T2R2 東京科学大学 リサーチリポジトリ
Science Tokyo Research Repository

論文 / 著書情報
Article / Book Information

題目(和文)	がん光熱治療用FePt/Au中空ナノシェルに関する研究
Title(English)	Study on Hollow FePt/Au Nanoshells for Photothermal Therapy of Cancer
著者(和文)	張茹芝
Author(English)	Ruzhi Zhang
出典(和文)	学位:博士(工学), 学位授与機関:東京工業大学, 報告番号:甲第10504号, 授与年月日:2017年3月26日, 学位の種別:課程博士, 審査員:北本 仁孝,和田 裕之,吉本 護,中村 一隆,柘植 丈治
Citation(English)	Degree:Doctor (Engineering), Conferring organization: Tokyo Institute of Technology, Report number:甲第10504号, Conferred date:2017/3/26, Degree Type:Course doctor, Examiner:,,,,
学位種別(和文)	博士論文
Type(English)	Doctoral Thesis

Powered by T2R2 (Science Tokyo Research Repository)

Tokyo Institute of Technology

Study on Hollow FePt/Au Nanoshells for Photothermal Therapy of Cancer

by

Ruzhi Zhang

Supervised by:

Professor: Yoshitaka Kitamoto

Associate Professor: Hiroyuki Wada

Submitted in February 2017

Table of Contents

Chapter 2 Synthesis of Silica-FePt/Au Core-Shell Nanospheres

Chapter 1 General Introduction

1.1 Photothermal Therapy

1.1.1 Critical Needs for Photothermal Therapy

As one of the leading causes of death, cancer accounted for over 8.2 million deaths and 32.6 million living with cancer (within 5 years of diagnosis) annually in 2012 worldwide [1]. The main reason for this is that the traditional methods of cancer treatment (such as surgery, chemotherapy, and radiation therapy) having many important disadvantages, have failed to fulfill the demands of modern cancer treatment. For example, surgery had been taken as the first-line therapy for a lot of tumors but becomes limited to the patients who do not qualify for surgical resection because of the bad medical conditions or the presence of deep-seated lesions. Chemotherapy can kill rapidly growing cancer cells but also can harm perfectly healthy cells, causing systemic side effects due to unspecific drug delivery to all tissues. In addition, the development of drug resistance by the cancer cells is another one of main causes of failure in Chemotherapy treatment. This outcome underscores the critical need for minimally invasive alternatives. The ideal minimally invasive procedure should decrease health care costs, shorten hospital stays, and offer effective treatment options to patients who are otherwise not eligible for surgery or other conventional treatments. More importantly, the ideal minimally invasive procedure should selectively eliminate only diseased tissues without causing side effect at least.

Nowadays, photothermal therapy (PTT), also called as photohyperthermia, as a promising alternative strategy, is attracting much attention due to its potential advantages of minimal side effects, low toxicity, great patient comfort, simplicity and potential to treat tumors in areas where open surgical resection may not be viable. The rationale for this type of cancer therapy is based on localized heating in the range of 41–47°C [2] due to light absorption by photo-absorbers in tumor tissues for the purpose of destroying cancer cells in a selective and targeted manner. Figure 1.1 shows the illustration of PTT, in which gold nanoshells is used as photo-absorbers.

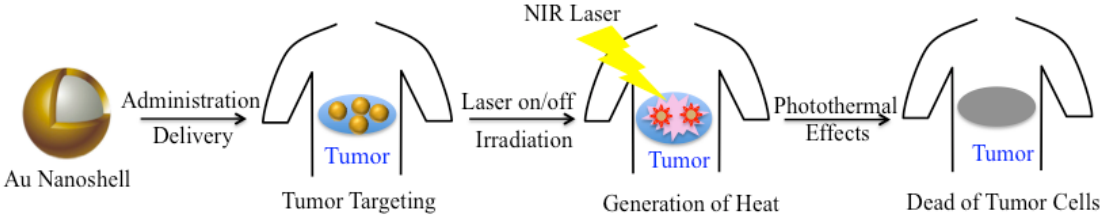

Figure 1.1 Illustration of gold nanoshells-mediated photothermal therapy of cancer

Reduced heat tolerance has been reported in tumor tissues due to their poor blood supply and heat dissipation [3]. As a result, direct and irreversible cell killing of tumors occurs by destroying cell membranes and denaturing proteins.

The heating achieved by converting laser energy into thermal energy is nonspecific so that treatment volume and exposure time are limited by potential damage to the surrounding normal tissues. Therefor, the use of the light-absorbed nanomaterials as photothermal agents (PA) in PTT to produce localized heating with little collateral damage can not only greatly reduce the non-specific damage associated with PTT, but also make it possible to obtain t therapeutic heating at relatively low-power laser or with short exposure time. The effectiveness of PTT relies heavily on the performance of these photothermal agents. Therefor current research of PTT is mainly focused on the development of photothermal agents that would be more powerful and more specifically target cancer cells.

Like PTT, other types of minimally invasive cancer therapy strive to create a procedure that maximizes the death of cancer cells while minimizing surrounding damage. These techniques range from thermal ablation by radiofrequency, microwave, ultrasound, laser treatments, and oscillating magnetic fields. The characteristic features of these different techniques of cancer treatment are showed in Table 1.1.

Radiofrequency ablation (RFA) that uses a high-frequency alternating current (in the range of 350–500 kHz) [4] through one or more electrodes placed around and in tumor tissue resulting in heat and coagulative necrosis to heat tissues to the point of desiccation, has the broadest application in cancer treatment. Therefore, not surprising, the biggest advantage of this method is experiences. RFA is generally conducted in the outpatient setting but requires the direct placement of one or more electrodes and grounding pad in close proximity to the tumor. This technique does not discern between healthy and tumor tissue. If healthy tissue is within the path of the RF waves, the tissue will be destroyed along with the cancerous tissue. Additionally, the desiccation and subsequent that result from high temperature in RFA increase in tissue impedance, as well as skin burns at the grounding pad reported in a few instances limits the repeat treatment.

Microwave ablation (MWA) using electromagnetic waves (typically 915 MHz and 2.54 GHz) to induce high temperatures of more than 100°C [5] represents a relatively new electrosurgical technique. Here also, one or more antennas are placed into the tumor. The shorter wavelengths of microwaves provide the capability to direct and

Table 1.1 Characteristic features of various types of cancer treatment techniques

Technology	Radiofrequency (RF) ablation	Microwave（MW） ablation	High-intensity focused Ultrasound (HIFU)	laser-induced thermotherapy (LITT)	Magnetic fluid hyperthermia(MFH)	NIR laser-mediated photothermal therapy (PTT)
Energy source	high-frequency alternating current	electromagnetic waves	focused ultrasound	laser of 800-1100nm	oscillating magnetic fields	NIR laser of 800-1100nm
Energy power	frenquecy of 350–500 kHz	900-2500MHz	2-20 MHz ,100^1000W	2~15W	0~5 kA/m of 0.05~1.2 MHz	0.5~5W
Applicator	one or more electrodes	one or multiple antennas	ultrasound probe	one or more Laser fibers	magnetic nanoparticles	photo-absorbers
Temperature	55~100°C	~100°C	60~70°C	50~100°C	42–46 °C	42–46 °C
Lesion size	a few millimeters(5~7mm) around the electrode	less 2 cm away from the antenna	less 2 mm from the probe	~7 mm	several centimeters	several centimeters
Possible methods	local/regional hyperthermia	local/regional hyperthermia	local hyperthermia	local hyperthermia	local hyperthermia	local hyperthermia
Exposure duration	3~5 min	1-5 min	1-10 s	~3 min	several tens of minutes	~6 min
Precision	Bulk heating	Bulk heating	Precise	Precise	Precise	Precise
Suitable tumor	deep and large tumor	shallow and small tumors	deep placed soft tissue	thin, continuous tumors	small tumors	deep tumors
Invasivity	Non specific damage	minimal invasive	Noninvasive	minimal invasive	minimal invasive	Noninvasive
Repeatable	difficult	possible	possible	difficult	possible	possible
Advantages	Well-controlled focal thermal injury, Proven effectiveness, Worldwide availability and ability to treat different tumor types.	High temperature available. Capable of forming large lesions in the presence of blood perfusion.	Good depth of penetration with the ability to pass harmlessly through tissues. Large scope for treatment of different tumor types. Potentially curative and repeatable.	Highly cost-effective, Can deliver controlled low energy through a variety of fiber configurations to achieve thin, continuous lesions in and around defined structures	No heat generation in healthy tissue, No pain expected by the patient.	Low energy power and minimal heat transfer, No heat generation in healthy tissue
Disadvantages	Surface heating, Need to conduct electric energy into the body, Limited Ablation zones	Higher susceptibility to heat-sink effects cumbersome than RFA and use larger cables , Complexity of microwave antenna design, Limited length of tissue,	Expensive,Unstable,Requires general anesthetic. Long time taken to ablate given object. Cannot be directed through air-filled viscera such as the lung.	High power , Small volume of tumor ablation, Successful ablation of only 2 cm. Tissue charring around the tip of the fiber. Pain expected by the patient.	Low efficiency of heating generation, Needs of large amount of magnetic particles(approximately 10% of the tumor volume)	Small volume of tumor ablation, Limited depth of laser penetration in human body, Ununiformity of heating, Residual of tumor cells

focus the energy into tissues, and the much broader field of power density (up to 2 cm surrounding the antenna) results in a much larger zone of active heating. Compared to several other thermal therapies, reduced penetration with microwave energy, as well as several practical problems, such like power loss, resultant heating of the coaxial cable and the complexity of microwave antenna design, limit its application greatly.

High intensity focused ultrasound (HIFU) is an early stage medical technology in which ultrasound probes placed in close proximity to a tumor can cause tissue damage. The most important advantage of HIFU should be that only sound waves is used in this type of treatment to kill the tumor, which avoids many side effects induced in other types of cancer treatment. However, there are still some drawbacks of this method limiting the clinical application of HIFU. For example, HIFU doesn't pass through either solid bone or air and it is only useful to a tumor with large dimensions. Most important, the potential injury from the ultrasound probe to normal tissue in the near field of the ultrasound probe is critical [6]. By now HIFU is not FDA approved and is not available in the United States. The poor experiences of HIFU also limit the development of HIFU.

Laser ablation, also named as laser-induced thermotherapy (LITT) can be applied by the placement of a laser fiver or by light-absorbers delivered to the tumor where photon energy conduction induced heating can reach temperatures of over 50°C. Laser therapy also results in a nonspecific area of necrosis. Light-absorbers, such as indocyanine green (ICG) can be utilized to minimize nonspecific damage. However ICG is not ideal because the small molecule is not retained in the desired area and is unevenly distributed in the tissue. Also, the power required to obtain a tumor response, 50~100W/cm2, causes severe damage to non-target tissues [7].

Magnetic hyperthermia also is an early stage medical technique for cancer. In this procedure, magnetic nanoparticles (MNPs) are injected into patient's body and the patient is placed in an alternating magnetic field. MNPs selectively target into cancer tumor and heat up when an external high-frequency field is added. As a result, the temperature of the tumor rise up and cancer cells are killed by thermal damages. And the thermal damages induced in this type of cancer treatment are specific due to no heat generation in surrounding healthy tissue without MNPs. For optimal magnetic hyperthermia, magnetic nanoparticles of a minimal dosage should be able to generate sufficient heat to increase the tumor tissue to at least 42°C.The generated heat amount depends on the strength and frequency of the AC magnetic fields, and the magnetic

properties of MNPs. In order to avoid nonspecific heating of healthy tissues, the application of high strength or high frequencies magnetic fields is restricted. Therefor, the desirable MNPs must have high heating efficiency. However, in practice, it is difficult to obtain such magnetic nanoparticles due to the poor magnetic anisotropy and magnetic moments for small particle size of MNPs.The difficulty of getting sufficient heating led to iron volumes equal to about 10% of tumor volume being required. However, the concentration of MNPs in injectable doses is low in practice.

Up to date, these methods are being developed greatly. Still, the nonspecific damage to the healthy tissue limits their application. In PTT, the photothermal agent in combination with NIR light induces cell death by thermal damage only in selective areas. Neither the photothermal agent nor the NIR laser is cytotoxic alone; only the combination induces cell death. Moreover, currently, compared with other physical energy sources, the use of laser is the most accurate way to deliver energy to the intended target. With the assistance of the photothermal nanoagents, the laser power required for the complete tumor regression was decreased greatly, which make PTT far safer.

1.1.2 Near-infrared Light Source

When light is incident on a tissue, it is transmitted, scattered, or absorbed depending on the wavelength. Light that is not scattered attenuates exponentially as it passes through tissue. The primary absorbers in tissue are water, hemoglobin, oxyhemoglobin and melanin. A “therapeutic window” exists in the NIR region between 650–900 nm, where there is minimal absorption by skin and tissue, which leads to minimal tissue invasion and deeper (up to 10cm) tissue penetration. In PTT, near-infrared (NIR) light is preferred to allow for noninvasive penetration of reasonably deep tissues. By designing the photothermal nanoagents to absorb the light within the NIR region, light-induced heating in tissue is confined to specific areas containing the photothermal agents.

The thermal response of PTT agents strongly depends on the parameters of laser source; therefore, the optimization of the parameters of laser source is needed in order to obtain sufficient therapeutic heat for cancer treatment. For example, both of continuous wave and pulsed lasers are workable in PTT.We can select them based on the requirement of a specific application. In the case of continuous wave laser, an enduring and moderate heating is built up during the irradiation so that continuous wave laser is more suitable for thermal hyperthermia. In the case of pulsed wave laser with

high energy density, it enables an intense localized heating in the vicinity of light-absorbing nanoparticles and is best suited for photothermal imaging.

1.1.3 Ideal Photothermal Agents

The heating achieved by converting laser energy into thermal energy is nonspecific so that treatment volume and exposure time are limited by potential damage to the surrounding normal tissues. Using light-absorbed nanomaterials as photothermal agents (PA) to produce localized cytotoxicity with little collateral damage can greatly enhance the selectivity and specificity for disease destruction. The effectiveness of PTT relies heavily on the performance of these photothermal agents. Therefor current research of PTT is mainly focused on the development of photothermal agents that would be more powerful and more specifically target cancer cells.

Ideal photothermal agents for PTT should fulfill the following requirements:

- Strong, tunable and stable absorption in NIR region. Strong SPR absorption, especially in the NIR region for optimal tissue penetration, always results in relatively high photothermal conversion efficiency and makes it possible to use low-power laser sources in PTT treatment. Tunable SPR absorption is needed to match the selected laser wavelength and minimize tissue absorption in the NIR absorption and stable SPR absorption is useful when operate the treatment for a long time or many times.

- Spherical or near-spherical shape, which is generally more desirable for delivery. There are studies indicating that the shape of particles can significantly affect the kinetics of cell internalization and the rate of endocytosis (Yoo et al.). Spherical shape is crucial for the efficient intracellular uptake due to the ease of cell penetration for spherical particles and uniform cellular interaction regardless of orientation. The non-spherical particles were reported to have a lower uptake than spherical particles with the same composition (Gilbert et al.).

- Small particle size of less than 400 nm. Particles in the 50~500 nm are readily internalized by cells and those in the 80~400 nm size range do not have a noticeable effect on differentiation of cells. And colloidal particles smaller than 400 nm are able to extravasate and accumulate in tumor regions due to the enhanced permeability and retention (EPR) effect (Yuan et al., 1995).

- Low toxicity. Ideal PA should be non-toxic to both healthy and cancer cells while its toxicity should only be activated in the presence of laser irradiation, which is required to achieve a selective cancer treatment with minimum side effects.
- Good solubility in biocompatible liquids (such as hydrophobicity, minimal aggregation). This would ensure long blood circulation time for high tumor uptake of nanomaterials via the enhanced permeability and retention (EPR) effect and, consequently, easy access to cancer tumors and high accumulation at the tumor site.
- Easy functionalization. Accumulation of PA at the tumor is essential in PTT treatment. A surface that is convenient for bioconjugation is desirable for actively targeting specific cancer cell. This would also allow for highly selective treatments since active tumor targeting would become possible.

Over the past decades, many different types of photothermal agents with NIR light absorbing capability have been widely reported. They can be classified into two families: organic agents and inorganic agents. The morphology, heating mechanisms, efficiency and spectral ranges greatly differ from each other.

Organic agents with small molecular weights, such as indocyanine green (ICG) or poly-pyrrole (PPy), have good biocompatibility and biodegradability, and therefore can be used for nanobiotechnology. ICG is approved for clinical use on patients by the US Food and Drug Administration (FDA), and has been widely used in phototherapy for many years. However, the low photothermal conversion efficiency, nonspecific binding to proteins, lack of tumor-targeting specificity, especially, photobleaching, of these organic materials limit their application in PTT.

Inorganic agents including metallic nanoparticles, carbon nanotubes (CNTs), graphene oxide (GO), upconversion nanoparticles (UNPs), quantum dots, rare earth ions-doped nanoparticles and semiconductor nanoparticles have been attracted much attention recently due to their high photothermal conversion efficiency, non-photobleaching and the ease of synthesis and modification. Among them, gold nanostructures, including gold nanospheres, gold nanoshells, gold nanorods, gold nanocages and even gold nanostars, have attracted much attention owing to their unique features, such as their optimal absorption efficiency, tunable size and morphology, good biocompatibility and easy surface modification. The rapid heating of gold nanostructures has also lead to reduction in treatment time of PTT. These properties make gold nanostructures particularly appropriate for PTT. Many studies have investigated Au

nanostructures-based PTT as shown in recent reviews. In fact, it is generally accepted that gold nanostructures are one of the most widely studied photothermal agents and plays an important role in the area of photothermal treatment for cancer therapy. The most commonly used gold nanostructures for cancer cell sensing and therapies are gold nanoshells (Au NSs) [8]. Au NSs are spherical particles composed of a dielectric silica core surrounded by a thin gold shell. Au NSs are unique in that they combine the following ideal features in a single particle:

(1) They have very large optical absorption cross-sections;

(2) They can designed and fabricated to preferentially absorb light at specific wavelengths from the visible to the near-infrared (NIR) regions of the spectrum;

(3) They can efficiently generate heat by absorbing radiation, and are thermally stable at therapeutic temperatures;

(4) They preferentially accumulate at tumor sites due to their nanoscale dimensions and spherical shape. Table 1.2 shows the optical cross-sections (σ_{ext}) of Au NSs compare favorably with those of conventional fluorophores and quantum dots [9,10].

Very recently, a new metal nanostructure, namely hollow gold nanospheres (HGNs), has been recently developed and successfully used for PTT. HGNs have many advantages such as spherical shape, small size (less than 100 nm in outer diameter), hollow spherical structure and strong and tunable absorption due to the two surfaces

Table 1.2 Comparison of Au NSs with conventional fluorophores and quantum dots in extinction cross-sections

Geometry	Dimensions (nm)	Wavelength (nm)	σ_{ext} (m^2)	Ref
Au nanoshells	120 of silica-core 10 of shell thickness	808	3.8×10^{-14}	[9]
CdSe-QDs	130	808	1.5×10^{-14}	[9]
Indocyanine green	Molecular	88	1.66×10^{-20}	[10]

(interior and outer) present. In particular, its hollow structure can be used to load anticancer drugs and then achieve the combination of photothermal therapy and chemotherapy, which has important applications in anticancer medicine. However, almost all nanostructures investigated for PTT and similar purposes to date can meet some of the requirements for ideal PA, but not all at the same time. For example, nanorods, nanocages, nanostars and nanocubes of gold can afford strong NIR absorption but have non-spherical shape. Their cell penetrations are known to be less effective compared to spherical nanoparticles. Likewise, core/shell structures with dielectric cores, for example, silica, have tunable NIR absorption and spherical shape but SPR absorption is not strong enough. Thus, they require more laser power than other gold nanostructures. The application of HGNs also suffers from many intrinsic drawbacks. The optical quality of HGNs is not high mainly due to the low uniformity of the hollow Au shell, which is generated using Cobalt nanoparticles with a poor uniformity as a template. Other problems with these systems include typically structural instability, poor photothermal stability and low tumor-homing ability (it is possible to accomplish selective targeting but not active targeting).

1.1.4 Challenges and Possible Solutions of Photothermal Therapy

PTT is a promising technology of cancer treatment due to its unique advantages but still an experimental treatment for cancer. However, there are still many challenges ahead for the clinical application of PTT.

Firstly, the resistance of cancer cells to thermal therapy, the nonuniform heat distribution and rapid heat dissipation by circulating blood make it difficult to realize the complete tumor eradication only by PTT. Thus it is necessary to combine PTT with other medical technologies that can effectively enhance the efficacy of the cancer treatment. By now the most used medical technology to combine with PTT is chemotherapy due to the enhanced cytotoxicity of some cancer drugs at temperature rise. And a concerted photothermal-chemo therapy with a single platform capable of simultaneous PTT and targeted drug delivery is preferred to minimize nonspecific systemic spread of nanodevices in human body. However the development of a highly efficient nanodevice for the photothermal-chemo therapy possesses a lot of challenges. Recently it is reported that the use of a novel photoactivated nanomaterial, hollow gold nanoshells remarkably enhanced the therapeutic efficiency while minimizing acute side effects. Hollow gold nanoshells (HGNs) consisting of a huge cavity surrounded by a thin shell of gold are extremely efficient NIR light absorbers. Recent researches

demonstrated that HGNs provide a possibility to treat tumors efficiently and completely. We will review the development of HGNs in details in the next chapter.

Also, the accumulation of photothermal agents at the tumor remains a matter of challenge. Efficient accumulation of PA in selected tumors is necessary to achieve optimal therapy. Bioconjugation of photothermal agents with targeting ligands, e.g. small molecules, peptide, aptamer, etc. for actively targeting specific cancer cell has been applied [11] to increase the accumulating concentration of PA in the tumors. However, the ability for actively targeted delivery of the nanostructures with targeting ligands to tumor cells is limited. The improvement of tumor-homing ability is needed. Extra-magnetic field (MF) mediated tumor targeting, as one mechanism that holds promise for in vivo applications is a good choice to assist in the aggregation of photothermal agents within cancer cells to increase PTT efficiency. In the MF mediated tumor targeting, an external magnetic field is used to induce therapeutic magnetic particles to target specific tissue sites. Many studies have experimentally demonstrated magnetic field-directed assembly of magnetic nanoparticles (e.g. Fe_3O_4 nanoparticles) for various vivo applications[12]. Moreover, Schleich et al. [13]compared in vivo four different strategies in terms of targeting capabilities and found that magnetic targeting showed a better nanoparticle accumulation in tumor compared to active targeting in ex vivo biodistribution. They also found that the most effective targeting strategy for therapeutic purposes was the combination of the magnetic targeting and active targeting due to improved particle accumulation at the tumor and longer survival time. Therefore, nanoparticles with double magnetic active targeting capability (e.g. magnetic gold nanoparticles) might become the next promising nanomedicine for cancer therapy.

One issue of importance with gold nanostructures-based PTT agents, as with all optical materials, is photothermal stability [14]. It is well known that the melting point of metal nanoparticles greatly depressed below the bulk melting temperature due to their small size [15]. And the metal shell layer with the high surface-to-volume ratio resulted from their core-shell geometry will seek to minimize its free energy and segregate into a solid particle at elevated temperatures. Therefore, any depressed melting temperature will be accompanied by a significant change of nanoshells in morphology, and consequently, in optical properties. Moreover, the rough surface of the colloid-nucleated metallic shell results in an increased surface area. Also, a high number of surface defects and fissures could decrease both of the structure stability and thermal stability of metallic shell. It had been reported that the shape and structure of thermally unstable gold nanostructures (such as gold nanoshells, gold nanorods, gold nanocages, hollow

gold nanoparticles and so on) were significantly changed after NIR laser irradiation, resulting in the reduced SPR absorbance and considerable blueshift in peak wavelength. Although some methods had been developed to improve the thermal stability of gold nanoshell or gold nanorod, a lot of additional synthetic steps were required in these procedures and the improvement in the thermal stability is limited. For example a protective layer of silica only could increase the melting temperature of gold nanoshell from 275°C to 300°C [16].

Finally, most nanoparticles are known to lose their uniformity and reproducibility when production is scaled up. Therefore, great efforts into the improvement of synthesis methods of nanoparticles are needed to ensure high quality control of nanoparticles.

1.2 Hollow Gold Nanoshells

1.2.1 Introduction

As an important member of nanomaterials, gold nanomaterials have drawn wide attention in the biomedical field due to its numerous excellent properties, such as good biocompatibility, excellent photothermal conversion, and easy modification with a variety of biological molecules. And hollow gold nanospheres (HGNs) represent one of the most promising candidates for cancer therapy due to their unique chemical/physical properties as below:

1) Compared with gold nanospheres whose absorption peaks are located in visible region of 520 nm, the absorption peaks of HGNs could be adjusted to the near-infrared region (700~900 nm);

2) HGNs have less toxicity than GNRs, because bio-toxic CTAB used in synthetic process of GNRs is not necessary in synthetic process of HGNs;

3) HGNs have a spherical shape that is the most suitable shape for targeted delivery in human body;

4) Hollow structure of HGNs generates minimum mass in the same size of gold nanostructures of different morphologies. Its cavity structure can be used to load drugs and then achieve the combination of photothermal therapy and chemotherapy, which has very important applications in anticancer medicine.

Therefore, it can be predicted that multifunctional nanoparticles based on HGNs will play an increasingly important role in the integrated treatment of tumors.

1.2.2 General Synthetic Techniques

A variety of approaches have been developed for the synthesis of HGNs. Here we will focus those approaches by which HGNs with NIR absorption can be prepared successfully. Sacrificial galvanic replacement of cobalt nanoparticles is a popular method to synthetize HGNs currently. The fundamental is introduced as follows. Firstly, Cobalt nanoparticles (CoNPs) are synthesized, then the CoNPs colloidal solution is transferred to stirred HAuCl4 aqueous solution. The $AuCl_4^-$ ions in the $HAuCl_4$ solution were quickly reduced to Au atoms. The Au atoms nucleated, grew continuously on the surface of CoNPs. Finally, HGNs are obtained after CoNPs are completely consumed. In this method, the particle size of HGNs can be controlled by the diameter of the Co NPs and the shell thickness of HGNs can be controlled by the amount ratio of $HAuCl_4$ and the reducing agents. The reaction equation is shown as follows:

$$3Co+2AuCl_4^-=2Au+3Co^{2+}+8Cl^-$$

Liang et al. [17,18] first reported the use of sacrificial galvanic replacement of cobalt nanoparticles to synthesize HGNs. The study showed the SPR peak position of HGNs would be adjusted from 550 nm to 820 nm.

Recently silver nanoparticles (AgNPs) were also used as sacrificial templates in the synthesis of HGNSs via a sacrificial galvanic replacement reaction, in which AgNPs were reacted by the addition of $HAuCl_4$ aqueous solution. The reaction equation is shown as follows:

$$3Ag_{(s)} + AuCl_4^-{}_{(aq)}=Au_{(s)}+3Ag_{(aq)}^+ +4Cl^-_{(aq)}$$

The reduction of Au^{3+} ion results in the oxidation and dissolution of Ag ions from the template. The galvanic replacement reactions using Ag nanoparticles as sacrificial template has been demonstrated to be a simple and elegant method to synthesize HGNSs, however, almost all of the HGNs resulted by this method are seamless without and pores due to the high reaction temperature of ~100 °C. Under such a high temperature, the gold shells reconstructed them into a smooth and complete surface, which means that there are not any pores on the surface of HGNs and drugs only can be loaded on the outside of HGNs.

Zhang et al. [19] and Prevo et al. [20] successfully prepared HGNs using Ag NPs as template. The sizes of HGNs synthesized by this method range from 20 to 50 nm in

diameter and the SPR absorbance of HGNs could be precisely manipulated within the wavelength range of 600–800nm.

Galvanic replacement reaction processes can produce HGNs with tunable size and shell thickness, and are reproducible, as demonstrated by several independent laboratories already; however, they still present some important limitations.

Firstly, the disadvantages of galvanic replacement reaction processes are complicated synthesis process, unstable conditions and low reproducibility of produced particles. Moreover, cobalt nanoparticles is very sensitive to oxidation under ambient conditions. Although many different strategies have been developed to improve the long-term oxidation stability of cobalt template nanoparticles, for example the use of PVP as a stabilizer of cobalt particles by Preciado-Flores et al.[21], these post modification methods are often laborious and not ideal. The use of stabilizers not only resulted in the formation of multicore particle aggregates, but also results in HGNs with decreased binding affinity for PEGylated linkers used to conjugate antibodies, which in turn reduces the targeting ability of HGNs. Additionally, the use of cobalt NPs or Ag NPs make these methods not eco-friendly.

Secondly, the low homogeneity of HGNs is another problem. HGNs prepared by these two methods exhibit larger variations in core diameter and shell thickness, which resulted from the limited uniformity of metal templates in particle size. The poor uniformity of the shell diameter causes the broader spectral width.

Thirdly, the design of HGNs in particle size and pore size is limited. It is difficult to enlarge the particle size of HGNs more than 100nm due to the big challenge in the production of more and large cobalt or silver nanoparticles. So these conventional galvanic replacement strategies would be not helpful for some special application in which HGNs with the size of more than 100nm is needed. On the other hand, controlling pore size, another important parameter of HGNs, especially in the application of drug delivery, is difficult since the pore size of HGNs always changes when shell thickness changed in the synthesis process of these methods. Changing particle size at a constant shell thickness is difficult.

Another method of preparation HGNs is using nonmetallic structure as core and gold as shell. Liu et al. [22] firstly succeed in synthesizing hollow shell using the hollow C-60 nanometer shell as template. Zhong et al. [23] used the cross-linked product of glucose oxidase (GOD) and glutaraldehyde as template to prepare gold nanospheres

with hollow structure. However the SPR absorption band of these shells only showed in visible region. Graf and van Blaaderen [24] synthesized a gold shell on the surface of silica and then obtained hollow gold nanospheres by dissolving SiO_2 core with hydrofluoric acid, The SPR absorption in NIR was obtained but the structure stability of these hollow shells was poor. Some shells broke into parts after dissolving the silica cores.

Therefore, nowadays, the development of facile and environmentally friendly procedures for the synthesis of hollow gold nanoshells with a tailored morphology and NIR absorption is still an important challenge.

1.2.3 Biomedical Applications of Hollow Gold Nanoshells

PTT is considered a good choice to treat tumor cells; however, it is difficult to eradicate tumor cells by PTT alone because of the nonuniform heat distribution. There have been quite a few studies that combine PTT with chemotherapy and the results are proved to be better than PTT or chemotherapy alone. Chemotherapy is an important method of treating cancer. Many anticancer drugs are difficult to give full play to efficacy in treatment because of poor stability, low solubility, being nontargeted, and easy removal by metabolism. However, loading cancer drugs on a suitable support cannot only extend residence time of drugs in the body, thereby improving the utilization of drugs, but also control the release of drugs. In addition, if the carrier is conjugated with targeted molecules, it can also greatly reduce the cytotoxicity of drugs to normal cells caused by no targeting. Ideal drug carriers should have characteristics of chemically stable, long half-life, nontoxic or low toxic, biodegradable, large drug loading capacity and others. HGNs just successfully demonstrated to meet most of the requirements for ideal drug carriers simultaneously because of their cavity structure, large specific surface area, good biological safety and biocompatibility, and facile surface functionalization. The inner cavity allows high drug loading. Moreover, HGNs can delivery the payload efficiently and safely to the tumor by loading the payload into the inner cavity surrounded by a protective polymer layer When NIR light is irradiated to tumor cells, HGNs absorb light and convert light into heat. At the same time, the temperature-responsive polymer coated on the HGNs surface begin shrinking and releasing drug. The combined photothermal-chemo therapy is a very attractive therapy model to kill tumor cells completely [25].

You et al. [26] reported bifunctional use of ~40 nm HGNs for photothermal ablation of cancer cells and drug release upon NIR light irradiation, revealing their excellent

drug delivery properties. The results showed that HGNS not only had extremely higher payload capacity at least 3.5 times that of solid gold nanoparticles with the same size, surface charge, and weight, but also generated the much higher photothermal heat upon NIR laser irradiation compared to their solid counterparts. They also found that the doxorubicin-loaded HGNS displayed decreased systemic toxicity compared to free DOX or liposomal DOX and exhibited enhanced antitumor effect after the irradiation of laser [28].

In addition to transport drugs, HGNs can play the role of delivery carrier for gene therapy that is a new promising medical technique by using genes to treat and prevent disease. siRNA is one of the strong candidates for the next generation of gene therapy. However, the most critical factor limiting the application of siRNA-mediated gene therapy is delivery siRNA to its target site because their negative charges, large size and low chemical stability are not favorable for in vivo delivery. Using HGNs to deliver siRNA with the acid of NIR light can obtain both of the enhanced stability and temporal and spatial release of siRNA molecules in vivo. Lu et al. coupled [29] small interfering RNA (siRNA) and biological targeted molecules folic acid (FA) to HGNs. HGNs delivered siRNA to tumor cells. Under the NIR laser irradiation, siRNA separated from HGNs and bound the transcription factor NF-kB, which made it not able to function properly and thereby inhibited tumor cell growth. It showed the promising applications of HGNs for gene therapy or photothermal combined gene therapy.

1.2.4 Challenges and Possible Solutions of Hollow Gold Nanoshells for Biomedical Applications

The advantage of hollow plasmonic nanostructures mainly comes from the presence of two surfaces (internal and external) and hybridization among them, along with the presence of cavities and pores at the shells. Thanks to the progress in the current synthetic routes, we can now master the issues like shell thickness and void size, yet perfect control on the size and distribution of the surface pores, which are as important as the void size when HGNs were utilized as a delivery carrier of drug or gene, is a crucial challenge to overcome in the future. Actually, in almost all cases of galvanic replacement reaction strategies, the reaction would be permitted to proceed until a complete shell formed in order to obtain uniform and structurally stable HGNs, so that their pores size are too small to be measured by TEM or SEM. However the payload capacity of HGNs for drugs or contrast agents would be greatly limited by their small pores.

Another challenge should be to improve the photothermal stability of HGNs. For the core-shell structured metal nanoparticles with a high surface-to-volume ratio, there is such a tendency to change their geometry to a solid particle for minimizing their free energy and obtaining a stable state. Therefore, any factors causing a change of the core-shell structured metal nanoparticles in the melting point would also induce a similar change in their morphology and optical properties. More recent studies have reported the aggregation, fragmentation, and melting of gold nanostructures by laser irradiation, resulting in the reduced SPR absorbance and considerable blueshift in peak wavelength [30]. In particular, HAuNS with increased surface area and hollow cavy possess high potential energy, which causes HAuNS thermally unstable and inducts energy relaxation by changing the shape or structure to reach a stable state. Lu et al., [31] reported that an obvious morphology change of HAuNS induced by the heat generated during the laser irradiation had been observed. The decrease in light absorption of HAuNS after NIR laser irradiation was also observed. At the same time an SPR band at ~520nm resembling an absorption peak of spherical solid gold nanoparticles appeared. The reshape of HAuNS into solid droplets was observed. The lase-induced heat even transformed HAuNS into solid spherical particles [32].

In addition, as previously discussed, the success in obtaining HGNs with the tunable absorption over a wide range comes as an output of having full control over the synthesis of metal template nanoparticles, the protection of metal template nanoparticles from oxidations, galvanic replacement reaction conditions, and surface functionalities. However these routines are rather complex, sensitive and not eco-friendly. Each step has to be controlled carefully for high quality of HGNs. The next step forward would be to optimize these routines in order to meet with the requirements for industrial applications.

Another consideration in designing HGNs with improved performance is the integration of active targeting capability. Combining HGNs with magnetic particles is thought to be an optimal option since the ability of active targeting via bioconjugation of targeting agents on the surface of HGNs is limited and magnetic targeting showed a better nanoparticle accumulation in tumor compared to active targeting in many cases.

1.3 Magnetic Gold nanoshells

1.3.1 Introduction

Multifunctional nanomaterials that contain two or more different functionalities are attractive candidates for technological applications in the areas of biomedicine. Therefor it is natural and right for researchers to design and fabricate of multifunctional gold nanoparticles by the strategy of integrating the gold nanoparticles with other functional nanocomponents inspired by the potential benefits of multimodal functionality. Such multifunctional gold nanoparticles can possess several favorable capabilities simultaneously. Recently, magnetic gold nanocomposites as one of highly promising multifunctional gold nanoparticles developed for the biomedical application have been attracted much attention because they can exhibit excellent magnetic properties and optical properties simultaneously, which could be very convenient for the application of cancer treatment, especially for multimodal imaging, targeted delivery and photo thermal therapy.

1.3.2 Magnetic Gold Nanoshells with Iron Oxide Nanoparticles

Over the past few years, a lot of multifunctional materials having both optical properties of gold and magnetic properties of superparamagnetic nanoparticles have already been reported. Multifunctionality is generally achieved by synthesizing gold shell of different core structures or outside epilayer. Paramagnetic iron oxide NPs (SPIO, Fe_3O_4) have been most widely chose as magnetic component due to their low cost and inherent biocompatibility. SPIONs are either stuck to the surface of a solid particle, or encapsulated in a core by a silica or polymer. Herein, as opposed to other types of theranostic agents, the unique advantage of magnetic cores is to provide opportunities to the applications of MR imaging, magnetically hyperthermia and magnetically enhanced targeting delivery. Table 1.3 shows the characteristic of various magnetic gold nanoshells reported in recent years. All of them possess the capability of being responsible to NIR light and magnetic field at the same time. Among them, the most commonly reported one is the core-shell structured Fe_3O_4/silica/Au nanoparticles reported by Maceira et al. [33] and Ji et al. [34]. Here silica coating is used as the dielectric interface, with SPIO NPs embedded inside a gold shell. The plasmonic properties of the core/shell structure can be red-shifted to NIR region by the control on shell thickness.

Oppositely, Bardhan et al. [35] attached SPIO NPs on the outside surface of silica-core gold nanoshells, and then prepared a thin silica epilayer doped with the fluorophore, ICG. When coated with SPIO NPs, the plasmon resonance of gold shell red shifts from 770nm to 815nm due to the higher refractive index of Fe_3O_4 (n= 3)

Table 1.3 Characteristic of various magnetic gold nanoshells having NIR absorption.

compositions	Particle size/nm	Size of magnetic NPs/nm	Thickness of Au shell/ nm	NIR absorption	Magnetic induction	Hollow porous structure	Drug loading
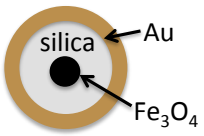 Fe_3O_4/silica/Au	~200 nm	~30 nm	~30 nm	○	×	×	△
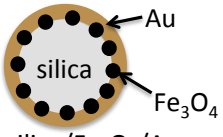 silica/Fe_3O_4/Au	~300 nm	~20 nm	~30 nm	○	△	×	△
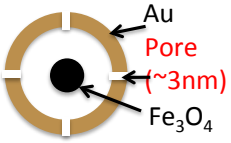 Fe_3O_4/hollow/Au	~100 nm	~30 nm	~20 nm	○	×	△	△

relative to H_2O (n =1.33). After coated with silica epilayer, the plasmon resonance of the final product shifts to 822 nm. In this structure, this silica epilayer is responsible to not only stabilize the magnetic particle by providing a chemically inert and biocompatible surface, but also protect the fluorophore of ICG from photobleaching. On the other hand, Kim et al. [36] prepared a layer of SPIO NPs sandwiched between silica and Au. Other materials, such as organic polymers, have also been used as dielectric interface between magnetic iron oxide core and Au shell.

All of the above-discussed magnetic gold nanoshell successfully present both magnetic property and NIR-optical property and show a good potential for biomedical application, however, most of these nanosystems have solid and compact structures, and drug loading is limited. Moreover, their capability of being responsible to the magnetic field is limited since the number or the size of magnetic nanoparticles encapsulated in these structures are limited due to a lot of technological difficulties during the synthesis process. Very recently, a few studies have been reported for the hollow magnetic gold nanostructures as well as their applications for multimodal imaging and PTT. For example, Yong et al. [37] successfully synthesized a plasmonic magnetic nanostructure consisting of hollow-type gold nanoshells with SPIO NPs inside their interiors for bimodal imaging and photonic-based therapy of cancer cells. The synthetic scheme is to

synthesize SPIO NPs (9-11nm), then deposit a gold layer of 2-3nm on these magnetic NPs, sequentially coat an outer Ag layer as a template for the formation of hollow gold nanoshells, finally hollow magnetic gold nanoshells with the SPR peak of 770nm. The potential of these hollow magnetic gold nanoparticles for biomedical imaging, targeted photothermal therapy had been investigated and demonstrated. However, similar with other HGNs prepared by mean of replacement reaction of Ag NPs, the surface of gold shell was seamless without any pores.

Yang et al. [38] developed another hollow plasmonic magnetic nanostructure using HGNs and SPIO NPs. Opposite to Yong's group, they successfully attached water-soluble SPIO NPs on the surface of HGNs by mean of modifying SPIO NPs with dimercaptosuccinic acid (DMSA) via a ligand exchange process to introduce thiol groups. Fe_3O_4 NPs-coated HGNs were lastly synthesized based on the chemistry of Au–S bond formation between thiol groups on Fe_3O_4 NPs and HGNs and took advantage of the inherent magnetic and strong NIR absorbance, which allow them a great promise for biomedical applications, particularly in cancer imaging and therapy.

Based on the above reported works, it is well known that combining SPIONs with HGNs to form a hollow multifunctional nanocomposite is workable, however, by such two approaches discussed above, it is difficult, if not impossible, to load drug or genes into interior space. Reported hollow magnetic particles usually have a seamless surface, which greatly limits their delivery functions for cancer treatment.

1.3.3 Magnetic Gold Nanoshells with Other Magnetic Nanoparticles

Despite the advantages and the widespread use of iron oxide NPs, they have been shown to have some weaknesses with regards to their relatively low magnetization saturation. Therefore, some other magnetic nanoparticles with higher magnetization saturation incorporated with gold shells, also had been developed for cancer treatment.

For example, Iron-platinum nanoparticles (FePt NPs) composed of an approximately equal atomic ratio of Fe and Pt represent an alternative because they possess a three-times-higher bulk saturation magnetization (about 1140 emu/cm^3) than that of iron oxides [39]. In addition to their promising properties for magnetic manipulation, a higher T2-shortening effect than iron oxide NPs allows FePt NPs to be superior contrast agents for MRI [40]. Recently, the finding that the cytotoxicity of unmodified FePt NPs was not significant during 24 h in brain endothelial cells further boosts FePt NPs potential in biomedical application. Almost all of these reported FePt/Au nanostructures

Table 1.4 Characteristic of various FePt/Au core-shell nanostructures reported by now

	Structure	FePt, diameter	Au, thickness	Silica, thickness	Plasmonic absorption	Saturation magnetization	Ref
FePt/Au	Mono-layered Core-shell	Core, ~8 nm	Outer shell, about 1 nm	No	530~540 nm	15 emu/g	[41]
FePt/Au/ silica	Double-layered Core-shell	Core, ~14 nm	Middle shell, about 7 nm	Outer shell, ~25nm	530~540 nm	Not available	[42]
FePt/silic a/Au	Double-layered Core-shell	Core, ~5nm	Outer shell, about 10nm	Middle shell, ~32nm	600~850n m	0.6 emu/g	[43]

shown in Table 1.4 have a core-shell structure in which gold also works as a functional coating due to gold's excellent biocompatibility and chemical stability. By incorporating with silica layer or not and the location of silica layer, these FePt/Au core-shell nanostructures can be divided to three following types:

(a) FePt/Au core-shell NPs in which a thin gold layer is directly prepared on the surface of FePt NPs;

The approach to synthesize FePt/Au core/shell nanoparticles is to use a seed-mediated method consisting of synthesis of FePt nanoparticles and then Au coating over the FePt nanoparticles. Monodisperse FePt nanoparticles (8 nm) were prepared via a typical polyol method [41], and then used as the seeds. Au shells were grown on the surfaces of the magnetic cores by reductive decomposition of Au $(O_2CCH_3)_3$ in the

presence of surfactants. Finally hexane dispersed FePt/Au core-shell NPs capped with oleic acid and oleyl amine ligands were made water-soluble by ligand exchange. These hybrid NPs are superparamagnetic at room temperature and the surface plasmon band shows a red shift compared to the case of the pure Au nanoparticles but still lies in visible region.

(b) Silica-protected FePt/Au core-shell NPs, in which an external shell of silica can be readily biofunctionalized and provides high colloidal stability [42];

Silica-protected FePt/Au core-shell NPs were fabricated by a seeded growth method using FePt colloid as seed. Firstly star-shaped FePt NPs of ~14 nm in diameter dispersed in organic solvents was prepared as the core. Then the aqueous FePt solution was obtained by phase transfer using cetyltrimethylammonium bromide (CTAB) as a phase transfer agent. Finally the growth of gold shell was achieved after the as-prepared seed solution including $HAuCl_4$ and ascorbic acid was added to the seed solution of FePt/CTAB. The optical band of the obtained silica-protected FePt/Au core-shell NPs appeared around 530–540 nm in the measured UV-visible spectra.

(c) FePt-core silica/Au nanoshells that a thick silica layer is used as an intermediate layer for the optimum particle size and optical property [43].

The synthesis route involved three sequential steps, starting with the synthesis of the superparamagnetic FePt-core NPs using a modified polyol method reported by Sun's group [44], followed by the formation of a thick silica shell, which was subsequently decorated with a surface layer of Au. The gold shells were prepared by the two-step seed-mediated growth of gold on the silica surface, using the ~3 nm Au colloid as seed solution. To make the attachment of Au colloids successful, the silica surface was functionalized with APTES (3-aminopropyltriethoxysilane). These superparamagnetic hybrid NPs not only could be magnetically manipulated and retained at a targeted location under realistic dynamic conditions, but also have a quite broad absorption in the region of 600~900 nm, which make them workable for photothermal therapy and magnetically enhanced delivery with an external magnetic field. Until now, most of magnetically and optically active hybrid nanostructures for cancer treatment were prepared on the basis of SPIO NPs and gold shells, and the studies on FePt/Au core–shell NPs as MRI agent are more or less spread out; however, the promising properties of FePt led people to design novel hybrid nanosystems based on FePt/silica/Au NPs with properties designed for use in PTT.

On the other hand, it is reported that the doping of SPIONs with cobalt ions further enhances their magnetic property, thus forming $CoFe_2O_4$ NPs. These spinel ferrite NPs possess ca. 20–30 times higher magneto-crystalline anisotropy as compared to SPIONs; this increases the performance of materials for biomedical applications. Inspired by this, several magnetic gold nanoshell consisting these spinel ferrite NPs had been developed. For example, Ravichandran et al. developed a $CoFe_2O_4$@Au core-shell nanoparticle by iterative-seeding based method for magnetic hyperthermia combined with chemotherapy. This nanocomposite consists of a cobalt ferrite kernel as a core and

multiple layers of gold as a functionalizable active stratum. The targeted delivery of Doxorubicin using $CoFe_2O_4$@Au as a nanopayload is demonstrated in this report. And the cellular MR imaging showed that $CoFe_2O_4$@Au is an efficient T2 contrast agent.

Lee et al. [45] synthesized a new kind of magnetic gold nanoshells consisting of $MnFe_2O_4$ core, silica middle layer and the outside layer for cancer therapy and MR imaging. The prepared $MnFe_2O_4$/silica/Au nanocomposites were superparamagnetic and had a higher magnetization saturation (2 emu/g) than that of iron oxide NPs-based magnetic gold nanoshell (0.3 or 1.2 emu/g) [46]. However, similar with iron oxide NPs-base gold nanoshells, the performance of these magnetic gold nanoshells in magnetic property was kindly improved due to the higher magnetization saturation of magnetic materials than that of iron oxide NPs but still limited by the small size of single magnetic NPs and few numbers. More importantly, by now no studies of these magnetic plasmonic materials having porous hollow shell have been reported.

1.3.4 Photothermal Effect of Magnetic Nanoparticles

Some magnetic nanoparticles (MNPs) with a dark color, such as iron oxide (Fe_3O_4) nanoparticles, also can be applied as photothermal agents for cancer therapy because they exhibits a broad absorption of light from the visible to NIR region. More recent studies had demonstrated their potential in the application of cancer treatment. For example, in 2011,Yu T. et al. [47] used alumina-coated iron oxide magnetic nanoparticles as photothermal agents to selectively kill bacteria. In this study, the magnetic particles were induced to aggregate at a specific location by a magnetic field and then heated up when irradiated by NIR laser resulting in the killing of bacteria. In 2012, Liao, M. et al. [48,49] examined the photothermal effect of Fe_3O_4 NPs coated with APTES-functionalized mesoporous silica (mSiO2) in in vitro and in vivo and $mSiO_2$-coated Fe_3O_4 nanocomposite displayed dual modalities for photothermal therapy of cancer and MR imaging. In 2013, Chu, M. et al.[50] investigated the photothermal effect of Fe_3O_4 NPs with different shapes. No obvious differences in photothermal effects were found among the spherical, hexagonal, and wire-like Fe_3O_4 nanoparticles.

However, the concentration of these reported Fe_3O_4 NPs applied for the photothermal therapy of cancer by NIR laser irradiation are usually very high because of the lower photothermal conversion efficiency in comparison to Au nanorods and silica-core gold nanoshells under the same laser source [49~52]. Since extra-high-dose magnetite might generate potential toxicity to the body, Fe_3O_4 NPs must be improved if used as the PTT agent. There are mainly two routes: to modify efficiently NIR light-absorbing materials

onto the surface of magnetic NPs or to increase the number of the magnetic NPs. Recent reports showed that the clustering of magnetic NPs can induce a red-shift in the light absorption spectra [51]. In 2014,Shen, S. et al [52] reported that the clustered Fe3O4 NPs of 225nm induced the heating more efficient than the individual Fe_3O_4 NPs of 10~15nm.

Unfortunately, the sub-micro particle size of the clustered Fe_3O_4 NPs (200nm~) greatly limits their biomedical application. The difficulty of modifying Fe_3O_4 NPs to have targeting capacity should be another challenge since maintaining the good condition of antibodies on MNPs is difficult so that antibody-functionalized MNPs are only good for a short period of time.

Besides Fe_3O_4 NPs, FePt NPs, another important magnetic nanomaterial also have attracted attention due to their photothermal effect activated by NIR laser. FePt NPs, opposing to the unique feature of plasmon resonance as that of Au nanostructures, have a broadband absorption at NIR region. In 2012, C.L.Chen et al. [53] demonstrated the possibility of using magnetic FePt NPs excited by NIR femtosecond laser for aforementioned tumor-targeted therapy. Cubic-like shaped FePt NPs with a face-centered cubic structure and 12 ± 1.0 nm in diameter were prepared and 3-mercaptopropionicacid (MPA) was chosen to produce COOH-terminated water-dispersible FePt NPs. The surfaces of MPA-FePt NPs were then modified with folic acid to specifically target folate receptors. Finally these modified FePt NPs were then introduced into cellular environment. The results showed that the temperature of the FePt NPs can be heated up to a couple of hundreds degree C in picoseconds under laser irradiation. They further compared the efficacy of FePt NPs photothermal therapy in cancer cells with typical plasmonic Au NRs.The FePt threshold laser energy to destroy cancer cells (~10 mJ/cm^2) was found to be comparable to that of gold nanorods (~18 mJ/cm^2)[54].The better photothermal transduction efficiency and magnetic property than those of Fe_3O_4 NPs make FePt NPs, or FePt NPs-based materials, more competitive candidates in future cancer therapies. However, by now, about FePt NPs-based PTT, there are only few studies and the further development is needed.

On the whole, the finding in the photothermal effect boosts magnetic NPs versatility in multifunctional cancer therapy. Magnetic NPs with unique magnetic property and good photothermal property, have gained more recognition as a superior material in cancer diagnosis and therapy.

1.3.5 Magnetic FePt/Au Nanostructures

It is mainly superparamagnetic nanoparticles that have been utilized to combine with gold nanostructures for cancer treatment until now. However their capability of being responsible to a magnetic filed is limited due to their poor magnetic properties. At the same time, the excellent magnetic properties of FePt nanoparticles inspired people to use FePt NPs to prepare the magnetic gold nanostructures instead of iron oxide nanoparticles. More importantly, recent studies demonstrated the excellent photothermal effect of FePt NPs. It is expected that not only the magnetic targeting capability but also the photothermal therapy capability could be improved by the use of FePt NPs instead of iron oxide NPs. Additionally; the excellent uniformity of morphology and particle size is another advantage of FePt NPs compared with other magnetic materials. As well known, the magnetic property uniformity of magnetic particles greatly depends on the uniformity of morphology and particle size. It is believed that the choice of FePt NPs could also bring an improvement in both the structure and the properties.

Until now, the studies on magnetic hybrid FePt/Au nanoparticles with a spherical shape as MRI agent are more or less spread out, whereas the literature for the application of PTT is very sparse. Most of the reported FePt/Au nanostructures for magnetically functioned biomedical applications, have a core-shell structure in which gold is always utilized as a functional outside coating due to gold's excellent biocompatibility and chemical stability. There are also several FePt/Au tadpole-, dumbbell-, bead- and necklace-like heterostructures prepared by growing Au NPs on FePt nanorods, but with the aim to explore their catalytic activity [55].

Generally, FePt/Au core-shell nanostructures can be divided to three following types by incorporating with silica layer or not and the location of silica layer:(a) FePt/Au core-shell NPs in which a thin gold layer is directly prepared on the surface of FePt NPs; (b) Silica-protected FePt/Au core-shell NPs, in which an external shell of silica can be readily biofunctionalized and provides high colloidal stability [56]; (c) FePt-core silica/Au nanoshells in which a thick silica layer is used as an intermediate layer for the optimum particle size and optical property. N. Kostevsek et al. [57] designed such a multifunctional structure (FePt/silica/Au) for combining photothermal stimulation and manipulation with an external magnetic field. The synthesis route of FePt-core silica/Au nanoshells involved three sequential steps, starting with the synthesis of the superparamagnetic FePt-core NPs using a modified polyol method reported by Sun's group, followed by the formation of a thick silica shell, which was subsequently

decorated with a surface layer of Au. The gold shells were prepared by the two-step seed-mediated growth of gold on the silica surface, using the ~3 nm Au colloid as seed solution. To make the attachment of Au colloids successful, the silica surface was functionalized with APTES (3-aminopropyltriethoxysilane). These superparamagnetic hybrid NPs not only could be magnetically manipulated and retained at a targeted location under realistic dynamic conditions, but also have a quite broad absorption in the region of 600~900 nm. The experiment results demonstrated the photothermal effect of hybrid FePt/silica/Au NP. However, FePt/silica/Au core-shell NPs still have many drawbacks in both structure and property, similar with those of SPIO/silica/Au core-shell NPs because the improvements of magnetic gold NPs in both structure and properties resulting from the replacement of iron oxide NPs-based core by FePt NPs-based core are limited due to the limit number of FePt particles encapsulated in the core.

1.3.6 Challenges and Possible Solutions of Magnetic FePt/Au Nanostructures for Biomedical Applications

As discussed above, to develop a therapy that can selectively and completely kill tumor cells is one of the most important goals for the research of cancer treatment. Therefore, the development of a platform that can effectively delivery drug and absorb light is in great demand. Undoubtedly, it should be an ideal theranostic agent for photochemotherapy if there is a magnetic gold nanocomposite with

(1) A hollow porous structure with tunable particle size and pore size;

(2) Strong, stable and tunable plasmonic absorption in NIR region;

(3) High magnetocrystalline anisotropy enough to make it possible to be controlled by an external magnetic field;

To date, there are several reports on the synthesis of hollow the iron oxide/Au nanoparticles in the form of either core/shell or hybrid layers for biomedical application, in particular for cancer treatment. However till now, to the best of our knowledge, it hasn't been reported so far as to the successful synthesis of such a multifunctional nanocomposite. The main limitations of the current hollow magnetic gold nanoshell are listed below:

(1) Unstable plasmonic absorption, which is the important drawback of HGN and still left. It is difficult to improve the photothermal and structural stability of hollow gold

nanoshells via the use of magnetic NPs since few numbers of magnetic NPs are just stuck to the surface or encapsulated in the core.

(2) Relatively poor magnetic performance due to the superparamagnetic behavior of magnetic nanoparticles with small size and limit numbers.

(3) Small or no pores on the surface. Actually their surfaces were always prepared to be seamless or closely seamless in order to obtain the NIR absorption and maintain the structure stability.

(4) Limit size tunability and morphological uniformity, which results from the difficulty in controlling the size and morphological uniformity of cobalt/silver template NPs used in the traditional synthesis method of HGNs by the current synthesis technologies.

In the present thesis, a novel approach to counter the above issues and then obtain ideal magnetic gold nanoshells is proposed. In case of magnetic gold nanoshells for photothermal or chemo-photothermal therapy, the choice of magnetic materials is very important. In this thesis, instead of iron oxide NPs, FePt NPs is chose as magnetic material to incorporate with gold nanoshells due to their higher saturation magnetization and stronger photothermal effect. It is believed that not only the magnetic targeting capability but also the photothermal therapy capability of hybrid NPs could be improved by the use of FePt NPs.

Another key consideration in designing magnetic gold nanoshell for biomedical applications is structure. The approach to incorporate magnetic NPs with gold shell is also important. In this thesis, we designed a double-layered shell structure. FePt NPs are assembled to a thin but dense shell, as the interior layer while gold shell is deposit as the outside layer. Such a double-layered structure could bring a lot of advantages listed as below:

(1) The properties brought by functional NPs can be tuned according to the needs by controlling the layer thickness.

(2) It is possible to load a large number of magnetic NPs while occupy hollow space as less as possible, which is convenient in the case that both enhanced magnetic property

and high loading efficiency are needed.

(3) The mechanical/structural stability of the composite shells can be enhanced due to the presence of FePt shell, which is very meaningful, considering of the importance of

mechanical stability property for the delivery of encapsulated material and the structural instability of hollow gold shell. Magnetic FePt/Au nanoshells should have much better mechanical properties than mono-layered gold nanoshells or other magnetic gold nanoshells.

(4) The photothermal stability of the composite shells can be enhanced because the interior layer of FePt having a high thermal stability can play a role of hard template to support gold shell without hindering the light absorption of gold shell, and serve as energy absorbing centers, then the structure and diameter of the composite shells won't change significantly during and after laser irradiation.

Among the above four advantages of the double-layered structure, the last one is the most important and meaningful. Almost all of gold nanostructures having a plasmonic absorption band in NIR region, for example, silica-core gold nanoshells, gold nanorods, gold nanocages as well as their hollow structures, would more or less melt after a long-time or high-power laser irradiation, due to the heating generated by themselves. Surface modification or silica coating on the surface can be helpful for solid gold nanostructures to improve the thermal stability, but not useful for hollow gold nanostructures to prevent them from melting to solid particles. Therefore, it is believed that to build a double-layered structure is an effective solution for the issue of photothermal instability of gold shells. However, to our knowledge, by now no studies of FePt/Au double-layered NPs have been reported.

Additionally, although many studies about the photothermal capability of only magnetic particles or gold nanoshell have been reported, no studies about the combined photothermal capability of magnetic gold nanoshells, even in which not only plasmonic gold compound but also magnetic compound could convert light to heat.

1.4 Objectives, Motivation and Outline of Dissertation

The most important objective of the present study is to establish the fabrication protocol for double-layered FePt/Au nanoshells, to investigate their optical properties with the tunable SPR absorption in the region of NIR and high magnetic response for biomedical applications, and to demonstrate a potential for PTT using the nanoshells.

I propose two types of FePt/Au hollow porous nanoshells, which have different morphology and properties and were named as Type A and Type B. The three-step synthesis route for Type A is shown schematically in Figure 1.2. In short, firstly the plain silica nanospheres with negative charge are modified with cationic polyelectrolyte

in order to obtain positively charged silica templates, then a thin nanoshell consisting of the superparamagnetic FePt nanoparticles of 5 nm in size was synthesized using a polyol method in an argon/H_2 atmosphere, as reported by our group. In the next step, the as-prepared silica-core FePt nanoshells were functionalized with amine functional polymer. The gold shells were prepared using a seed-mediated growth of gold reported by Kah et al. The amine-functionalized surface of the FePt shells was seeded with Au NPs (1~3 nm in size). Then the gold shell is formed by reducing the additional gold ion on the Au-seeded surface of FePt nanoshell. It is important to mention that the successful modification of FePt nanoshell with amine functional group not only makes possible the binding between the Au seeds and FePt surface in the subsequent synthesis step, but also leads to the formation of gold shell with a good quality because a high-quality amine polymer layer could permit a high surface coverage of Au seeds on the FePt nanoshell. Therefore, in this thesis, the polymer kind, the polymer molecule and the number of polymer layers were changed to obtain a thin and smooth shell of gold to optimize optical properties and their effects on the quality of gold shells were investigated. Finally, the removal of the silica template by alkaline treatment converts the core-shell composite to the hollow shell structure. The size and the density of the accumulated nanocrystals can be controlled by adjusting the synthesis conditions, which results in the tunable morphology and properties of hollow nanoshells; the whole size of the shells can also be tuned by controlling the size of silica templates. In this synthesis route, the enhanced magnetic property can be obtained by increasing the number of FePt NPs. The SPR absorption in the NIR regain can be obtained by controlling the morphology of the gold shell and the whole particle size. The size and number of the pores on the shell surface can be tuned by adjusting the density of the nanocrystals of each shell.

It is reported that the photothermal capability of gold shells greatly depends on the morphology of the shells. Inspired by this, I designed another synthesis route aimed at obtaining another type of FePt/Au hollow nanoshells (Type B), which have a lot of improvements in both morphology and properties compared with Type A. The synthesis route of Type B includes four steps and is also shown in Figure 1.2. The first two steps and the last step of Type A are completely same with those of Type A. The only difference between the synthesis route of Type A and Type B is whether the FePt/Au shell is treated by supercritical fluid before the removal of silica cores. In the present thesis, supercritical ethanol treatment was proposed to optimize the morphology and properties of the shells for the expanded applications. During the thermal treatment of

supercritical ethanol, metal NPs melt and adjacent NPs fused together on the silica cores, resulting in the enlarged pores in the shell with a network structure. At the same time, a lot of the factors of the nanoshell, such as the crystal size and structure of metal NPs, the roughness and thickness of the shell also changed together, and these changes could be guided to the various directions based on the different needs, by controlling the thermal-treatment conditions (temperature, pressure and time). It should be noticed that the enlarge of pore size affect not only the optical property of the shell, but also the structural stability. Therefore, in order to obtain stable structure, two following things become important and necessary: (1) to evaluate the required particle density of each shell; (2) to optimize the thermal-treatment conditions.

In this thesis, two different synthesis routes to fabricate two types of the hollow magnetic FePt/Au nanoshell having a strong NIR absorption for PTT, excellent magnetic property and large cavity for magnetically enhanced targeting delivery are proposed: (1) synthesis of silica-core/FePt/Au double-layered shell composite particles with small pores and their hollow structure, (2) synthesis of silica-core/FePt/Au double-layered shell composite particles with enlarged pores and improved properties which were obtained by treating the composite particles using supercritical ethanol.

Firstly, the synthesis of FePt nanoshells on silica-core in various conditions and the controls of the whole particle size and the morphology are discussed in Chapter 2.1. Secondly, the plasmonic gold shells are deposited via two-step seed-mediated growth method on the prepared silica-core FePt nanoshells whose surface was modified by an amine polymer in advance, and the effect of different polymer interlayers and the dependences of deposition conditions are investigated in Chapter 2.2. Thirdly, hollow porous FePt/Au nanoshells with enlarged pores (Type B) are fabricated by thermal treatment of silica-core/double-layered FePt/Au nanoshell composites, and their morphology, structure and properties are discussed and compared with those of Type A in Chapter 3. Finally, the photothermal capabilities of these magnetic gold nanoshells are demonstrated and compared in Chapter 4. The results obtained in the present study are summarized, and general conclusions are described in Chapter 5.

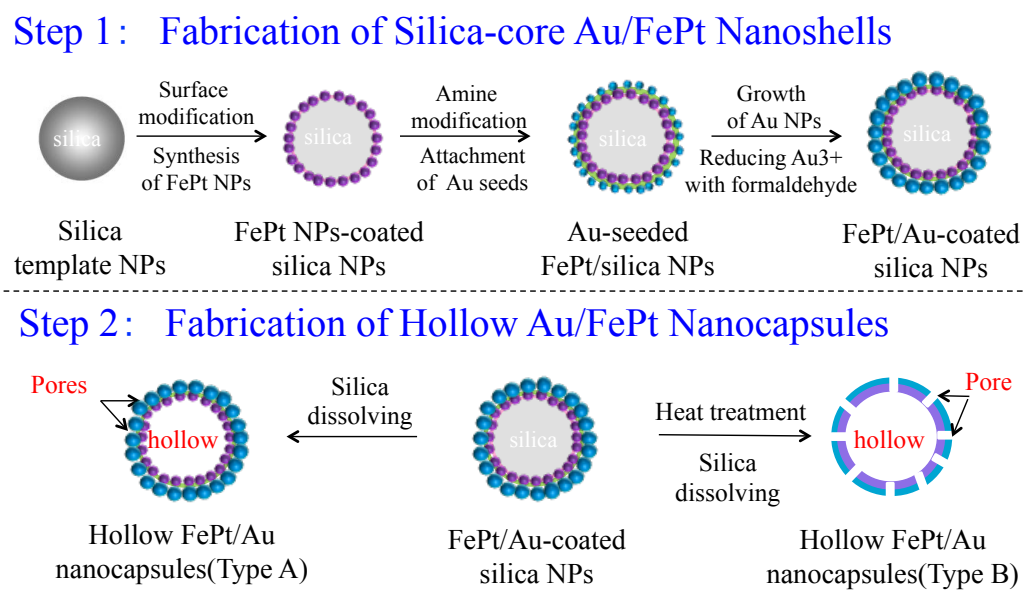

Figure 1.2 Fabrication process for hollow FePt/Au nanoshells

Reference

[1]. Ferlay J, Soerjomataram I, Ervik M, et al. GLOBOCAN 2012 v1.0, Cancer incidence and mortality worldwide: IARC Cancer Base No. 11 [Internet]. Lyon, France: International Agency for Research on Cancer, <http://globocan.iarc.fr>; 2013 [accessed 08.15].

[2]. Wust P, Hildebrandt B, Sreenivasa G, et al. Lancet Oncol 2002; 3: 487-97.

[3]. Song CW, Lokshina A, Rhee JG, Patten M, Levitt SH. IEEE Trans Biomed Eng 1984, BME-31:9–16.

[4]. Courtney M. Townsend. Sabiston textbook of surgery: Philadelphia, PA: Elsevier Saunders. p. 236. ISBN 978-1-4377-1560-6.

[5]. Simon CJ, Dupuy DE, Mayo-Smith WW Radiographics. 2005 Oct; 25 Suppl 1():S69-83.

[6]. K.Hrmann, K. U., Michel, M. S., Gaa, J., Marlinghaus, E. & Alken, P. (2002) J. Urol. 167, 2397–2403.

[7]. R. Medvid, A. Ruiz, R.J. Komotar, J.R. Jagid, M.E. Ivan, R.M. Quencer, and M.B. Desai.June 25, 2015

[8]. D. Ortega and Q. A. Pankhurst, Magnetic hyperthermia, in Nanoscience: Volume 1: Nanostructures through Chemistry, P. O'Brien, Editor. 2013, Royal Society of Chemistry: Cambridge. p. 60-88

[9]. Hirsch, L.R., Stafford, R.J., Bankson, J.A., Sershen, S.R., Rivera, B., Price, R.E., Hazle, J.D. , Halas , N.J. and West , J.L. (2003) Proceedings of the National Academy of Sciences of the United States of America , 100 , 13549 – 54 .

[10]. Leatherdale, C.A., Woo, W.K., Mikulec, F.V. and Bawendi, M.G. (2002). The Journal of Physical Chemistry B, 106, 7619 – 22.

[11]. Kang B, Mackey MA, El-Sayed MA (2010). J Am Chem Soc 132:1517–1519

[12]. Sheparovych R, Sahoo Y, Motornov M, Wang SM, Luo H, Prasad PN, et al. Chem Mater 2006;18:591-3.

[13]. Nathalie Schleicha, Chrystelle Pob, Damien Jacobsa, b, Bernard Ucakara, Bernard Gallezb, Fabienne Danhiera, 1, Véronique Préata, Journal of Controlled Release Volume 194, 28 November 2014, Pages 82–91

[14]. Chen Y-S, Frey W, Kim S, Kruizinga P, Homan K, Emelianov S. Nano Lett. 2011;11(2):348–54. 4.

[15]. T. Castro, R. Reifenberger, E. Choi, and R. P. Andres, Phys. Rev. B 42, P. Buffat and J. Borel, Phys. Rev. A 13, 2287,1976,.

[16]. C. Radloff and N. J. Halas.Appl. Phys. Lett., Vol. 79, No. 5, 30 July 2001

[17]. H H.-P. Liang, L.-J. Wan, C.-L. Bai, and L. Jiang, Journal of Physical Chemistry B, vol. 109, no. 16, pp. 7795–7800, 2005.

[18]. Kobayashi Y, Horie M, Konno M, et al. J Phys Chem B 2003;107 (30):7420–7425.

[19]. Z.-S. Zhang, Z.-J. Yang, X.-L. Liu, M. Li, and L. Zhou, Scripta Materialia, vol. 63, no. 12, pp. 1193–1196, 2010.

[20]. S. Preciado-Flores, D. Wang, D. A. Wheeler et al., Journal of Materials Chemistry, vol. 21, no. 7, pp. 2344–2350, 2011.

[21]. S. Preciado-Flores, D. Wang, D. A. Wheeler et al., Journal of Materials Chemistry, vol. 21, no. 7, pp. 2344–2350, 2011.

[22]. C. Liu, W. H. Dong, M. Liu, Y. Fan, and L. Zhen, Acta Chimica Sinica, vol. 67, no. 16, pp. 1825–1828, 2009.

[23]. X. Zhong, Y.-Q. Chai, and R. Yuan, Talanta, vol. 128, pp. 9–14, 2014.

[24]. C. Graf and A. van Blaaderen, Langmuir, vol. 18, no. 2, pp. 524–534, 2002.

[25]. J. Z. Zhang and C. Noguez, Plasmonics, vol. 3, no. 4, pp. 127–150, 2008.

[26]. You J, Zhang G, Li C. ACS Nano 2010;4: 1033–41.

[27]. You, R. Zhang, G. D. Zhang et al., Journal of Controlled Release, vol. 158, no. 2, pp. 319–328, 2012.

[28]. J. You, R. Zhang, C. Y. Xiong et al., Cancer Research, vol. 72, no. 18, pp. 4777–4786, 2012.

[29]. W. Lu, G. Zhang, R. Zhang et al., Cancer Research, vol. 70, no. 8, pp. 3177–3188, 2010.
[30]. K. M. Haas and B. J. Lear, Nanoscale, 2013, 5, 5247–5251
[31]. Lu W, Zhang G, Zhang R, et al. Cancer Res 2010;70 (8):3177–3188.
[32]. Heman Burhanalden AbdulrahmanJan KrajczewskiDorota Aleksandrowskaand Andrzej Kudelski .J. Phys. Chem. C, 2015, 119 (34), pp 20030–20038
[33]. V. Salgueirino-Maceira, M. A. Correa-Duarte, M. Farle, A. Lopez-Quintela, K. Sieradzki, R. Diaz, Chem. Mater. 2006, 18, 2701.
[34]. X. J. Ji, R. P. Shao, A. M. Elliott, R. J. Stafford, E. Esparza-Coss, J. A. Bankson, G. Liang, Z. P. Luo, K. Park, J. T. Markert, C. Li, J. Phys. Chem. C 2007, 111, 6245.
[35]. Rizia Bardhan, Wenxue Chen, Carlos Perez-Torres, Marc Bartels, Ryan M. Huschka, Liang L. Zhao, Emilia Morosan, Robia G. Pautler, Amit Joshi,* and Naomi J. Halas Nanoshells with Targeted Simultaneous
[36]. Kim, J.; Park, S.; Ji, E. L.; Jin, S. M.; Lee, J. H.; Lee, I. S.; Yang, I.; Kim, J.-S.; Kim, S. K.; Cho, M.-H.; Hyeon, T. Angew Chem Int Ed 2006, 45, 7754–7758.
[37]. Yong Taik Lim,Mi Young Cho,Jin Kyeong Kim,Seol Hwangbo,and Bong Hyun Chung. ChemBioChem 2007, 8, 2204 – 2209
[38]. J. Yang, H. I. Elim, Q. Zhang, J. Y. Lee, W. Ji, J. Am. Chem. Soc. 2006, 128, 11 921.
[39]. Maenosono, S.; Saita, S.. IEEE Trans. Magn. 2006, 42, 1638−1642.
[40]. Maenosono, S.; Suzuki, T.; Saita, S.. J. Magn. Magn. Mater. 2008, 320, L79−L83.
[41]. Nandwana, V.; Elkins, K. E.; Poudyal, N.; Chaubey, G. S.; Yano, K.; Liu, J. P. J. Phys. Chem. C 2007, 111, 4185.
[42]. J. Mater. Chem., 2010, 20, 61–64
[43]. J. Phys. Chem. C 2015, 119, 16374−16382
[44]. Sun, S.; Murray, C. B.; Weller, D.; Folks, L.; Moser, A.. Science 2000, 287, 1989−1992.
[45]. J. Lee et al./Multifunctional Magnetic Gold Nanocomposites Adv. Funct. Mater. 2008, 18, 258–264
[46]. Wang, H.; Brandl, D. W.; Le, F.; Nordlander, P.; Halas, N. J. Nano Lett. 2006, 6, 827–832.
[47]. Yu, T.; Li, P.; Tseng, T.; Chen, Y. Nanomedicine. 2011, 6, 1353–1363.
[48]. Liao, M.; Lai, P.; Yu, H.; Lin, H.; Huang, C. Chem. Commun. 2012, 48, 5319–5321.
[49]. Liao, M.; Lai, P.; Yu, H.; Lin, H.; Huang, C. Chem. Commun. 2012, 48, 5319–5321.

[50]. Chu, M.; Shao, Y.; Peng, J.; Dai, X.; Li, H.; Wu, Q.; Shi, D.. Biomaterials 2013, 34,4078–4088.
[51]. Qin W, Lohrman J, Ren SQ.. Angew Chem Int Ed 2014;53:7316e9.
[52]. S. Shen et al. / Biomaterials 39 (2015) 67e74 on
[53]. C.L. Chen, L.R. Kuo, C.L. Chang, Y.K. Hwu, C.K. Huang, S.Y. Lee, et al. Biomaterials, 31 (2010), pp. 4104–4112
[54]. C.-L. Chen et al. / Biomaterials 34 (2013) 1128e1134
[55]. Wu, J.; Hou, Y.; Gao, S. Nano Res. 2011, 4, 836− 848.
[56]. Wu, J., Hou, Y. & Gao, S. Nano Res. (2011) 4: 836. doi: 10.1007/s12274-011-0140-y
[57]. N. Kostevšek, K. ŽužekRožman, M. Arshad, M. Spreitzer, SpomenkaKobe, and S. Šturm, *J.* Phys Chem C 2015 119 (28), 16374-1638.

Chapter 2 Synthesis of Silica-FePt/Au Core-Shell Nanospheres

2.1 Preparation of silica-FePt Core-shell Nanospheres

2.1.1 Introduction

The study on hollow FePt nanoshells as magnetic drug carriers for cancer treatment had been first reported by our group [1,2,3]. This hollow magnetic nanoparticle consisting of a thin FePt shell of 5 nm in thickness and a cavity with the diameter of about 320 nm have an excellent delivery capacity for carrying drugs or genes. To obtain such shell structured nanoparticles, silica nanoparticles were used as a template. They were modified by a cationic polymer of poly (diaryldimethylammonium chloride) (PDDA). FePt nanoparticles of 5 nm in size were deposited on the surface of PDDA-modified silica particles via a polyol method and then the core-shell structured silica/FePt nanoparticles were obtained. Finally dissolving the silica template particles with a NaOH solution results in the formation of the hollow magnetic capsules as the final product. The FePt shell also exhibits a ferromagnetic property at room temperature because the small FePt nanoparticles (3-4 nm) had an ordered-alloy phase. The polyol process is the most common method to fabricate FePt NPs [4]. In this process, the polyol of tetraethylene glycol (TEG) acts as both of a solvent and a reducing agent for precursors. Figure 2.1 shows the fabrication strategy of FePt core-shell particles. In the case of magnetically guided DDS, the nanometer-thick magnetic shell is advantageous for a dramatic enhancement of the drug loading capacity and a reduction in the magnetic

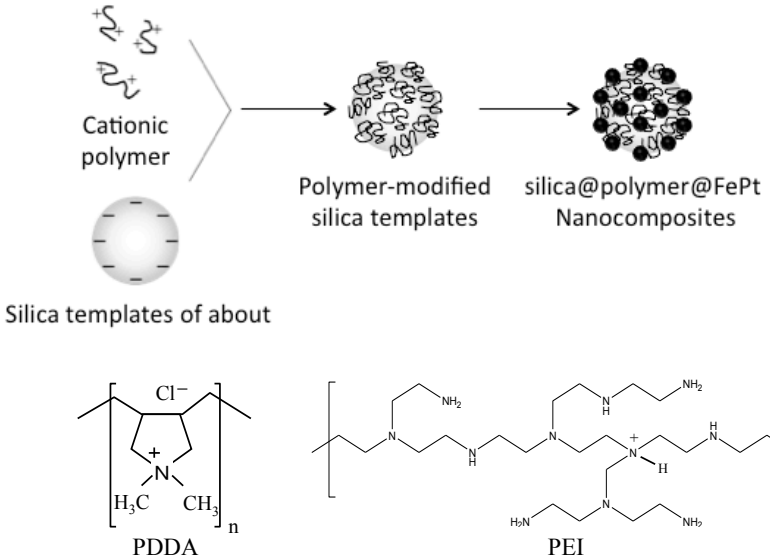

Figure 2.1 Fabrication schemes of silica-FePt core-shell nanospheres and structure of PDDA (left) and PEI (right)

components administered. Magnetic properties, such as magnetic susceptibility and the blocking temperature, are manipulated with maintaining the particle size and the shell thickness through varying the synthesis conditions. The diameter of the FePt nanoshells can be easily tuned by changing the size of the template particles and the shell thickness. Recent study of this composite nanoparticles showed that a porous capsule composed of fused FePt nanoparticles could be obtained by the thermal treatment of silica-FePt core-shell nanospheres. Water-soluble anti-cancer drugs could be loaded into the hollow space of the FePt capsules. The excellent magnetic property and high drug loading capacity of the hollow FePt nanoshell suggest applicability of hollow FePt nanoshell as a drug carrier in magnetically guided drug delivery system [2,3].

In this thesis, silica-FePt core-shell nanospheres were utilized as a magnetic nanoshell to combine with a gold shell considering their advantages and conveniences. The silica nanospheres with two different diameters of 320nm and 120nm were used to investigate the effects of the size of the silica cores on the morphology and optical property of FePt/Au nanoshells, and in the case of smaller silica cores (120nm), cationic polyelectrolyte poly (ethyleneimine) (PEI) with lower molecular weight was utilized as a cationic polyelectrolyte for surface modification, instead of PDDA. Various silica-FePt core-shell nanospheres with the different thickness of FePt shell had been synthesized to investigate the effects of the density of FePt NPs on the structural stability of hollow FePt/Au nanoshells.

2.1.2 Materials and Methods

2.1.2.1 Materials

Amorphous silica particles (average diameter: 320 nm and 120 nm,); Fe (acetylacetonate)$_3$ (powder, Sigma-Aldrich); Pt (acetylacetonate)$_2$ (powder, Sigma-Aldrich), tetraethylene glycol (TEG) (99%, Sigma-Aldrich), PDDA aqueous solution (average molecular weight: 100 kg/mol, 35wt% in water, Sigma-Aldrich) were purchased and used as received. Absolute Ethanol (C_2H_5OH, 99.5%) an double distilled water Absolute Ethanol (C_2H_5OH, 99.5%) and deionized water was used during reaction and washing as solvent.

2.1.2.2 Methods

2.1.2.2.1 Modification of Silica Template Particles

80 mg of amorphous silica particles (average diameter: 320 nm) was added into 5 mL of pure water to obtain 5 mL of an aqueous dispersion of silica particles, following the

addition of 25 mL of 5 wt% PDDA aqueous solution. After the sonication of 15 min and the stirring of 2h,the PDDA-modified silica particles were collected and redispersed in TEG (50 mL) for the next step.

PEI-modified silica particles (average diameter: 120 nm) were fabricated by mixing 5 mL of an ethanol dispersion of amorphous silica particles (10~80 mg) with 25 mL of PEI ethanol solution (5 wt%). After the stirring of 2h,the PEI-modified silica particles were purified by washing with water three times. The PEI-modified silica template particles were then redispersed in TEG (50 mL) for the next step.

2.1.2.2.2 Synthesis of Silica-FePt Core-shell Nanospheres

FePt nanoparticles were deposited by using the following modified polyol method: A mixture of Fe (acetylacetonate)$_3$ (0.212 mmol), Pt (acetylacetonate)$_2$ (0.192 mmol), modified-silica template particles (13.3 mg, 26.6 mg, 40 mg) and TEG (50 mL) a solvent and reducing agent was added to a 100 mL three-necked, round-bottom flask and then heated under strong stirring at 503 K by refluxing for 2 h in an inert gas (Ar/H_2). After the reaction, the products were collected by centrifugation and washing with ethanol three time.

2.1.2.3 Characterization

Silica-FePt Core-shell nanospheres were characterized by powder x-ray diffraction (XRD) using an X-ray diffractometer (Rigaku, RINT 2100V) for crystal structure, and transmission electron microscopy (TEM, Hitachi, H-8100) for morphology and size distribution. Zeta potentials of various particles were measured using a Zetasizer Nano (Malvern) and a Nano Partica (Horiba). Magnetic properties were measured by a physical property measurement system (Quantum Design Corp. PPMS).

2.1.3 Results & Discussions

2.1.3.1 Size Control by Changing Size of Silica Templates

FePt nanoparticles were synthesized at 503 K in the presence of polymer-modified silica particles with two different sizes of 120nm (13.3 mg) and 320nm (40 mg) in diameter, and their TEM images are shown in Figure 2.2. To obtain the same radio of FePt precursor to surface area of silica particles, the weight of 120 nm silica was decreased to 13.3 mg, one third of the weight of 320 nm silica since the surface area of 120 nm silica is three times more than that of 320 nm silica. Two kinds of polymer-modified silica particles were entirely covered with FePt nanoparticles. These

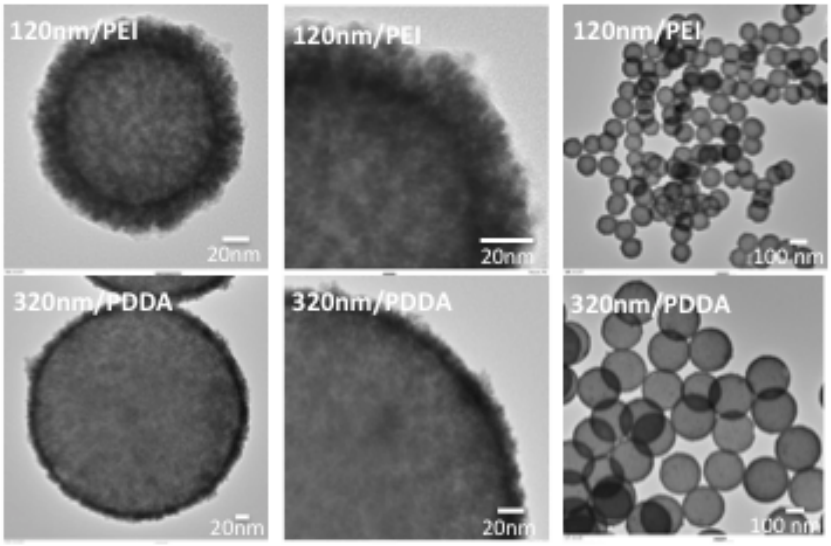

Figure 2.2 TEM images of silica-FePt core-shell nanospheres synthesized in the presence of two kinds of polymer-modified silica templates with different sizes and surfaces.

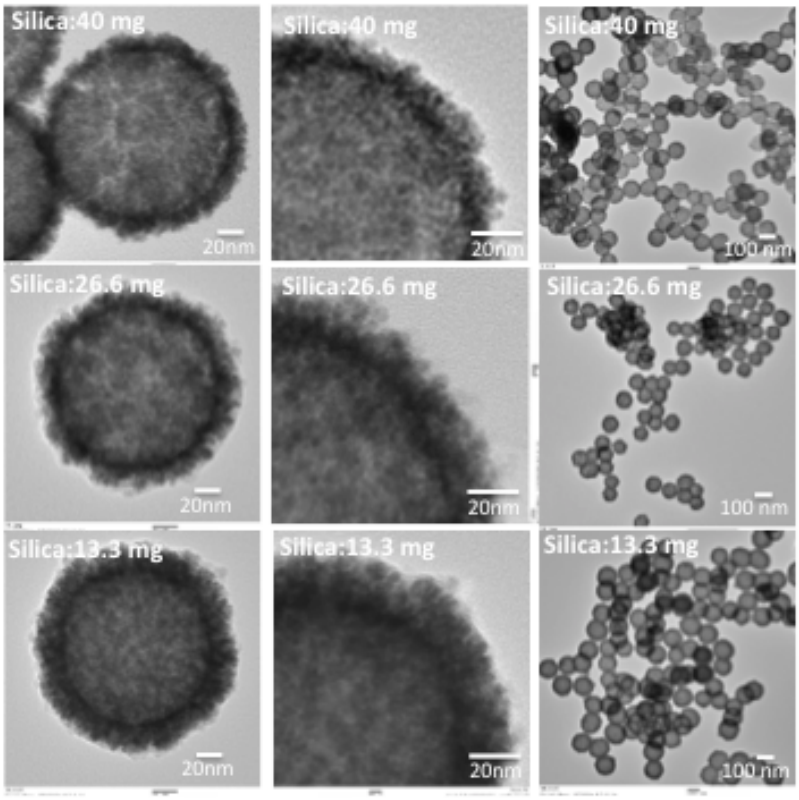

Figure 2.3 TEM images of silica-FePt core-shell nanospheres synthesized by changing the silica weight to (A) 13.3 mg, (B) 26.6mg and (C) 40 mg respectively.

results suggest that both PDDA and PEI can play the role of the cationic polyelectrolyte to modify silica in the synthesis of silica-FePt core-shell nanospheres. Based on the TEM images, the FePt shells on the silica of 120 nm have a thickness of about 20 nm whereas the FePt shells on the silica of 320 nm have a thickness of about 10 nm. The accumulation of FePt nanoparticles onto PDDA-modified silica particles of 320 nm in diameter was more uniform than that of PEI-modified silica particles of 120nm in diameter.

2.1.3.2 Morphology Control by Changing Amount of FePt Precursor

FePt nanoparticles were synthesized at 503 K in the presence of PEI-modified silica particles of 120nm in diameter with the different amount of 13.3 mg, 26.6 mg and 40 mg, and their TEM images are shown in Figure 2.3. The size of the FePt nanoparticles was not obviously affected by changing the weight ratio of templates to precursors used in their syntheses; only the amount of FePt nanoparticles accumulated on the surface of the PEI-modified silica particles changed, and a thinner shell was obtained by increasing the weight of silica. The thickness of FePt shell was 20nm, 15 nm and 11 nm when the silica weight was 13.3 mg, 26.6 mg and 40 mg, respectively. These various silica-FePt core-shell nanospheres with the different thickness will be used as the template in the next step of the growth of gold shells. It should be noticed that the FePt shell becomes rough and nonuniform when the silica amount is less than 13.3 mg whereas the shell was not completely covering the surface of the silica cores when the silica amount is more than 40 mg.

2.2 Deposition of Au Nanoshells on Silica-FePt Core-shell Nanospheres

2.2.1 Introduction

Light-absorbing metallic nanoparticles have been attracted much attention as photothermal (PTT) nanoagents and the light-absorbing effectiveness of these nanoparticles that greatly affects the efficiency of PTT treatment strongly depends on their plasmon resonance properties. Gold nanoshells consisting of a dielectric silica core surrounded by a thin gold shell have attracted much attention because of the following two important optical features:

(1) They have high absorption efficiency of light due to the intensified interaction with the electromagnetic field by a phenomenon known as surface plasmon resonance (SPR) [5~8];

For a noble metal particle, the oscillating electromagnetic field of the light induces a collective coherent oscillation of the free electrons of the metal when irradiated by light and the amplitude of the electron oscillation along the direction of the electric field of the light can reach maximum for a specific-frequency light. This unique phenomenon in noble metal nanoparticles (also called plasmonic nanoparticles) is called surface plasmon resonance (SPR)[9,10]. The SPR band intensity and wavelength can be adjusted by changing all the factors affecting the electron density on the particle surface, such as the metal material, particle size, shape, structure, composition and the dielectric constant of the surrounding medium, as theoretically described by Mie theory [11,12,13]. The surface plasmon resonance leads to strong electromagnetic fields on the particle surface and these excited plasmon electrons relax in two different ways: absorption and scattering. Additionally, the strongly absorbed energy is quickly converted to the metallic lattice in the form of heat, which is subsequently transferred to the surrounding medium resulting in the temperature increase of the surrounding medium. This is the basis of all plasmonic nanoparticle-mediated PTT applications.

(2) Their spectral and absorption/scattering ratio can be straightforwardly tuned by varying their geometry and composition [14,15,16].

The basis for this convenient tunability in optical properties of gold nanoshells whose mode is showed in Figure 2.4 can be explained in terms of the plasmon resonance hybridization showed in Figure 2.5. In the case of a gold nanoshell, the nanostructure can be decomposed into a solid gold sphere and a hollow cavity surrounded by a bulk gold. Subsequently, the plasmon response of a gold nanoshell can be taken as an interaction between the plasmon response of a sphere and the plasmon response of a cavity. When these two plasmon resonance hybridize, the interaction of the plasmons on the inner and outer surfaces of the shell results in two plasmon modes: the lower energy symmetric called as “bonding” plasmon where the plasmons of the sphere and the cavity are out of phase, and the higher energy antisymmetric called “antibonding” plasmon in which the plasmons of the sphere and the cavity are in phase[17,18]. This plasmon resonance behavior of the gold nanoshell can be understood using the plasmon hybridization model and calculated using Mie theory. The electron gas deformations can be decomposed as spherical harmonics of order l and then the plasmon resonances of the sphere ($\omega_{s,l}$) and the cavity ($\omega_{c,l}$) are given as:

$$\omega_{S,l} = \omega_B \sqrt{\frac{l}{2l+1}}$$

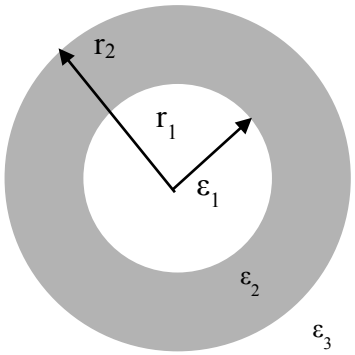

Figure 2.4 Geometry of gold nanoshell with indicated radii (r) and three dielectric functions corresponding to the core, shell and ambient medium (ε).

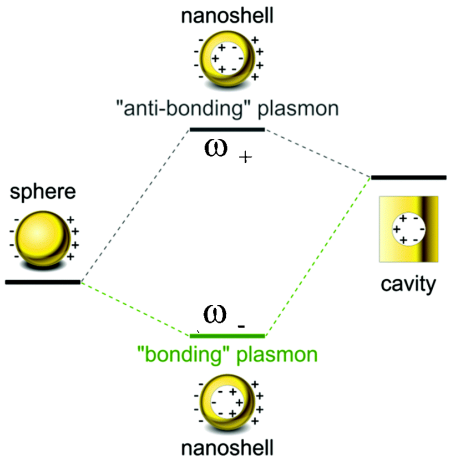

Figure 2.5 Schematic of Plasmon hybridization for a gold nanoshell.

and

$$\omega_{C,l} = \omega_B \sqrt{\frac{l+1}{2l+1}}$$

where ω_B is the bulk plasma frequency. Thus the frequencies of these two resonances ($\omega_{l\pm}$) are given by

$$\omega_{l\pm}^2 = \frac{\omega_B^2}{2}\left[1 \pm \frac{1}{2l+1}\sqrt{1+4l(l+1)\left(\frac{r_1}{r_2}\right)^{2l+1}}\right]$$

where r_1 refers to inner radius and r_2 refers to outer radius. It is obvious that the strength of the interaction between these two plasmons is controlled by the ratio of r_1 / r_2. For

bonding plasmon modes, a larger value of r_1 / r_2 corresponding to a thinner shell produces lower energy resulting in stronger interaction and a large red-shift of the nanoshell resonance compared to the sphere resonance. Therefore, the appearance of NIR absorption has been explained as a result of the plasmon resonance hybridization [17,18] and we can control the red-shift the plasmon resonance of gold nanoshells from the visible to near infrared region (NIR) efficiently by adjusting the core/shell ratio (r_1 / r_2). For gold nanoshells, the extinction cross-section is given as

$$\sigma_{\text{ext}}(\omega) = \frac{2\pi\omega}{c}\text{Im}(\alpha(\omega)),$$

where c is the speed of light, ω is the angular frequency and a is the complex polarizability of the particle.

$$\alpha(\omega) = 4\pi\varepsilon_o r_2^3 \left| \frac{\varepsilon_2\varepsilon_a - \varepsilon_3\varepsilon_b}{\varepsilon_2\varepsilon_a + 2\varepsilon_3\varepsilon_b} \right|, \text{ where } \varepsilon_o = 8.85 \times 10^{-12}\,\text{Fm}^{-1}$$

where $\varepsilon_a=\varepsilon_1(3-2P)+2\varepsilon_2P$, $\varepsilon_b=\varepsilon_1P+\varepsilon_2(3-P)$,$P=1-(r_1/r_2)^3$. From the equation, it is evident that the absorption, scattering and extinction cross-sections of a gold nanoshell are a sensitive function of the inner and outer radius of the metallic shell, which indicates that it is possible to realize the optimization of the optical cross-sections of gold shells for a specific frequency (wavelength).

A fabrication of gold nanoshells always involves multistep synthesis procedure. The most commonly used approach to fabricate silica/gold nanoshells is a bottom-up wet chemical synthesis including the attachment of gold colloids on functionalized silica surface, followed by the growth of gold shell based on electroless plating; this is named as a seed-mediated growth process. In this approach, the silica surface functionalization is crucial for the binding between gold colloids and the silica surface, where these gold colloids will serve as Au seeds for shell growth. Thus many researches regarding this process focused on the investigations of the influence of silica surface functionalization. Various organosilanes containing functional groups with high affinity to gold, such as amino ($-NH^2$) or mercapto (-SH) group were chose to functionalize the surface of silica [19,20], Some functional polymers containing multiple $-NH^2$ groups, such as polyethyleneimine (PEI) [21] or poly (diallyldimethylammonium chloride) (PDDA) were also used to modify the silica surface [22]. The amino organosilanes were most frequently used for functionalization of silica surface due to their uniform and relatively

high surface coverage (up to 30%) with gold nanoparticles, which is very important for the formation of a smooth continuous shell.

Gold is grown with electroless plating onto the nucleation sites via reducing gold ion by a reductant. The morphology and thickness of shell are controlled by the amount of Au salt solution while affected by the reducing capability of the reductant. Therefore, there are many reported studies on the influence of the reducing agents on the shell formation because the reducing agents critically affect the growth of gold shell as well as the quality of gold shell. Sodium borohydride was first used as a reducing agent however formaldehyde is the most often used as a mild reducing agent in the synthesis of gold nanoshells [23]. Such as glucose [24], ascorbic acid [25], hydroxylamine [26] and CO [27] were also used as a reducing agent.

In the present thesis, the two-step seed-mediated growth process discussed above was chose to synthesize a gold shell on the surface of FePt shell, due to the convenience of this method in tuning the SPR absorption of gold shell. Terentyuk et al. found that for providing tissue hyperthermia by 808-nm laser diode, the best was using silica-core gold nanoshells with the ratio of core diameter to shell thickness as 140/20 nm, because these particles have extinction maximums at this particular wavelength. In their study, not only the theoretical spectra but also experimental spectra demonstrated this result. Therefore, the gold shell of 20 nm in the thickness was designed considering that the diameter of silica cores is about 120 nm while the total size of the as-prepared FePt shell is about 140 nm in this study [28]. However the synthesis process of gold shell is very sensitive and the growth of gold shell is fast within several seconds. Although the two-step seed-mediated growth procedure have been developed for several ten years, it is still difficult to control the morphology and the thickness of gold shells. If the reaction cannot be controlled properly, it eventually leads to the formation of a poor-quality gold shell with a very large thickness or heterogeneous morphology or incomplete coverage. To obtain the designed particles, it is required to highly control each step of synthesis process to ensure complete coverage of FePt nanoshell with gold while limit the shell thickness within 20 nm.

To facilitate the binding of gold to the FePt shell, a functional interlayer between FePt shell and the Au shell is needed in the synthesis process (shown in Figure 2.6) because metal nanoparticles are rather difficult to attach to or grow on other metal nanoparticles. Branched polyethyleneimine (PEI), a cationic polyelectrolyte with high amine content was chosen as a linker to bridge the FePt shell with the gold shell here since it was found to be able to effectively enhance the attachment of Au NPs to the surfaces of

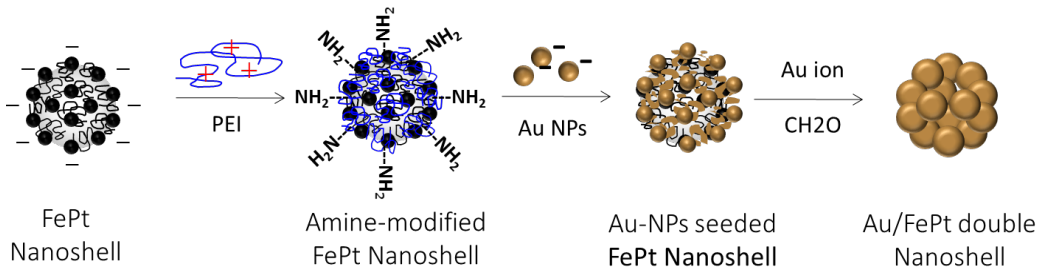

Figure. 2.6 Synthesis process of Au shell on the surface of silica-core FePt nanoshells

silica or iron oxide nanoparticles. The positively charged PEI binds to the negatively charged FePt shell through electrostatic self-assembly to form a stabilizing polyelectrolyte layer and the amine group of the PEI is available to attach to small Au nanoparticles. The negatively charged Au NPs were attached through electrostatic attraction and weak covalent bonding between the aminated nanoparticles and the negatively charged Au NPs. Therefore, the modification conditions and quality of amine groups on the substrate surface strongly affects the quality of Au shells. It is well known that the location of SPR band of gold nanoshells greatly depends on their morphology and shell thickness. To obtain a high-quality gold shell with the SPR band in NIR region, firstly we optimized the modification conditions of PEI layer. A series of PEI layers were prepared on the FePt nanoshells under various conditions and characterized by zeta potential measurement. The effects of various modification conditions of PEI layer are discussed in this chapter. Additionally, besides cationic polyelectrolyte PEI, non-electrolyte poly (N-vinyl-2-pyrrolidone) (PVP) and another cationic polyelectrolyte PDDA also were utilized to modify the surface of FePt shells and the effect of the different functional group of polymer were investigated and discussed in this chapter.

The attachment process of Au seeds is also a key step for producing a smooth and thin gold layer [29]. The exposure of Au seeds to functionalized surface of templates led a higher initial coverage followed by the monolayer coverage of gold nanoparticles up to 25~30% due to electrostatic repulsion between the nanoparticles [30]. In the present thesis, two kinds of Au colloids as Au seeds were prepared from $HAuCl_4$ by using two common reducing agents, THPC and $NaBH_4$, separately. In the synthesis route in which THPC is a reducing agent, THPC plays the role of both the reducing agent and the stabilizing agent [31]. In the synthesis route in which $NaBH_4$ is the reducing agent, $NaBH_4$ reduces gold ions through the formation of hydrogen to produce gold NPs while polyvinylpyrroridone (PVP) works as the capping agent, and stabilizes the Au NPs by embedding particles in a shell of stabilizing molecules [32]. Au NPs resulting from

these two preparations are hereafter called THPC-Au and PVP-Au, respectively. The structure schemes of THPC, $NaBH_4$ and PVP are shown in Figure 2.7. The attachment of Au seeds onto the PEI-modified cores in the presence of these two kinds of Au colloids was investigated and the effects of Au seeds with the different particle size and surface properties were discussed in this chapter.

In order to form the gold shell, the small Au seeds were further grown via seed-mediated electroless plating, in which a dilute gold plating solution of $HAuCl_4$ and potassium carbonate (often referred to as K-gold) as the metal source was reduced by the reducing agent. The shell layer morphology depends on the reducing agent used in the metallization process [33]. Two kinds of the reducing agents with the different reducing capability including formaldehyde and hydroxylammonium chloride (see Figure 2.8) were utilized in the final step, the formation of gold shell. Here the reducing ability of hydroxylammonium chloride is stronger than that of formaldehyde. Their performances were discussed and compared in this chapter.

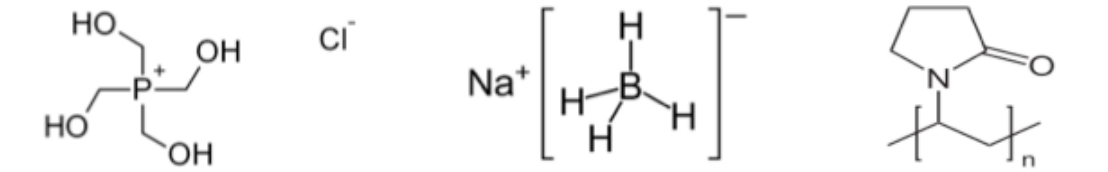

Figure 2.7 Schematic illustrations of structures of THPC, $NaBH_4$ and PVP

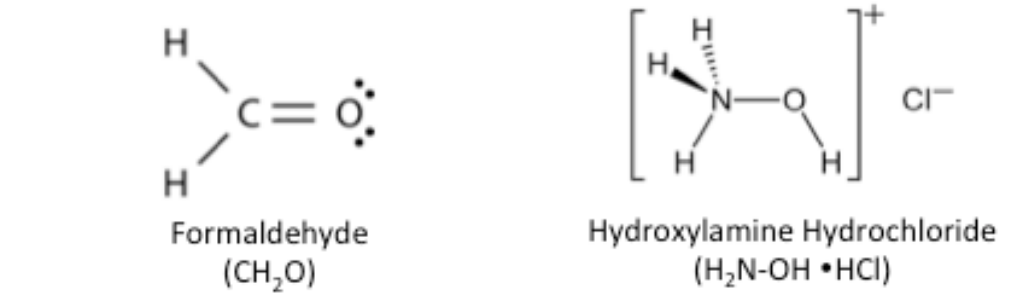

Figure 2.8 Schematic illustrations of structures and standard Redox potentials of formaldehyde and hydroxylammonium chloride

Additionally, a few other methods including (1) the direct growth of gold shell on the non-functionalized FePt surface using PVP-coated Au colloids and sodium borohydride ($NaBH_4$), (2) the formaldehyde stimulated shell growth on Sn-seeded particles and (3) the one-step polyol process of gold salts reduction on amino-functionalized FePt shells using EG or TEG as solvent and reducing agent, had been tried in this study, however the unfavorable experiment results forced us to give up them.

2.2.2 Materials and Methods

2.2.2.1 Materials

Amorphous silica particles (average diameter: 320 nm and 120 nm,); PDDA aqueous solution (average molecular weight: 100 kg/mol, 35wt% in water, Sigma-Aldrich); Polyethyleneimine (PEI, Mw: 1800); Polyethyleneimine (PEI, Mw: 25000); Polyethyleneimine (PEI, Mw: 750000); 3-Aminopropyl triethoxysilane (APTES, 97%), Polyvinylpyrroridone (PVP K-30, powder); Hydrogen Tetrachloroaurate (III) trihydrate ($HAuCl_4$, 99.99%); Tetrakis (Hydroxymethyl) Phosphonium Chloride (THPC, 80% solution); Sodium Tetrahydroborate ($NaBH_4$, Powder, 99.6%); Potassium Carbonate (K_2CO_3, Powder, 99.7%); Hydroxylamine hydrochloride (NH_2OH HCl, 97%);Formaldehyde (CH_2O, 37%); Sodium Hydroxide (NaOH, solid, JIS Special Grade) were purchased and used without any purification. Absolute Ethanol (C_2H_5OH, 99.5%) and deionized water was used during reaction and washing as solvent.

2.2.2.2 Methods

2.2.2.2.1 Modification of Silica/FePt Core-shell Nanoparticles

The surface of the silica/FePt core-shell nanoparticles with negative charge was functionalized with amine groups by treatment with branched polyethyleneimine (PEI).

Firstly, an aqueous suspension of silica/FePt core-shell nanoparticles was mixed with an aqueous solution of PEI. The mixture was sonicated for 2 h and then stirred for 12 h to complete the modification. The precipitate was purified by centrifugation and washing three times, and then redispersed in deionized water. PEI binds to the negatively charged surface of FePt shell through electrostatic attractions and the amine group of the PEI is available to attach to small Au colloids. These amine-terminated nanoparticles were redispersed immediately before the next step.

Six different types of PEI layers were prepared on the surface of FePt nanoshells using three kinds of PEI polymers with the different molecular weight (Mw:1800,

Table 2.1 Various PEI Polymer layers

Name	Components	Concentration	Ratio
Sample 1	PEI (Mw:2,000)	3%	
Sample 2	PEI(Mw:25,000)	3%	
Sample 3	PEI(Mw:750,000)	3%	
Sample 4	Mixed PEI(Mw:2,000+25,000)	3%	1:4
Sample 5	Mixed PEI(Mw:2,000+750,000)	3%	1:4
Sample 6	Mixed PEI(Mw:25,000+750,000)	3%	1:4

25000, 750000 $gmol^{-1}$). Their details were shown in Table 2.1.The concentration of all polymer aqua solutions was 3% and the ratio of the high molecular weight polymer to the low molecular weight polymer for mixed polymers was 1:4.

2.2.2.2.2 Attachment of Colloidal Au NPs as Seeds

Synthesis of THPC-Au Colloids. A THPC-Au colloid solution was prepared according to Duff et al [30]. First 0.5ml of freshly prepared 1M NaOH was added in 44.5 mL of ice-cold pure water, followed by the addition of 12μL of 80% THPC solution. The mixture was stirred for 5 min and then 4ml of 0.5wt% $HAuCl_4$ solution was added by drop-wise. Vigorously stirring was kept for 2h at ice bath. The final solution was refrigerated for at least 2 weeks before use.

Synthesis of PVP-Au Colloids. For the preparation of PVP-Au nanoparticles, the method described by N. R. Jana [31] with a slight modification was adopted. An aqueous solution (48.5mL) was prepared containing 0.015mM $HAuCl_4$ and 0.03mM PVP. Next, 1.5mL of freshly prepared 0.15mM $NaBH_4$ solution was added into the above solution while stirring. The solution turned deep wine-red immediately, indicating the particle formation. The final solution was refrigerated before use.

Synthesis of Au-seeded Silica/FePt core-shell Nanoparticles. First, 5 mL of suspension PEI-modified silica/FePt core-shell nanoparticles was added to an excess of 45 mL of gold colloid solution. The mixture was stirred for 1h and allowed to sit

overnight at 4°C to maximize the surface coverage of Au nanoseeds. The Au-seeded particles were purified by three cycles of centrifugation and wash, and then redispersed in 5 mL of pure water and used as described in the following subsection. The PEI-modified silica/FePt core-shell nanoparticles attached by gold colloids were named as Au-seeded PEI/FePt/silica. The ratio of silica/FePt core-shell nanoparticles to Au seeds is estimated from the total surface area of the template solution, the concentration and physical cross-section of the Au seeds, and assuming 25~30 % coverage of Au seeds on the surface of silica/FePt core-shell nanoparticles.

2.2.2.2.3 Growth of Au Shell

In order to form the gold shell, the small Au seeds that attached on Au-seeded silica/FePt core-shell nanoparticles was further grown via seed-mediated electroless plating, in which a dilute gold plating solution of $HAuCl_4$ and potassium carbonate (often referred to as K-gold) as the metal source was reduced by the reducing agent.

Synthesis of K-gold Solution. A 100ml of the K-gold solution was produced by the addition of 25 mg of potassium carbonate and 1.5mL of 1.0 wt% $HAuCl_4$ solution to 100 mL of pure water. The mixture was stirred for 2 h and then aged for a minimum of 24 h in the dark before it was used. The color of the solution slowly changed from yellow to colorless and the pH of the solution decreased to 7~8.

Synthesis of Gold Nanoshells 200 μL of the Au-seeded silica/FePt core-shell nanoparticles solution was added by drop-wise to 4 mL of the K-gold solution under vigorously stirring followed by the addition of the reducing agent (40~80 μL of formaldehyde or hydroxylamine hydrochloride). The solution changed from light black to blue black, indicating the formation of gold nanoshell. The magnetic gold nanoshells were collected and redispersed in pure water until use. UV-vis spectra were measured 1h after the reaction to confirm the formation of nanoshells.

2.2.2.3 Characterization

Silica-FePt/Au core-shell nanospheres were characterized by powder X-ray diffraction (XRD) using an X-ray diffractometer (Rigaku, RINT 2100V) for crystal structure, and transmission electron microscopy (TEM, Hitachi, H-8100), Scanning electron microscopy (SEM, Hitachi, S-4800) for morphology and size distribution. Zeta potentials of various particles were measured using a Zetasizer Nano (Malvern) and a Nano Partica (Horiba). Magnetic properties were measured by a physical property measurement system (Quantum Design Corp. PPMS).

The experimental extinction spectra of various samples were measured by UV–Vis spectroscopy (Jasco V-560). The sample solutions were typically placed in a rectangular cuvette (Malvern) with an internal width of 1 cm. The basic for the spectroscopy is that the machine measures the intensity of the desired range of wavelength of UV–Vis light passing through a sample solution (I_t), and compares it to the intensity of light before it pass through the sample solution (I_0) expressed in transmittance (T) or absorbance (A). The ratio of the light that passes through the cuvette is directly measured as Transmittance (T) defined as follows:

$$T = I_t/I_0 \text{ or } \% T = (I_t/I_0) \times 100$$

Absorbance (A) is defined as the amount of the light absorbed by the sample solution and is related to transmittance by the expression:

$$\text{Absorbance (A)} = -\log (T) = -\log (I_t/I_0)$$

Figure 2.9 shows what happens to light as it passes through a sample solution held in a cuvette. Sample nanoparticles may absorb light, scatter light, or both. The incident light may undergo absorption, reflection, interference, and scattering before it is transmitted. Thus the incident light is reduced in intensity due to absorption, reflection, interference and scattering of light. The change in light intensity can be given as:

$$\Delta I = I_0 - I_t = I_{absorbed} + I_{reflected} + I_{interference} + I_{scattering}$$

Normally, in order to measure just the amount of light absorbed by the sample particles, an appropriate control sample with just the same solvent without any sample particles is used as the reference. For most cases in which light scattering by sample nanoparticles can be negligible, the measured optical spectrum of the nanoparticles is almost entirely due to photon absorption by the nanoparticles. In such cases, the change in light intensity usually can be given as:

$$\Delta I = I_{absorbed} .$$

However, in the case of the gold nanoshell with the diameter more than 100 nm prepared in this study, light scattering cannot be negligible and the light is extinguished not only by absorption but also by scattering. The reduction of intensity of the incident light due to absorption and scattering is called extinction shown as follows;

$$\Delta I = I_{absorbed} + I_{scattering} = I_{extinction}.$$

The absorbance of the measured optical spectrum in this study actually reflects the

extinction (absorption and scattering) of samples. Thus, the absorbance spectrum of the gold nanoshell measured in this study was named as the extinction spectrum, in which the title of the vertical axis was referred to as "Extinction" while the horizontal axis was referred to as "wavelength". Additionally, it should be noticed that the unit of the vertical axis considered as [a.u.] in all the spectra and the comparison of extinction intensities between samples has no scientific meaning. In this thesis, the SPR wavelength of samples where the spectral intensity reaches to maximums was investigated because the photothermal conversion efficiency of gold nanoshells greatly depends on their SPR wavelength. The desired wavelength for gold nanoshells would be near 800 nm because the central wavelength of the mostly used laser source for PTT is 808 nm and biological tissue is also optically transparent at this wavelength. To obtain the desired wavelength, the surface morphology, the particle size and shell thickness were optimized in this study.

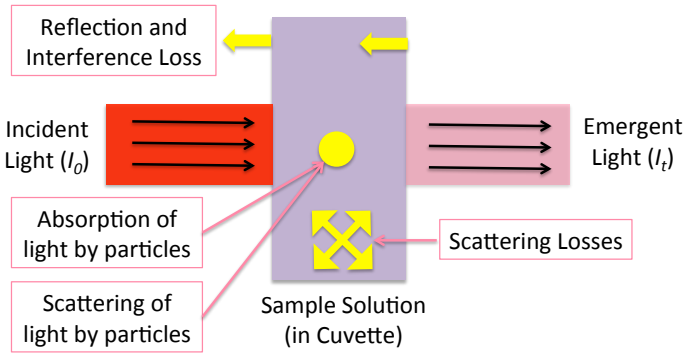

Figure 2.9 Schematic of transmittance of light through a sample solution in a cuvette. The incident light is reduced in intensity due to absorption, reflection, interference and scattering of light.

2.2.3 Results & Discussions

A gold nanoshell shown in Figure 2.10 was prepared successfully on the surface of 320nm silica-core FePt nanoshells (FePt shell: about 5 nm) when PEI is used as an interlayer. The obtained silica/FePt/Au nanoshells show uniform particle morphology and a uniform particle size distribution (see Figure 2.10 (e)). The thickness of gold shells observed in TEM images is about 15 nm. SEM images have revealed that the gold shell consisted of a lot of large gold clusters that grew from the Au seeds attached on the surface of silica/FePt shells, and the surface of silica/FePt/Au shell was rougher compared to the smooth silica/FePt shells. The study of SEM images also indicated that this gold layer grew on the surface of silica/FePt layer to form a double-layered

structure since the observed FePt shell was a smooth and complete layer.

Figure 2.11 shows the details of XRD patterns of FePt shell after Au seeding and the formation of gold shell. The details of XRD patterns of silica particles after Au seeding and the formation of gold shell also are presented in Figure 2.11. Their Au crystallite diameters are listed in Table 2.2. There are no obvious differences in Au crystallite diameters between the gold shells formed on the FePt shells and the gold shells formed on the silica particles, indicating that the presence of FePt shell did not have an obvious effect on the growth of gold shells.

The experimental spectra of silica/FePt shells and silica/FePt/Au shells were presented in Figure 2.12 (left). Silica particles or silica-core FePt nanoshells do not show any obvious absorption peak in the range of 300-900 nm. When these particles are coated with a thin gold shell, a broad but obvious extinction band peaking at the region of 700~850 nm in the experimental spectral curve of silica/FePt/Au shells is observed. Thus, the measurement of UV-Vis spectra can be an indirect technique to know the presence of a gold shell and monitor the growth of gold shells. Herein the SPR band of the NIR region in the UV-Vis spectra demonstrated the formation of continuous gold shells on the surface of silica/FePt shells. This change in the optical property caused the changes in the apparent color of aqueous solution of silica/FePt/Au shells shown in Figure 2.12 (right). After the fabrication of gold shells, the color of aqueous solution of silica/FePt shells changed from black to dark blue. To investigate the difference between the theoretical spectra calculated based on Mie theory and the experimental spectra, a gold shell of 20 nm in thickness was prepared on the FePt/silica shells with the diameter of 140 nm, and its TEM images and measured spectral curve are presented in Figure 2.13. The extinction band peaking at 817 nm was observed. As discussed before, Terentyuk et al. reported the calculated extinction peak of the silica-core gold nanoshells with the ratio of core diameter to shell thickness as 140/20 nm appeared around 810 nm [28]. There is a good correlation between calculated and measured spectra; however, the experimental curve is broader due to particle size heterogeneity.

The studies of MH curves of silica/FePt/Au shells at 300K revealed that the nanohybrids exhibited superparamagnetic properties; the magnetization at 10 kOe was 2.5 emu/g, whereas it was 5 emu/g for FePt shells. The decreased magnetization compared to that of FePt shells should be due to the large volume of Au nanoshells that resulted in the decreased Fe content percent. The magnetic FePt shell of the hybrid

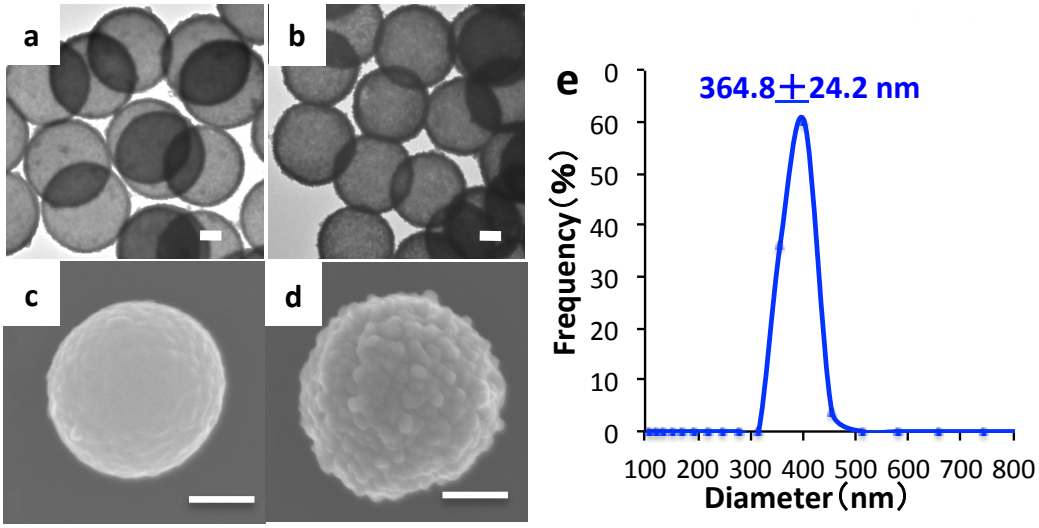

Figure 2.10 TEM and SEM images of (a, c) silica-FePt core-shells nanoparticles and (b, d) silica-core FePt/Au nanoparticles, and (e) particle size distribution of silica-FePt/Au core-shell nanoparticles. Bar is 100 nm.

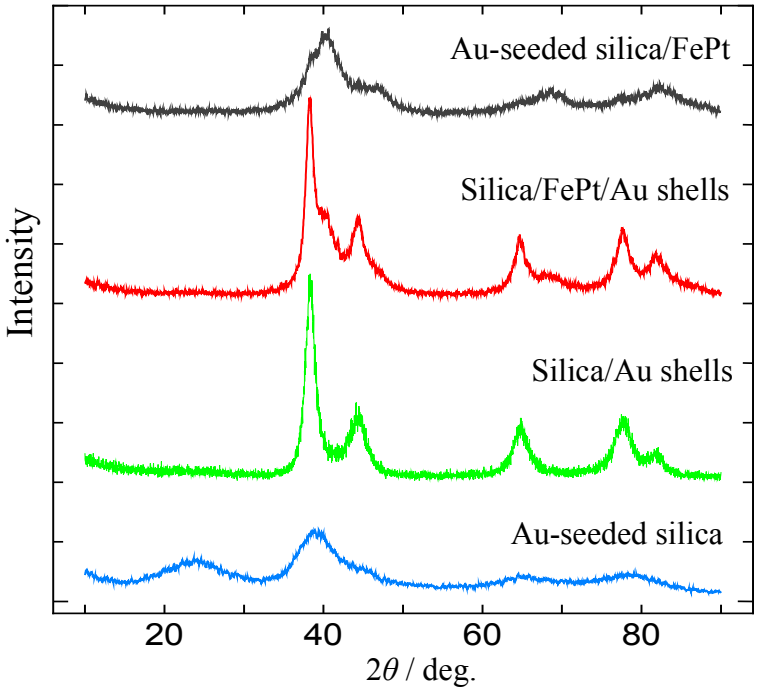

Figure 2.11 Powder XRD patterns of various particles: Au-seeded silica-FePt core-shell nanoparticles in blue, silica-FePt/Au core-shell nanoparticles in red, Au-seeded silica nanoparticles in blue and silica-Au core-shell nanoparticles in green.

Table 2.2 Comparison of Au crystallite diameters of gold nanoshells formed on the FePt nanoshells with formed on the silica cores

Sample Name	Au Crystallite diameter(nm)
Au-seeded silica/FePt NPs	1.7
Silica/FePt/Au nanoshells	5.9
Au-seeded silica NPs	1.2
Silica/Au nanoshells	6.1

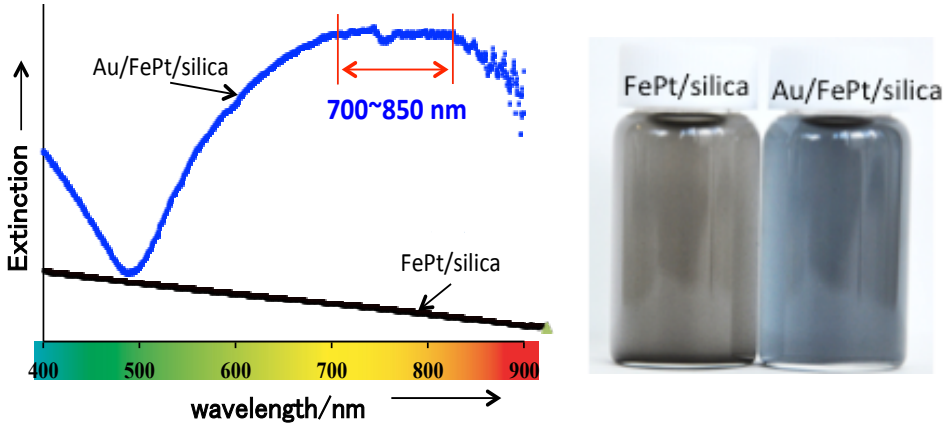

Figure 2.12 UV-Vis spectra and photos of aqueous solutions of silica/FePt shells (in black) and silica/FePt/Au shells (in blue)

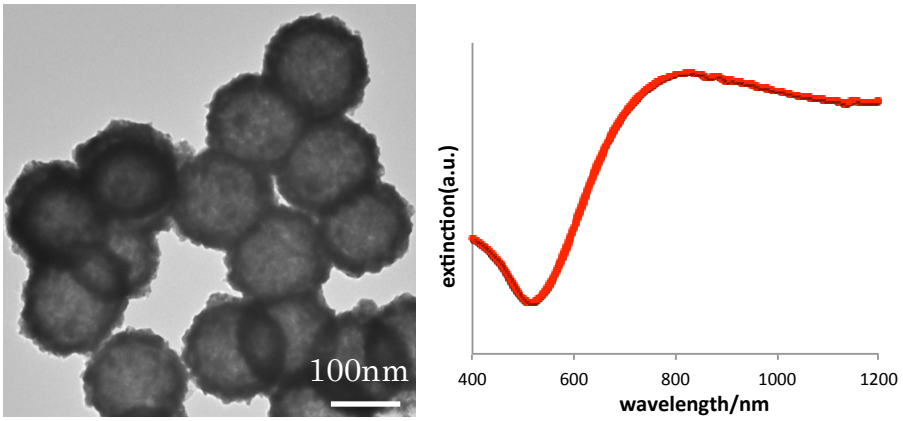

Figure 2.13 TEM images and UV-Vis spectra of 120nm silica/FePt/Au shells.

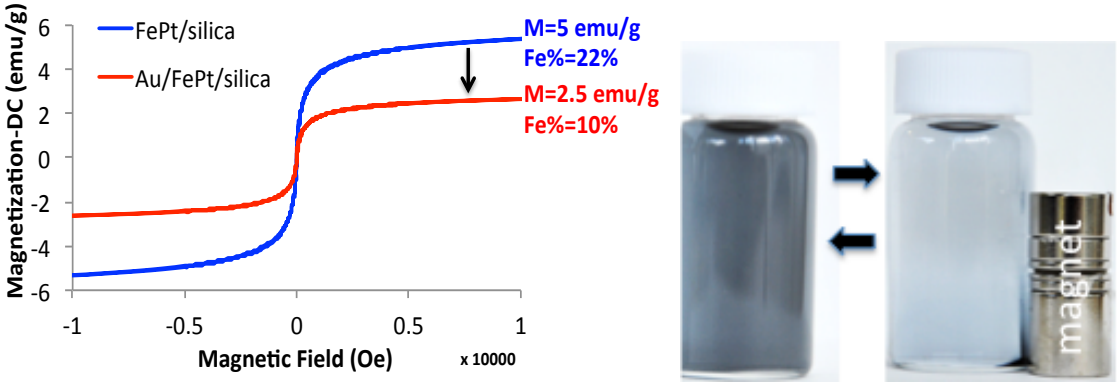

Figure 2.14 MH curves at 300K of silica/FePt nanoparticles in blue and silica/FePt/Au nanoshells in red, and collecting silica/FePt/Au nanoshells using a magnet.

shells allowed us to target them to specific locations of human body by an external magnetic field. This was monitored through the micrographs in Figure 2.14. In the absence of a magnet, the deep-blue suspension of silica/FePt/Au nanoshells is well dispersed. When an external magnetic field is applied, the nanoshells concentrate along the magnet, rendering the dispersion transparent, and they can be redispersed again when the magnet is removed.

2.2.3.1 Dependence on Surface Modification Process Conditions

2.2.3.1.1 Dependence on Polymer Species

Figure 2.15 shows the structures of PEI, PDDA and PVP used in this study. The success in polymer modification and Au seeding on the surface of FePt/silica nanoparticles was clearly identified from the zeta-potential changes shown in Table 2.2. The differences of polymer-modified FePt/silica nanoparticles in the zeta-potential could be caused by the different species of polymers, which indicated the surface charge of polymer-modified FePt/silica nanoparticles depends on the species of polymer. The positively charged cationic polyelectrolyte such as PDDA and PEI could directly adsorb onto the negatively charged surface of FePt/silica particles by electrostatic force. Then the negatively charged THPC-Au colloids were attached on these positively charged surfaces of polymer-modified FePt/silica particles, which resulted that the surface charge of all kinds of particles became negative again.

Figure 2.16 shows TEM images of Au-seeded polymer-modified FePt/silica particles before and after the growth of gold, in which the used polymer is PDDA (a1, a2), PEI

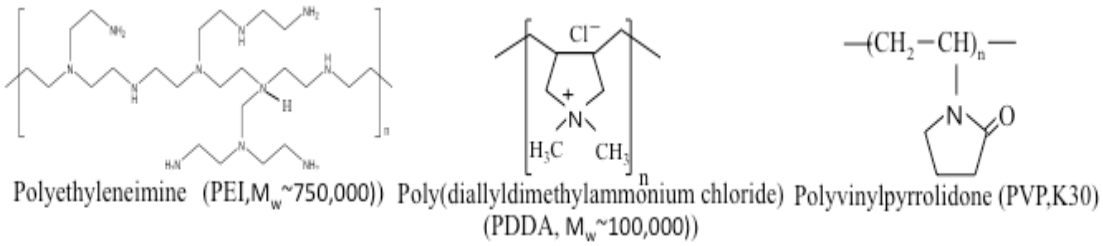

Figure 2.15 Illustrations of the structures of PEI (left), PDDA (middle) and PVP (right)

Table 2.3 Zeta potential changes of FePt/silica nanoparticles modified with the different polymers before and after the attachment of THPC-Au colloids

Material	Zeta-potential (mV) before Au seeding	Zeta-potential (mV) after Au seeding
FePt/Silica NPs	- 40	-
THPC-Au colloids	-48	-
PDDA-FePt/silica NPs	+50	-15
PEI-FePt/silica NPs	+42	-18
PVP-FePt/silica NPs	+0.1	-22

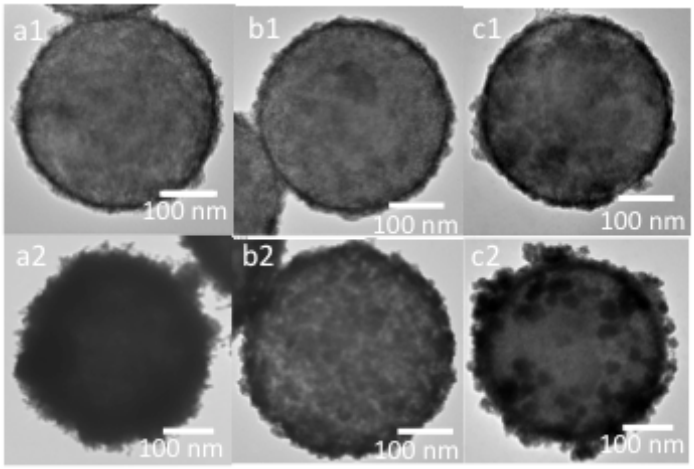

Figure 2.16 TEM images of various Au-seeded silica/FePt NPs before and after the growth of gold, in which the used polymer is PDDA (a1, a2), PEI (b1, b2) and PVP (c1, c2).

(b1, b2) and PVP (c1, c2). The characteristics of these six particles are shown in Table 2.3. As shown in Figure 2.16 (a1, b1 and c1), there are no obvious differences of various Au-seeded FePt/silica nanoparticles in the surface morphology although their polymer interlayers were different. After the growth of gold, the gold shells formed on the surfaces of Au-seeded FePt/silica particles modified using PDDA and PEI while only a lot of large Au clusters formed on the surface of Au-seeded FePt/silica particles modified using PVP. Moreover, the gold layer formed on the surface of PEI-modified FePt/silica particles was more smooth and thinner than that on the surface of PDDA-modified FePt/silica particles. Since the Au growth process conditions for all particles were the same, the difference of Au-shelled polymer/FePt/silica nanoparticles in the surface morphology should be caused by the difference of the Au seeded surfaces, which suggests that the attachment of Au nanoparticles and polymers on the surface of particles was not elicited by electrostatic adsorption because the surface charges of particles modified by PDDA and PEI are similar. Since the polarity of polymer-modified template particles did not decide the morphology of attachment of Au nanoparticles on them, electrostatic interaction was not probably the main reason of the attachment. The functional groups of polymers are probably responsible for the attachment of Au nanoparticles. It is difficult to make clear the difference of surface conditions (surface coverage of Au seeds, location of Au seeds, the number of active sites and so on) between the Au-seeded surfaces modified by PDDA and PEI based on TEM images or surface charges duo to the similar outlook or value. Therefore the Au-seeded surfaces of silica particles were prepared and compared here in order to clarify the difference between the surface modified by PDDA and PEI because it is possible to observe the conditions of Au seeded attached on the surface of silica without FePt NPs based on TEM images.

Figure.2.17 shows the micrographs for Au seed attachment and nanoshell formation v stage and the characteristics of the obtained Au-shelled silica particles are listed in Table 2.4.As well known, PEI exist predominately as positively charged $R–NH_3^+$ groups while PDDA on the other hand has a $[N^+(CH_3)_2]_n$ chain. Zeta potential measurements showed a value of +60~65 mV for PDDA-silica whereas PEI showed a lower value of +40~60 mV. However, the higher level of adsorption of negatively charged Au NPs was not found even with the higher level of positively charged groups of PDDA on the surface of silica in comparison with PEI. When Au ions and the reducing agent were added, the growth of Au NPs on PEI-silica particles was faster than the growth of Au NPs on PDDA-silica particles. After five growth circles, a complete shell of 40nm in thickness formed on PEI-silica while the bare silica surface still could be clearly

Table 2.4 Physiochemical characteristics of various Au-shelled Polymer/FePt/silica NPs prepared in the presence of various Au-seeded Polymer/FePt/silica NPs

Particles	Thickness (nm)	Position of plasmon peak (nm)
Au-shelled PDDA/FePt/silica	40	720
Au-shelled PEI/FePt/silica	24	860
Au-shelled PVP/FePt/silica	-	680

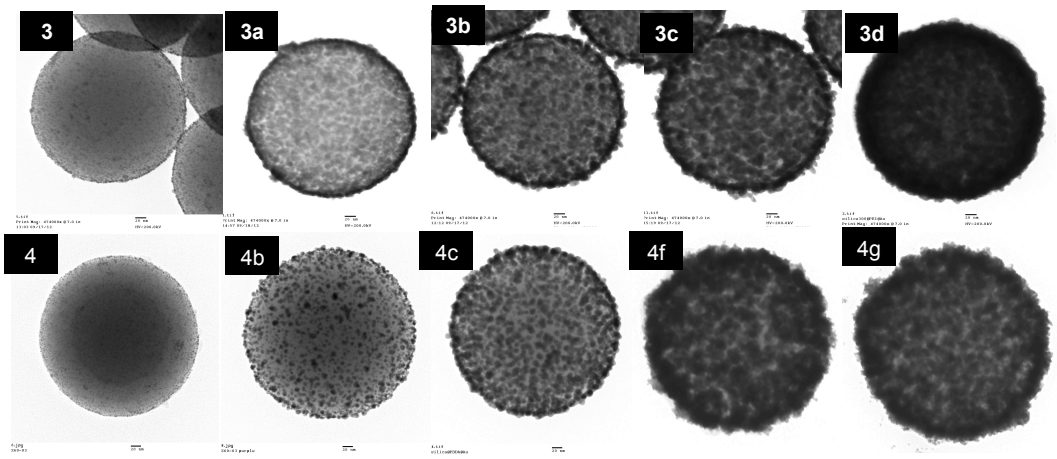

Figure 2.17 TEM images of Au-seeded PEI-modified silica NPs (3) and the growth of Au seeds at various stages (3a, 3b, 3c, 3d), Au-seeded PDDA-modified silica NPs (4) and the growth of Au seeds at various stages (4b, 4c, 4f, 4g),

Table 2.5 Characteristics of Au-shelled Polymer/FePt/silica nanoparticles obtained at various stages of Au growing process

series	Total size/ nm	Shell thickness/nm	SPR Absorption/nm
3a	275	7.5	812
3b	290	15	839
3c	315	27.5	860
3d	339	40	890~
4a	309	9.5	615
4b	328	14	672
4e	366	38	850
4f	389	49.5	780

observed on the shell on PDDA-silica even the thickness increased to 49.5nm after eight growth circles. As a result, the SPR absorption peak wavelength of Au shells on PEI-silica is longer than that on PDDA-silica when the thickness is similar. On the base of their molecular structure, it was thought that PEI could provide more active sites than PDDA so facilitated the subsequent growth of Au shell. Therefore, PEI is more suitable to modify silica than PDDA and PVP when a thin and uniform shell with the SPR absorption in NIR region is desired.

2.2.3.1.2 Effects of Molecular Weight of PEI

The successes of the modification of the PEI polymer to the negatively charged FePt shells were clearly identified from their zeta-potential changes shown in Table 2.6. After amine modification, the surface charge of all samples changed to be positive and their surface charges were similar. Then these PEI-modified particles were utilized in

Table 2.6 zeta-potential changes of various PEI Polymer layers

Name	Components	Before Modification	After Modification	After Au seeding
Sample 1	PEI (Mw:2,000)	-40 mV	42 mV	-0.9 mV
Sample 2	PEI(Mw:25,000)	-40 mV	41 mV	-4.6. mV
Sample 3	PEI(Mw:750,000)	-40 mV	45 mV	-0.5 mV
Sample 4	Mixed PEI(Mw:2,000+25,000)	-40 mV	40 mV	-0.1 mV
Sample 5	Mixed PEI(Mw:2,000+750,000)	-40 mV	44 mV	-3.4 mV
Sample 6	Mixed PEI(Mw:25,000+750,000)	-40 mV	45 mV	-4.5 mV

the following step, with the as-prepared gold colloids of THPC-capped Au NPs together. The obtained THPC-capped Au NPs with a dark brown color have a diameter of ~3 nm and exhibited zeta-potentials in a range from -40 to -50 mV at pH 9, and their crystallite size was 1.1 nm calculated based on the study of XRD.

After Au seed attachment, the negatively charged Au NPs with the diameter of 3~10 nm were attached through electrostatic attraction and weak covalent bonding with the amine groups on the surface of PEI-modified FePt nanoshells. As a result, the surface

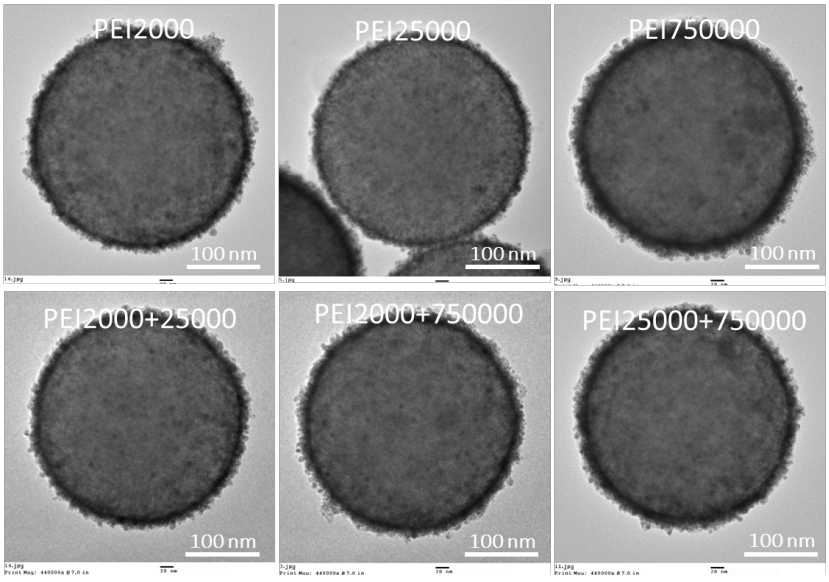

Fig.2.18 TEM images of various Au-seeded silica-FePt core-shell nanoparticles.

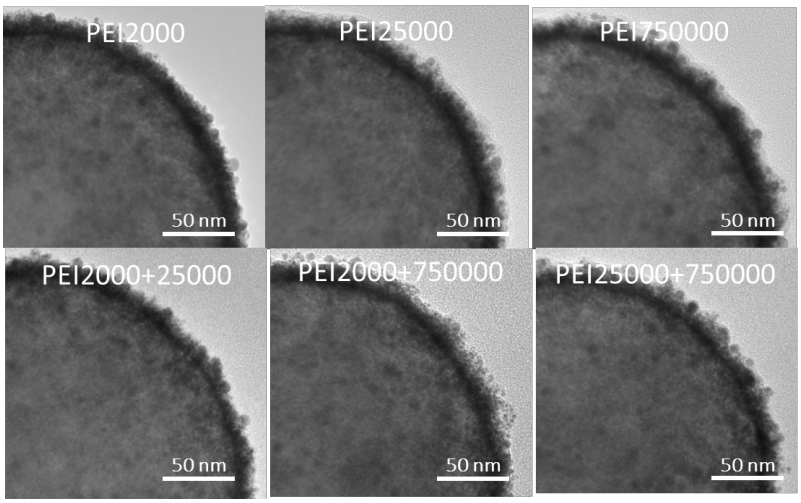

Figure 2.19 High-magnification TEM images of various Au-seeded silica-FePt core-shell nanoparticles.

charges of all Au-seeded FePt shells decreased greatly (shown in Table 2.6). Figure 2.18 compares TEM images of Au-seeded FePt shells. A lot of sphere nanoparticles with the diameter of ~10 nm were observed on the surface of all six kinds of samples, which were thought as the absorbed Au NPs since the size of single FePt NPs was less than 5 nm. And it was also found that the surfaces of Sample 1, 2 and 4 that were modified with low-molecular weight PEI seemed like thinner and smoother than the others samples that were modified with low-molecular weight PEI. Figure 2.19 shows the high magnification TEM images of Au-seeded FePt shells. Unfortunately, it is difficult to compare the quantity of Au NPs absorbed on various polymer layers only based on these TEM images. Figure 2.20 shows the UV-Vis spectrum of Au-seeded FePt nanoshells with various polymer layers, which also confirmed the Au NPs, had been successfully loaded to all of PEI-modified FePt nanoshells. The plasmon peaks of Au NPs were observed at the region of 500~600 nm marked as a pink zone, where there is no SPR absorption for these materials of Fe, Pt, PDDA, and silica but Au. It is also difficult to compare the surface coverage of Au NPs of six samples because these peaks were too weak and broad. XRD studies are shown in Fig. 2.21. Four diffraction peaks at $2\theta = 41.14°, 47.18°$ and $83.54°$were observed in the XRD patterns of various Au-seeded FePt nanoshells, which can be identified as the diffraction of the FePt fcc phase. No obvious diffraction peaks of the Au phase at $2\theta = 38.28°, 44.48°, 64.74°, 77.76°$ and $81.94°$ were observed in the XRD patterns since the amount of the Au NPs were too small and their diffraction peaks were too weak to be recognized.

In order to form the gold shell, Au-seeded silica/FePt core-shell nanoparticles was further reduced via electroless plating process. The Au NPs absorbed on various polymer layers were grew by the reduction of $HAuCl_4$ in K-gold solution with formaldehyde. The addition of K-gold solution and formaldehyde was being divided into three times. The growth of the Au NPs was monitored through TEM images, XRD patterns and UV-Vis-NIR spectra. The results after the first growth were discussed in this chapter.

Figure 2.22 shows TEM images of various Au-seeded FePt nanoshells after the first growth. The surface coverage of Au clusters increased obviously. For sample 3, 5 and 6,the Au NPs began to coalesce. These changes can be monitored by UV-Vis spectroscopy. As shown in Fig. 2.23 when Au is reduced exclusively onto Au seeds in the initial stage, the SPR peak of Sample 1 (PEI 2000) and 2 (PEI 25000) shifted to 600 nm from 550 nm, which reflects the characteristics of the growing Au seeds. And the

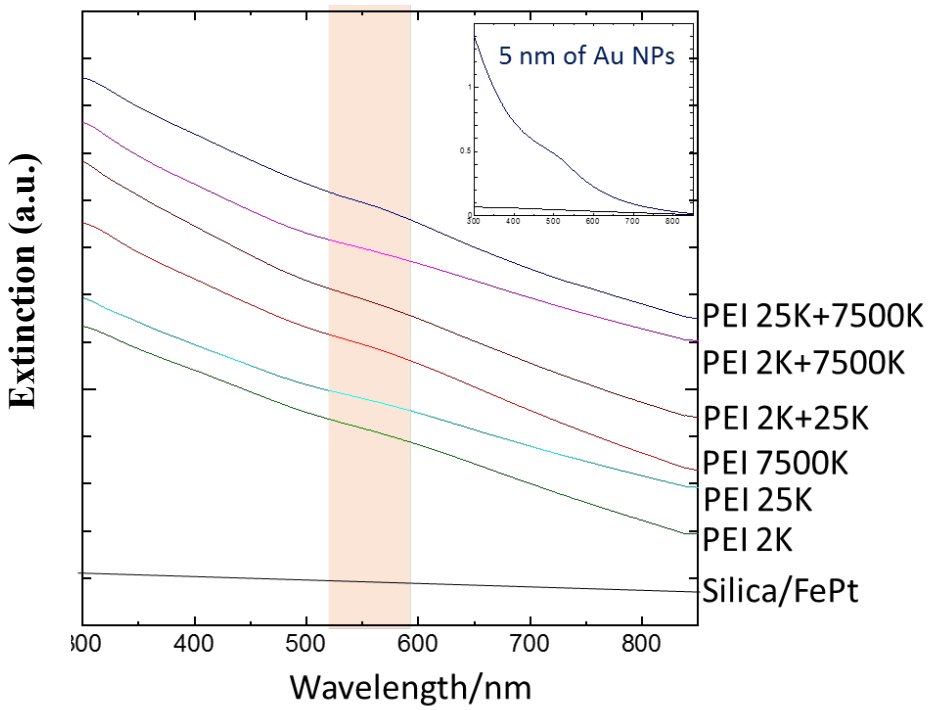

Figure 2.20 UV-Vis-NIR spectra of various Au-seeded silica-FePt core-shell nanoparticles with different polymer interlayers.

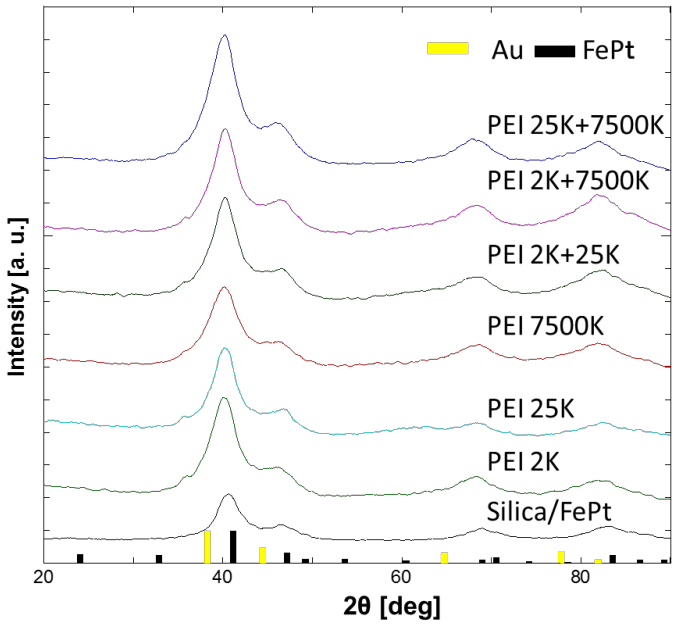

Figure 2.21 Powder XRD patterns of various Au-seeded silica-FePt core-shell nanoparticles with different polymer interlayers.

intensity of their SPR peaks in the region of 500~650 nm was still stronger than that in the region of 700~1200 nm, which reflects the characteristics of the coalesced Au clusters or continuous Au nanoshells. So it was thought that the Au NPs absorbed on the surface of Sample 1 and 2 grew but the distance of these Au NPs was still too far to form coalescence.

On the contrary, a weak shoulder peaks at 700–900 nm appeared in the spectra of Sample 3~6, which was attributed to the presence of Au islands on the surface. So it was guessed that the surface coverage of Sample 3~6 were higher than those of Sample 1 and 2. Among sample 3~6,the SPR peak of sample 5 modified by the mixture of PEI with the lowest molecule weight of 2K and PEI with the highest molecule weight of 750K appeared around 912 nm, which is the longest wavelength among all various samples. Moreover the obtained gold shell of 14 nm in thickness also is thinnest. The XRD study exhibited consistent tendencies. As revealed in Figure 2.24, three obvious shoulder diffraction peaks of the Au phase at 2θ = 38.28°, 44.48° and 81.94° appeared near to the diffraction peaks of the FePt and two independent diffraction peaks of the Au phase at 2θ = 64.74°, 77.76° were observed in the XRD patterns of Sample 2~6, while the XRD patterns of Sample 1 was similar with FePt nanoshells and all the diffraction peaks of the Au phase were very weak.

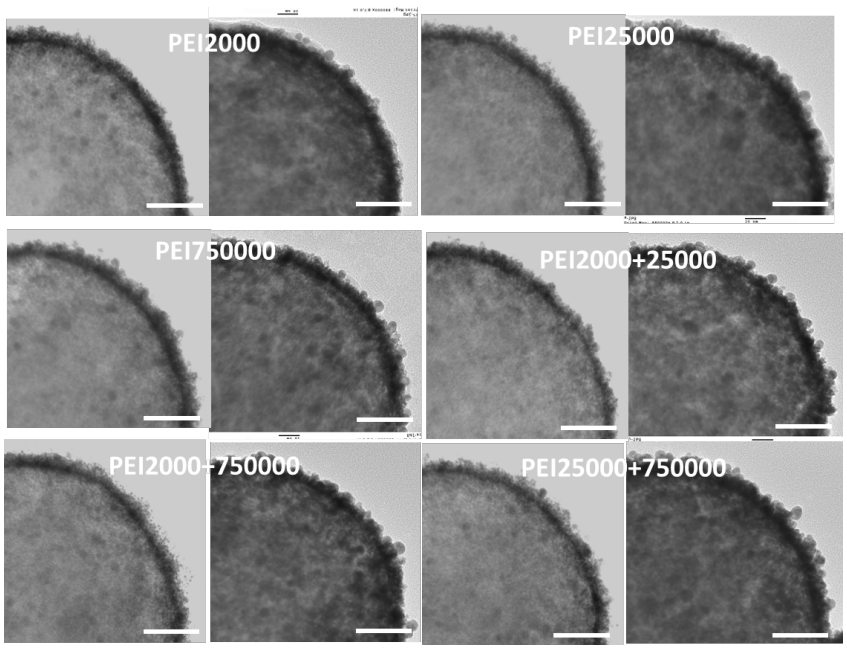

Figure 2.22 Comparison of various Au-seeded silica-FePt core-shell nanoparticles before and after the first growth of gold shell

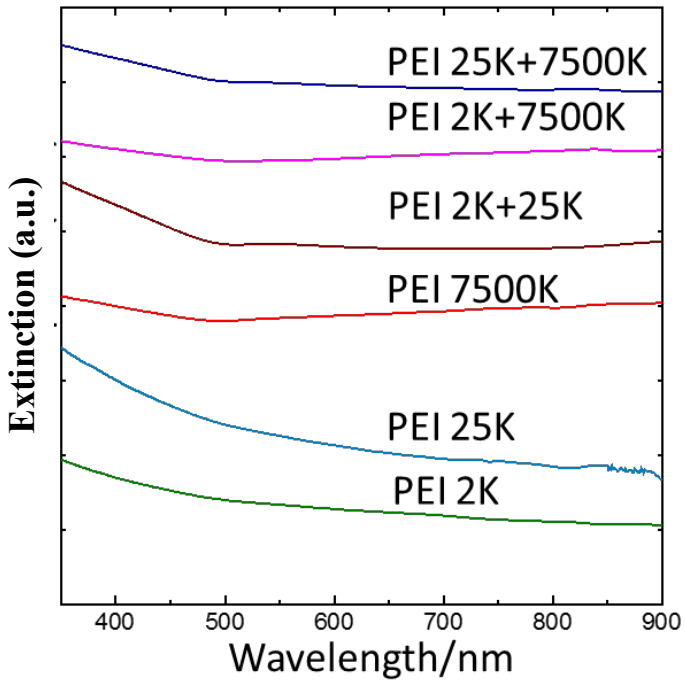

Figure 2.23 UV-Vis-NIR spectra of various Au-seeded silica-FePt core-shell nanoparticles with different polymer interlayers after the first growth of gold shell.

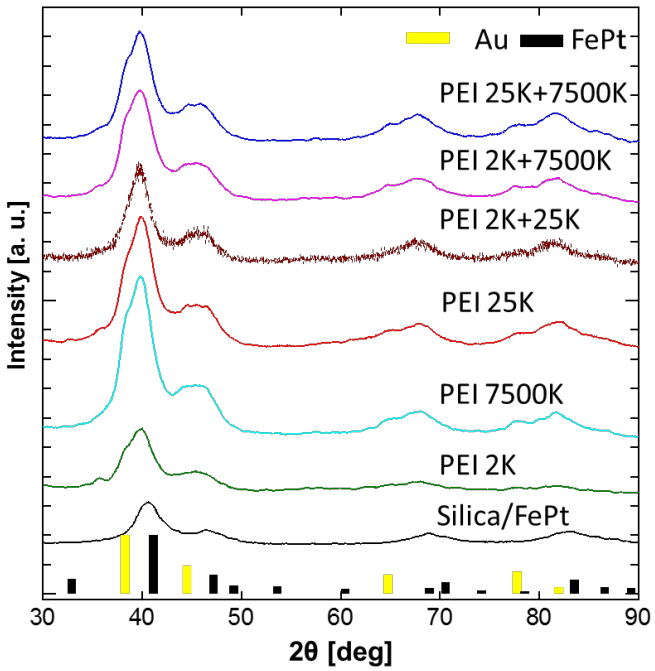

Figure 2.24 Powder XRD patterns of various Au-seeded silica-FePt core-shell nanoparticles with different polymer interlayers after the first growth of gold shell.

The effect of the molecular weight of PEI during the process of modifying the surface of FePt nanoshells on the quality and the optical property of gold nanoshells was investigated and discussed in this section. The SPR peak of gold shell grown on the FePt nanoshell modified by the mixture of PEI with the lowest molecule weight of 2K and PEI with the highest molecule weight of 750K appeared around 912 nm, which is the longest wavelength among all various samples. Moreover the obtained gold shell of 14 nm in thickness also is thinnest. The above results demonstrates that using the mixture of PEI with low Mw and PEI with high Mw is a potential method for improving the quality of gold nanoshells and optimizing the optical property of gold nanoshells.

2.2.3.2 Dependence of Au Seeding Process Conditions

2.2.3.2.1 Size Effects of Gold Colloids

In present thesis, THPC-capped Au NPs (THPC-Au) and PVP-capped Au NPs (PVP-Au), two types of gold colloids with the different particle size and surface property as shown in Figure 2.25 (a, b), were used in the preparation of the Au-seeded silica/FePt core-shell nanoparticles. Table 2.7 shows the details of physiochemical characteristics of the gold colloids as well as their attached particles. As seen in Table 2.7, the changes on the zeta-potentials of Au seeded PEI/FePt/silica indicated the successful attachment of THPC-Au and PVP-Au. THPC-Au and PVP-Au can be attached to the surface of aminated templates by the electrostatic force or van der Waals force. The higher surface charge of PVP-Au seeded PEI/FePt/silica might be caused by the relatively higher surface charge of PVP-Au. Here, it is very difficult to observe the condition of the Au colloids attached on the surface of FePt shell based on their TEM images shown in Figure 2.25 (c, d) due to the similar particle size of Au NPs with FePt NPs, therefore 120 nm silica particles modified by APTES without FePt shell were also attached using these two kinds of Au colloids. As shown in Figure 2.25 (e, f), the monodisperse deposition of THPC-Au seeds while the heterogeneous deposition of PVP-Au seeds are observed. And it is easy to observe the difference in the particle size between two kinds of Au colloid, however, difficult for the difference in the amount of the attached Au seeds. Au seeded PEI/FePt/silica prepared with the different gold colloids exhibited the different absorption peaks of UV-Vis spectra as shown in Figure 2.26. THPC-Au seeded PEI/FePt/silica exhibited the very slight absorption peak at ca.510 nm while PVP-Au seeded PEI/FePt/silica exhibited a distinct spectral intensity of plasmon bands at ca.530 nm. The difference of the plasmon absorption bands among Au-seeded PEI/FePt/silica reflected the size of gold clusters that is strongly dependent on the peak intensity and red-shift of absorption bands. The Au seeded PEI/FePt/silica

were further reduced by reaction with gold salts (K-gold) in the presence of formaldehyde. The attached Au seeds onto the silica cores played as nucleation sites to induce the coalescence between neighboring gold clusters [33]. To assess the Au seed effect of final shell growth, the volume radio of Au seed-attached particles to the K-gold solution was fixed, and the amount of formaldehyde (reducing agent) was kept at constant. The monodisperse deposition of THPC-Au seeds resulted in the smooth and thin gold nanoshells of 17 nm in thickness, as shown in Figure 2.27 (a). On the other hand, the heterogeneous deposition of PVP-Au seeds resulted in the relatively rough and thick gold nanoshells of 40 nm in thickness as shown in Figure 2.27 (b). This suggests that the smaller Au seeds lead to a better surface coverage of the PEI-modified FePt shells, and to the subsequent growth of nanoshells of better quality (i.e. thin and uniform shell). As shown in Figure 2.28, gold nanoshells prepared by THPC-Au colloids exhibited the red-shift plasmon resonance (770nm) in comparison to those (680 nm) prepared by PVP-Au colloids. That is, more uniform gold nucleates prepared by THPC-Au led to smooth and continuous gold layer onto the PEI/FePt/silica cores via a

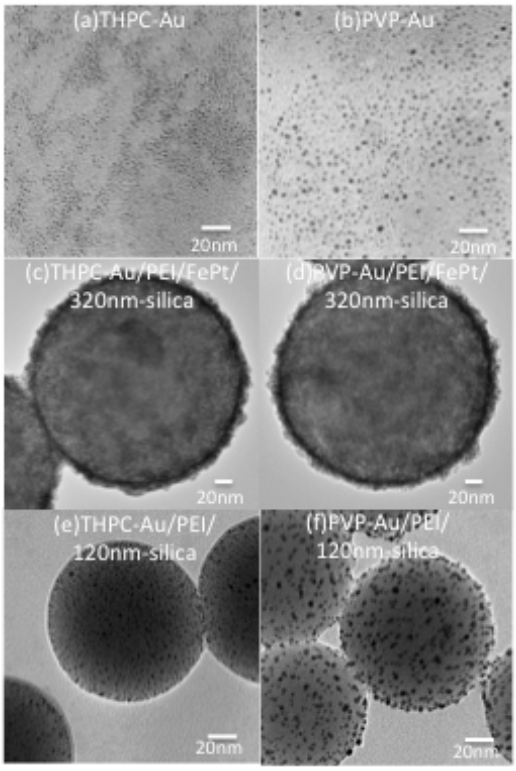

Figure 2.25 TEM images of Au colloids different in particle size and surface property (a, b), the prepared Au seeded PEI/FePt/320nm-silica (c, d) and Au seeded PEI/120nms-ilica (e, f), relatively.

Table 2.7 Physiochemical characteristics of various gold colloids and Au-seeded silica/FePt core-shell nanoparticles

Characteristics	THPC-Au	PVP-Au
Particle size (nm)	~3	~8
Zeta-potential of gold colloids (mV)	-30~-40	-1~1
Zeta-potential of PEI/FePt/silica (mV)	40~50	40~50
Zeta-potential of Au seeded PEI/FePt/silica (mV)	-30~-40	0~5
Position of plasmon peak of Au seeded PEI/FePt/silica (nm)	510	530

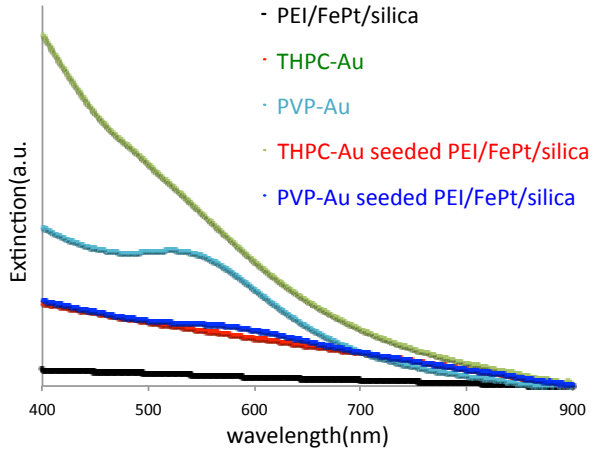

Figure 2.26 UV-Vis spectra of Au seeded PEI/FePt/silica NPs prepared with the different gold colloids.

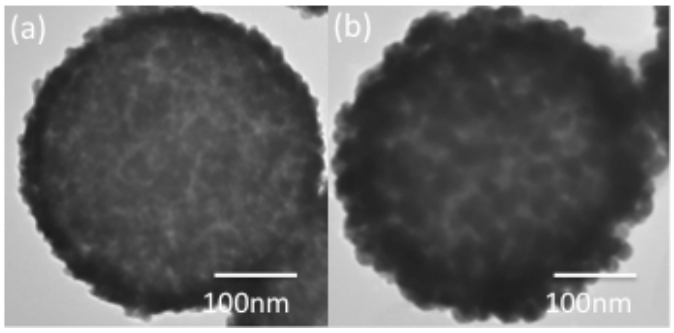

Figure 2.27 TEM images of Au shelled PEI/FePt/320nm-silica NPs using (a) THPC-Au and (b) PVP-Au

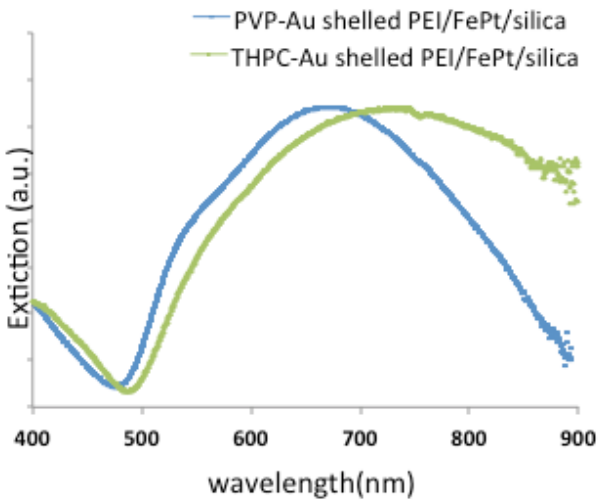

Figure 2.28 UV-Vis spectra of Au shelled PEI/FePt/silica NPs

nucleate-mediated coalescing process, consequently leading to the more red-shift plasmon resonance of gold shell. The difference of active surface area of Au seeds attached on the surface of FePt shell, wherein gold clusters more easily form also is considered as the reason for the differences in the two gold shells. The active surface area of gold clusters on PVP-Au-deposited cores should be fewer than that of THPC-Au-deposited cores as the surface area of PVP-Au NPs was coated by PVP. Hence, THPC-Au gold colloids were used in the following experiments to determine the growth process of the gold layers over PEI-modified FePt shells.

2.2.3.2.2 Aging Effects of Gold Colloids

2.2.3.2.2.1 THPC-Au

In the synthesis process of THPC-Au, THPC plays the role of both the reducing agent and the stabilizing agent. THPC reduced the gold ions by the formation of formaldehyde and then absorbed to the surface of gold NPs to provide colloidal stability by its negative charges. The equally charged gold nanoparticles repel each other resulting in the colloidal stability.

$$[P(CH_2OH)_4]Cl + NaOH \rightarrow P(CH_2OH)_3 + H_2O + H_2C{=}O + NaCl \quad (1)$$

$$P(CH_2OH)_3 + 2H_2O \rightarrow O_2P(CH_2OH)_3 + 2H_2 \quad (2)$$

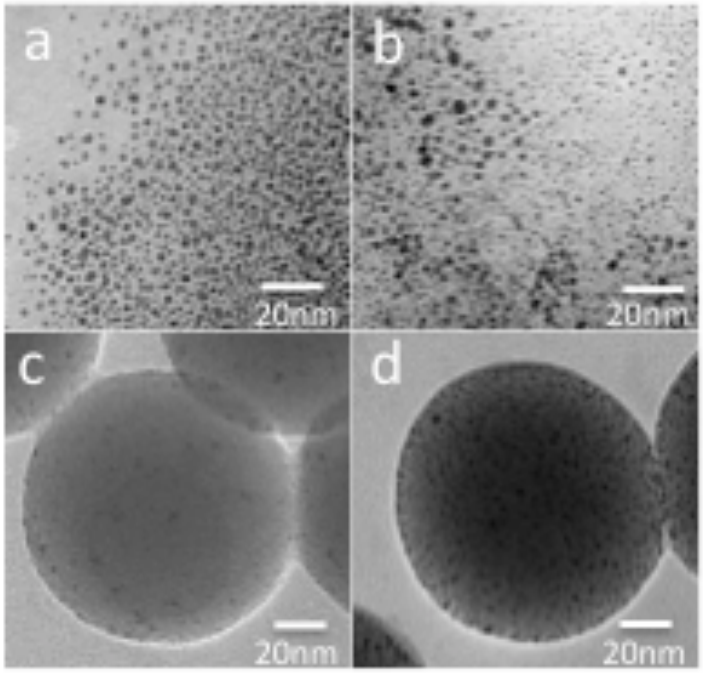

Figure 2.29 TEM images of THPC-Au (a) freshly and (b) two-week-aged, and Au-APTES/SiO_2 NPs prepared using (c) freshly and (d) two-week-aged THPC-Au.

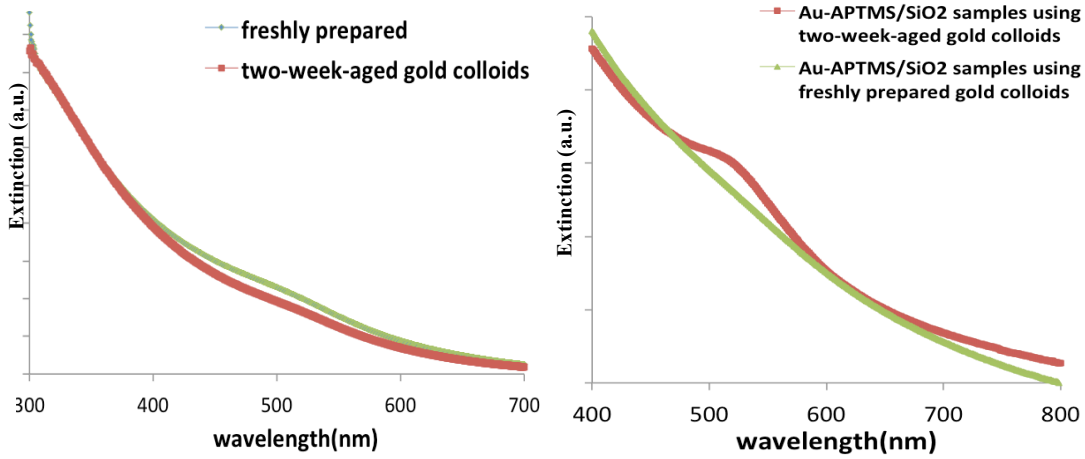

Figure 2.30 UV-Vis spectra of THPC-Au with various aging time at 4°C and Au-APTES/SiO_2 NPs prepared respectively

The resulting dark brown sol contained THPC-Au nanoparticles of ~3nm with a net negative interfacial charge of -40~-50mV at pH 10~11 determined by TEM images shown in Figure 2.29 (a). The UV-Vis spectra of gold colloids before and after aging were showed in Figure 2.23. The absorption peak red-shifts slightly after aging, indicating a slight variation of colloidal stability and particle size. This similar variation was observed from TEM images of gold colloids before and after aging. The

larger-sized gold nanoparticle of ~4 nm were observed from Figure 2.29 (b). At the same time, the pH of two-week-aged gold colloids gradually decreased to pH 7~8 from an initial pH 10~11, possibly because the residual OH-ions were gradually consumed by THPC reducing agents to form tris (hydroxymethyl) phosphine during the aging period at 4°C.The aggregation or Ostwald ripening, where larger particles grow at the expense of smaller ones, may lead to a change of the size of colloids. The zeta-potential of THPC-Au also increased to -30~-40mV at pH 7~8.

Two types of THPC-Au colloids (i.e., freshly prepared and two-week-aged) were used to attach APTES-modified silica nanoparticles of 120 nm in diameter. The attachment of THPC-Au colloids was achieved through electrostatic attraction between the aminated silica particles and the gold colloids having negative charges.

Figure 2.29 (c, d) compares TEM images of the Au-APTES/SiO_2 samples prepared using the freshly prepared and the aged THPC-Au colloids. The aged gold colloids exhibited higher surface coverage on the silica nanoparticle surfaces. In contrast, the Au-APTES/ SiO_2 sample prepared using the freshly prepared gold colloids exhibited a relatively lower surface coverage. As shown in Figure 2.30 (right), the peaks in the plasmon-derived absorption spectra were positioned around 500 and 520 nm, respectively, for the freshly prepared and aged gold colloids. The stronger plasmon resonance of the latter should be caused by the larger-sized gold clusters and higher surface coverage. The difference of two types of colloids in surface coverage would be caused by changes in the surface chemistry and zeta potential of gold colloids, which will be especially sensitive to pH as protonation/deprotonation affects. In Addition, the terminal amine groups of modified silica cores exist predominantly as positively charged R-NH^{3+} groups at pH＜10, pH in which seeding process is carried out. Therefore, two-week-aged gold colloids were used in the following experiments to determine the growth process of the gold layers.

2.2.3.2.2.2 PVP-Au

In the synthesis process of PVP-Au, $NaBH_4$ reduces gold ions through the formation of hydrogen to produce gold nanoparticles while PVP stabilized the gold nanoparticles by embedding particles in a shell of stabilizing molecules as the capping agent.

The reduction of chloroauric acid with $NaBH_4$ results in relatively bigger gold nanoparticles, ~5 nm in diameter determined by TEM image showed as Figure 2.31 (a), with middle interfacial charge of -1~1mV at pH 7~8. It is thought that there was no variation of particle size with various aging times by comparing TEM images of the

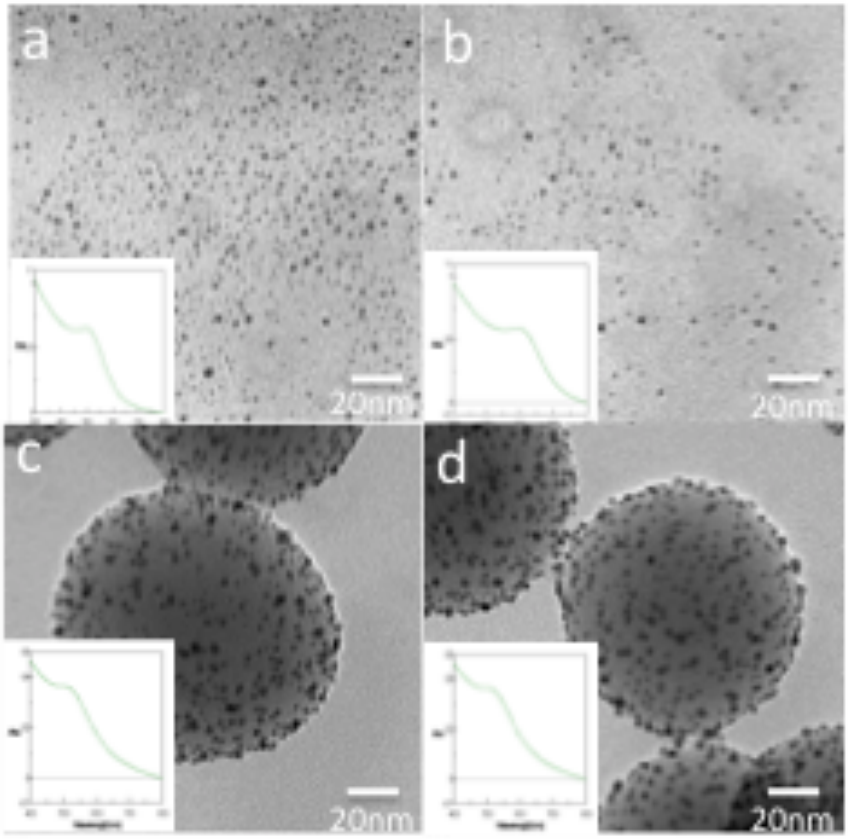

Figure 2.31 TEM images and UV-Vis spectra of PVP-Au and their Au-seeded APTES/SiO_2 (a,c) freshly prepared, (b,d) two-week-aged, the bar is 20nm.

aged colloids (Figure 2.31 (b)) with TEM images of the fresh colloids (Figure 2.31 (a)). As shown in Figure 2.31, UV-Vis spectra of two gold colloids were similar, in accordance with the conclusion resulted from TEM images. The pH of the aged colloids was 7~8, the same as that of the fresh colloids. This result clearly justifies that the PVP as the capping agent can significantly enhance the colloidal stability. It is believed that PVP couples to amino functionalized gold colloids while amide within pyrollidone structure gives water-soluble properties. It can be estimated that a larger surface area of the gold nanoparticles was covered by PVP molecule. Even stocked at room temperature, the PVP-Au colloids still showed a good stability.

TEM images and UV-Vis spectrum of Au-APTES/SiO_2 samples prepared using fresh prepared and aged PVP-Au were shown in Figure 2.31 (c,d). The peak position was similar. Here we realized that the interaction of PVP-Au NPs with silica cores is dependent on van der Waals forces rather than on electrostatic force.

2.2.3.3 Dependence of Au Growth Process Conditions

2.2.3.3.1 Amount Dependence of Gold Reducible Salts

The Au seeds attached to the PEI-modified FePt nanoshells were further reduced by reacting with gold-reducible salts, consequently leading to continuous gold layers on the core surface via coalescing of neighboring gold clusters. The iterative growth of the Au shell was monitored through TEM images (Figure 2.32) while K-gold solution including gold reducible salts was being added. After the first growth, when the average thickness of the Au shell was 7.5 nm, the Au seeds were visibly larger and began to coalesce, as shown in Figure 2.32 a1–a3, whereas after the second growth, the initial seeds merged and became almost indistinguishable (Figure 2.32 b1–b3). An incomplete Au shell with an average thickness of 15 nm was formed. After the third growth (Figure 2.32 c1–c3), a complete and thick Au shell with an average thickness of 40 nm was observed. The XRD patterns at various stages of growth of the Au shells exhibited consistent tendencies. As revealed in Figure 2.33, the diffraction peaks of Au sharpened, and the size of crystallites gradually increased from 2.1 to 4.3 nm and finally to 5.9 nm.

The evolution of the nanoshell structure gives rise to a gradual change in the optical properties of these colloids. This change can be monitored by UV-Vis spectroscopy. As shown in Figure 2.34, when Au is reduced exclusively onto Au seeds in the initial stage, a well-defined SPR peak appears at 550 nm, which reflects the characteristics of the growing Au seeds. The weak shoulder peak at 650–750 nm simultaneously appeared in the spectrum, which was attributed to the presence of Au islands on the surface, which indicates that an optical signature for the Au shell had developed. After the second Au deposition, the left peak became relatively weak whereas the right peak became strong and shifted slightly to the longer wavelengths of 700–800 nm. A thin and porous Au shell was observed. When the Au nanoshell reached completion in the last stage after the third deposition of Au, the shoulder peak to the right of the spectra further shifted to 750–850 nm. There were two distinguishable features in the shell growth process, i.e., the increase in nanoparticle size, and the decrease in separation between two neighboring Au NPs. With the growth of Au NPs along the surface, the left SPR peaks for Au NPs are enhanced and red-shifted, which can be determined by both the change in shape and size. At the same time, the separation between neighboring Au NPs decreases with the progressive seeded growth, leading to a gradual increase in dipole coupling, which has been shown to be responsible for shifting and broadening the right SPR peaks for Au shells.

The TEM images and UV-Vis spectroscopy results proved that the morphology and optical properties of Au shells could be tuned by controlling the growth process. The ability to control the morphology and thickness of magnetic Au shells is very important when considering some applications where a complete Au shell with strong SPR absorption in the NIR region is required, such as that in photothermal therapy. Other applications require an incomplete shell such as that in catalysis, biosensing, drug delivery, and SERS where exposed Au NPs on the surface are needed.

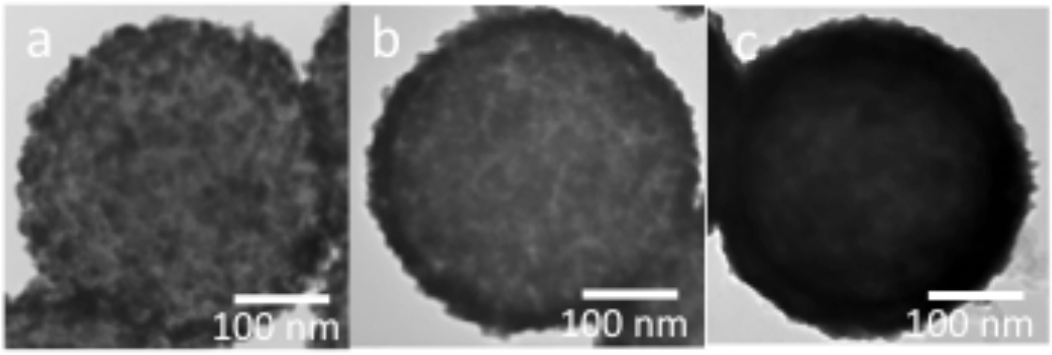

Figure 2.32 TEM images of Au-shelled PEI/FePt/silica with different thicknesses of a: 7.5 nm, b: 15 nm, and c: 40 nm. Bar is 100 nm.

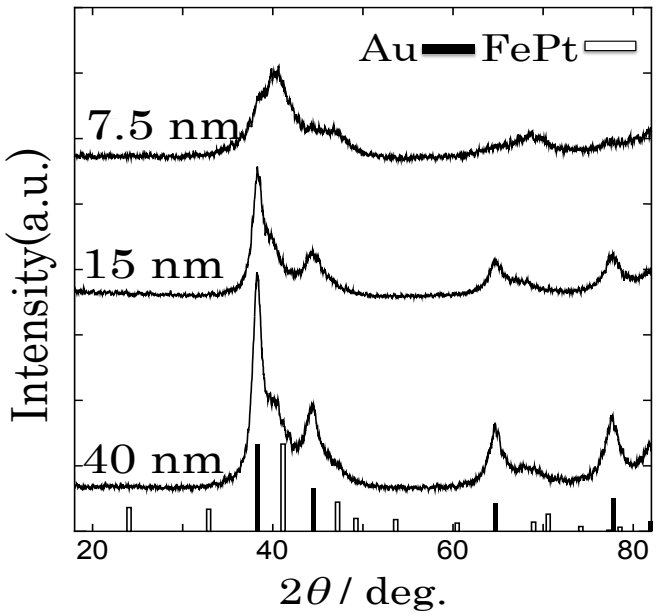

Figure 2.33 Powder XRD patterns of Au-shelled PEI/FePt/silica with different thicknesses Au shells.

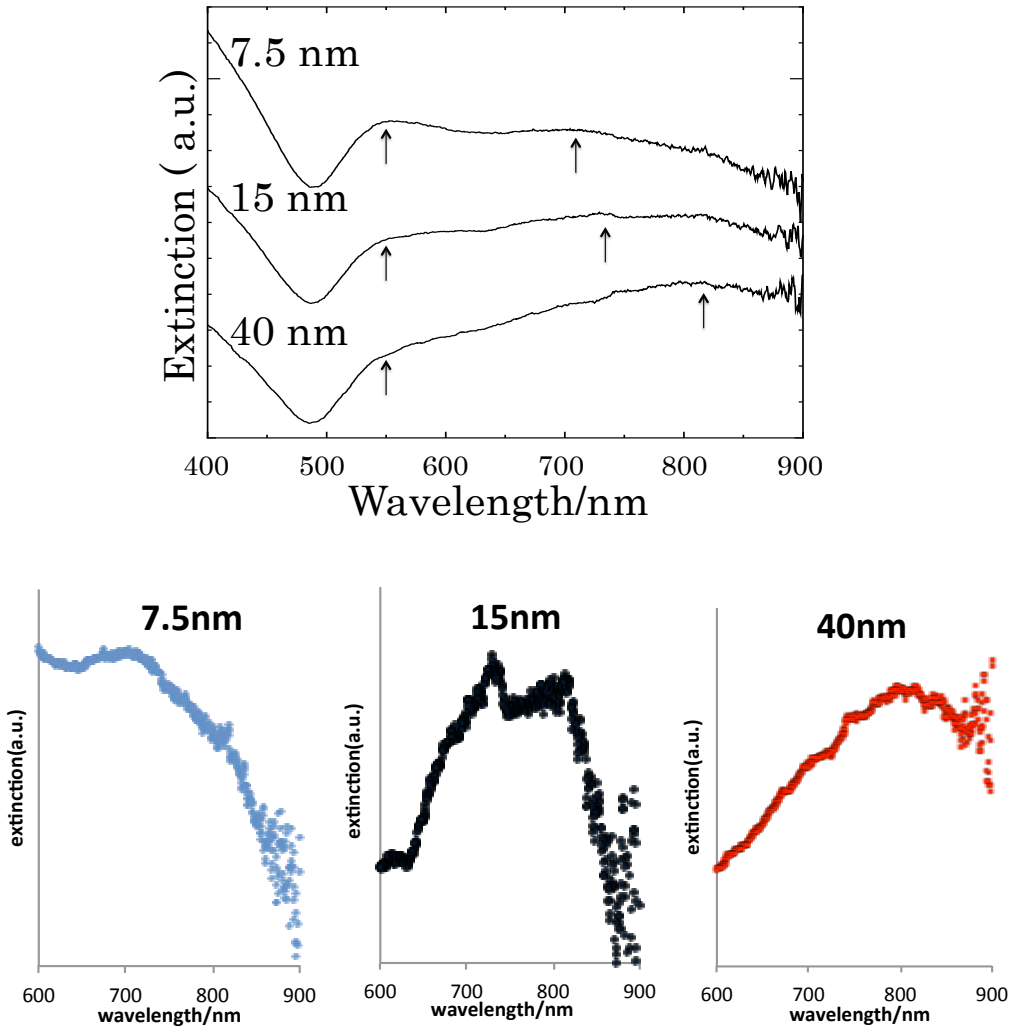

Figure 2.34 Gradual change in optical properties of Au-shelled PEI/FePt/silica with increased thickness of Au shells.

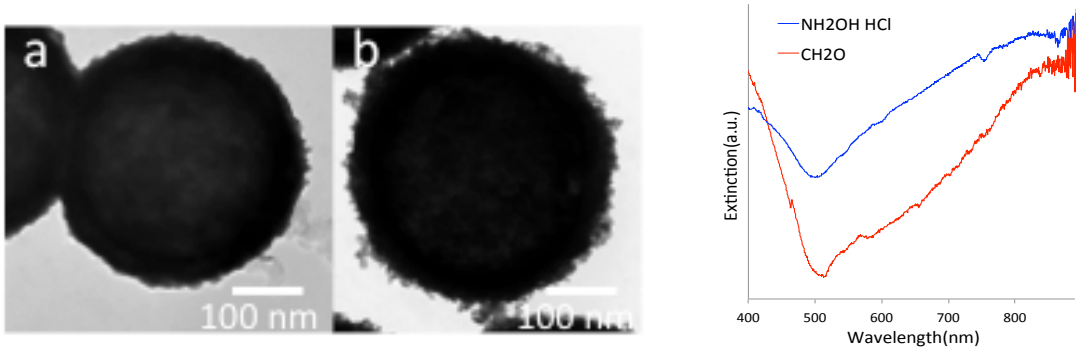

Figure 2.35 TEM images and UV-Vis spectra of Au-shelled PEI/FePt/silica prepared by (a) formaldehyde and (b) hydroxylamine-hydrochloride, the bar is 100nm.

2.2.3.3.2 Dependence of Gold Reducing Agents

The synthesis of gold nanoparticles in aqueous phase can be obtained by the reduction of tetrachloroauric acid ($HAuCl_4$) in the presence of a reducing agent. A lot of reducing agents have been reported for the synthesis of silica-core gold nanoshells and it was found that these reducing agents greatly affected the quality and quantity of the final products of gold shells [34]. For the growth of gold nanoshell, the morphology (such as thickness, roughness and coverage) of gold shell greatly depends on the reducing agent [35]. In this thesis, two most used reducing agents of formaldehyde (H_2CO) and hydroxylamine-hydrochloride ($NH_2OH\,HCl$) were chose and utilized as the reducing agent for the growth of a gold layer on a aminated surface of FePt nanoshells. Their Eq. are shown as below:

$$3CH_2O + 2[AuCl_x(OH)_{4-x}]^- = 3HCOOH + 2Au^0 + 2xCl^- + 3H_2O + (2-2x)OH^-$$

$$6NH_2OH{\cdot}HCl + 2[AuCl_x(OH)_{4-x}]^- = 3N_2 + 2Au^0 + (2x+6)Cl^- + 12H_2O + 2(1-x)OH^-$$

Figure 2.35 shows TEM images and UV-Vis spectra of Au-shelled PEI/FePt/silica particles, which were prepared by using formaldehyde or hydroxylamine-hydrochloride as the reducing agent while other conditions were the same. The gold layer prepared by the strong reducing agent of hydroxylamine-hydrochloride, having a thickness of 32.9 nm, is more rough and thicker than the gold layer prepared by the mild reducing agent of formaldehyde, whose thickness is 22 nm. It is believed that the difference of the reducing ability between these two reducing agents resulted in the difference of gold layers in morphology. The growth of gold layer with the presence of hydroxylamine-hydrochloride was fast so that a rough and thick gold layer formed.

As shown in Figure 2.35 (right), the SPR absorption peak of Au-shelled PEI/FePt/ silica particles prepared using formaldehyde showed at around 860 nm is more red-shift than Au-shelled PEI/FePt/silica particles prepared using hydroxylamine-hydrochloride that showed at around 830 nm. It is thought that the differences in the surface morphology and thickness caused the difference in the optical property. Considering that a gold shell with SPR absorption in the region of NIR and the ease of controlling the shell thickness are desirable in this thesis, the mild reducing agent of formaldehyde was chose for the following synthesis.

2.3 Conclusions

In this chapter, a series of silica-core FePt nanoshells with different particle size and shell thickness were prepared under various fabrication conditions; gold nanoshells

were successfully grown on the surface of FePt nanoshells via the two-step seed-mediated growth method using PEI polymer layer as the interlayer between FePt nanoshell and gold nanoshell. The study of TEM images and SEM images of the silica-FePt/Au core-shell nanoparticles and the appearance of an obvious SPR peak in the region of NIR wavelength demonstrated the formation of a complete gold shell and the two-layered structure of the silica-FePt/Au core-shell nanoparticles.

And we have studied the effects of various fabrication conditions on the quality of gold shells (such as the polymer species and molecular weight of polymer interlayer, the particle size and surface charges of gold colloids, the Au ion amount and the reducing agent), and optimized these fabrication conditions. The results show that there are significant improvements in the quality of the gold shells that is grown on the FePt nanoshells. In this study, six types of different PEI layers were prepared on the FePt nanoshells under various conditions (polymer species and molecular weight) and the quality of the obtained gold shell was studied using zeta-potential measurement, TEM, SEM, XRD and UV-Vis spectra. The results show that both of the polymer species and molecular weight of polymer have a significant influence on the formation of gold shells and similar with silica-core gold nanoshell, the amine group of PEI polymer is a relatively appropriated primer to enhancing coupling the gold shell with the FePt shell. Furthermore, the optimal condition for preparing an interlayer on the surface of FePt nanoshell is using the mixture of PEI (Mw: 2K) and PEI (Mw: 750K) with the weight ratio of 1:4 and the concentration of 3%. The obtained silica/FePt/Au nanoparticles have a smooth and thin gold shell of 14 nm in thickness, and show a SPR peak with the longest wavelength of 912 nm. As a result of my investigation, it is concluded that using the mixture of PEI polymers with different molecular weight to modify the FePt nanoshell make it possible to form a high quality gold shell. The use of the negatively charged THPC-Au colloids with a small size of ~3 nm and the reducing agent of formaldehyde is also responsible for the growth of a uniform and thin gold shell. The negatively charged small THPC-Au colloids can uniformly attach the surface of PEI-modified silica/FePt nanoparticles with a relatively higher surface coverage. And the use of the mild reducing agent of formaldehyde allow the reaction well controlled to avoid the overgrowth of gold clusters that may leads to the formation of a thick shell. Additionally, the total particle size of silica/FePt/Au nanoparticles can be tuned by using silica/FePt cores with different size and controlling the thickness of each shell by changing the amount of metal nanoparticles at the each synthesis process.

On the whole, the studies discussed above indicate the importance of the polymer

species and molecular weight of functional polymer in the fabrication process of interlayer and gold outer-layer. The insight provided in this study may aid in the development of techniques that can produce a smooth and complete polymer layer that could be used as the interlayer in the fabrication of other two-layered metal nanoshells.

Reference

[1]. Fuchigami T, Kawamura R, Kitamoto Y, Nakagawa M, Namiki Y. Langmuir 2011; 27:2923-8;
[2]. Fuchigami T, Kawamura R, Kitamoto Y, Nakagawa M, Namiki Y. Biomaterials 2012; 33:1682-7;
[3]. Namiki Y, Fuchigami T, Tada N, Kawamura R, Matsunuma S, Kitamoto Y, et al. Acc Chem Res 2011; 44:1080-93;
[4]. Oldenburg, S.J.; Averitt, R.D.; Westcott, S.L.; Halas, N.J. Chem. Phys. Lett. 1998, 288, 243–247.
[5]. Anderson RR, Parrish JA.1981 The Optics of Human-Skin. J. Invest. Dermatol. **77**, 13–19.
[6]. Sperling RA, Rivera Gil P, Zhang F, Zanella M, Parak WJ. 2008B. Chem. Soc. Rev. **37**,1896–1908.
[7]. Grobmyer SR, Moudgil BMHuang X, El-Sayed I, El-Sayed M. 2010. In Cancer nanotechnology (eds Grobmyer SR, Moudgil BM), pp. 343–357.
[8]. Averitt , R.D. , Westcott , S.L. and Halas , N.J. (1999) .Journal of the Optical Society of America B , 16 , 1824 – 32 .
[9]. Huang X, El-Sayed I, El-Sayed M. 2010. A. In Cancer nanotechnology (edsGrobmyer SR, Moudgil BM, editors.), pp. 343–357 New York, NY: Humana Press
[10]. Kennedy LC, Bickford LR, Lewinski NA, Coughlin AJ, Hu Y, Day ES, West JL,.Drezek RA.Small. 2011 Jan 17; 7(2):169-83.
[11]. van de Hulst , H.C. (1957). John Wiley & Sons, Inc. , New York .
[12]. Aden , A.L. and Kerker , M. (2004) . Journal of Applied Physics , 22 , 1242 .
[13]. Hu M, Chen J, Li ZY, Au L, Hartland GV, Li X, Marquez M, Xia Y. Chem Soc Rev. 2006 Nov; 35(11):1084-94.
[14]. S. Link, M.A. El-Sayed,J Phys Chem B, 103 (21) (1999), pp. 4212–4217
[15]. M. Faraday,Philos Trans, 147 (1857), pp. 145–181
[16]. J.A. Creighton, D.G. Eadon,J Chem Soc Farad Trans, 87 (24) (1991), pp. 3881–3891
[17]. E. Prodan and P. Nordlander, Nano Lett. **3**, 543 (2003).

[18]. E. Prodan and P. Nordlander, J.Chem.Phys.120, 5400(2004)
[19]. Jankiewicz, B.J.; Choma, J.; Jamioła, D.; Jaroniec, M. Adv. Colloid Interface Sci. 2012, 170, 28–47.
[20]. Xue, J.; Wang, C.; Ma, Z.. Mater. Chem. Phys. 2007, 105, 419–425.
[21]. Ashayer, R.; Mannan, S.H.; Sajjadi, S.. Colloids Surf. A 2008, 329, 134–141.
[22]. Pham, T.; Jackson, J.B.; Halas, N.J.; Lee, T.R. Langmuir 2002, 18, 4915–4920.
[23]. Tharion, J.; Satija, J.; Mukherji, S. RSC Adv. 2014, 4, 3984–3991.
[24]. Kim, J.H.; Bryan, W.W.; Chung, H.W.; Park, C.Y.; Jacobson, A.J.; Lee, T.R. ACS Appl. Mater. Interfaces 2009, 1, 1063–1069.
[25]. Graf, C.; van Blaaderen, A.. Langmuir 2002, 18, 524–534.
[26]. Brinson, B.E.; Lassiter, J.B.; Levin, C.S.; Bardhan, R.; Mirin, N.; Halas, N.J..Langmuir 2008, 24, 14166–14171.
[27]. Lim,Y.T.;Park,O.O.;Jung,H.T.J.colloid Interface SCi.2003,263,499.
[28]. Terentyuk et al.,Journal of Biomedical Optics 14(2), 021016(March/April 2009)
[29]. K. C. Grabar, P. C. Smith, M. D. Musick, J. A. Davis, D. G. Walter, M. A. Jackson, A. P. Guthrie and M. J. Natan, J. Am.Chem.Soc.1996,118,1148
[30]. D.G. Duff, A. Baiker, P.P. Edwards, Langmuir 9, 2301 (1993).
[31]. N. R. Jana, L. Gearheart and C. J. Murphy, Langmuir, 2001, 17, 6782.
[32]. Jackson, J. B.; Halas, N. J. J. Phys. Chem. B **2001**, 105(1), 2743–2746.
[33]. English, M.D.; Waclawik, E.R.. J. Nanopart. Res. 2012, 14, 650–660.
[34]. Lim, Y.T.; Park, O.O.; Jung, H.T. J. Colloid Interface Sci. 2003, 263, 449–453.
[35]. Pol, V.G.; Gedanken, A.; Chem. Mater. 2003, 15, 1111–1118.

Chapter 3 Morphology Changes of Silica-FePt/Au Core-shell Nanospheres to Hollow Porous FePt/Au Nanoshells

3.1 Introduction

Hollow nanostructures with a lot of fascinating properties associated with the unique hollow structures, such as large surface area, low density, and high loading capacity demonstrated a large variety of applications. To meet the requirement for practical applications, such hollow nanostructures should be synthesized with high uniformity and well-controlled morphology in a reproducible, scalable, and cost-effective way. There are three major approaches for the synthesis of hollow structures: (1) hard templating method; (2) soft templating method; and (3) self-templating method. Among the three methods, the hard templating strategy is conceptually the simplest one [1,2]. In a typical process, the templates are prepared first, followed by coating their surface with a layer of shell material. Hollow structures are then obtained after selectively removing the templates. The selective removal of the hard template is achieved through chemical etching, thermal treatment or calcination. The choice of template removal method is mainly determined by the composition of hard templates. In some cases, post treatment such as reduction or calcination is required to improve certain properties of the resulting shells.

In the case of silica-FePt core-shell nanoparticles, there are also two routes to convert the core-shell composite to the hollow porous structure: (1) directly removing the silica cores by alkaline treatment (the etching of hot NaOH aqueous solution); (2) removing the silica cores after thermal treatment via supercritical ethanol. After thermal treatment,

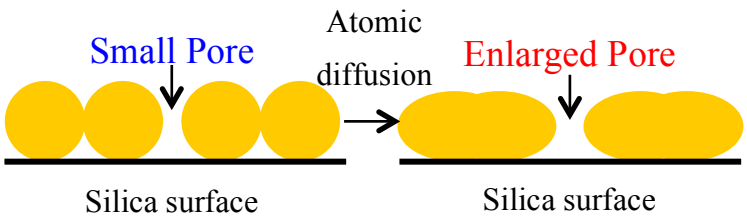

Figure 3.1 Illustration representing the formation mechanism of partially enlarged pores in thermal treatment.

not only the magnetic properties of silica-FePt core-shell nanoparticles could be improved by the change the structure of FePt NPs from fcc to fct, but also the morphology of silica-FePt core-shell nanoparticles would be changed, for example, the pores on the surface of FePt shell would be enlarged. Figure 3.1 shows the enlarging process of pores in thermal treatment. Supercritical ethanol belongs to supercritical fluid, which is any substance at a temperature and pressure above its critical point, where distinct liquid and gas phases do not exist [3,4]. Supercritical fluid can effuse through solids like a gas, and dissolve materials like a liquid [5,6]. Herein the advantages of using supercritical ethanol to treat nanoshells are listed as follows [7];

(1) Prohibition of the oxidation of Fe during the heat treatment,

(2) Prevention of the agglomeration of nanocomposites,

(3) Decrease of the sintering temperature.

Considering that both the drug loading ability and the optical properties including the photothermal capability depending on the morphology of magnetic gold nanoshells, two kinds of hollow magnetic gold nanoshells were designed and produced by two different routes in this study.

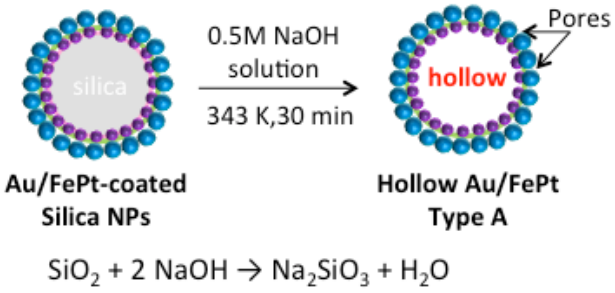

Figure 3.2 Fabrication process for hollow magnetic gold nanoshells of Type A

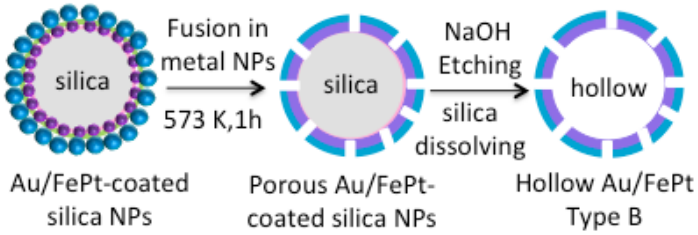

Figure 3.3 Fabrication process for hollow magnetic gold nanoshells of Type B

(1) Type A of FePt/Au nanoshell with hollow structure and small pores via the first route of directly removing the silica cores by the etching of hot NaOH aqueous solution shown in Figure 3.2;

(2) Type B of FePt/Au nanoshell with hollow structure, improved magnetic property, changed surface morphology and enlarged pores via the second rout of removing the silica cores after thermal treatment via supercritical ethanol shown in Figure 3.3.

The changes of the physiochemical characteristics of silica-core FePt/Au nanoshells after thermal treatment and the dependence of the morphology or properties of FePt/Au nanoshells on the experiment conditions of thermal treatment (heating time, heating temperature and so on) were investigated and discussed in this chapter. Additionally, supercritical water and supercritical ethanol were used for the thermal treatment of silica-core FePt/Au nanoshells to investigate the effects of supercritical fluid on thermal treatment. The critical temperature, critical pressure and critical density for water and ethanol of supercritical fluid are listed in Table 3.1

Table 3.1 Critical temperature, critical pressure and critical density of supercritical water and ethanol

Fluid	Critical temperature (K)	Critical pressure (MPa)	Critical density (g/cm^3)
H_2O	647.1	22.1	0.32
C_2H_5OH	512.4	8.1	0.27

3.2 Materials and Methods

3.2.1 Fabrication of Hollow FePt/Au Nanoshells (Type A)

The Au/FePt/silica composite nanoparticles were stirred with 1 mol dm^{-3} NaOH aqueous solution at 343 K for 1 h to dissolve the silica core particles. After removing the silica cores, the density of the Au/FePt/silica composite nanoparticles became smaller, resulting that these hollow particles were floating on water surface of tube when stirring was stopped. Hollow particles were then purified several times by washing with water and magnetic separation, and were finally redispersed in deionized water.

3.2.2 Fabrication of Hollow FePt/Au Nanoshells (Type B)

Thermal treatment of the double-layered Au/FePt/silica nanoparticles: A dispersion (7 mL) of Au/FePt/silica nanoparticles in ethanol or water was added to a reaction cell. The reaction cell (11 cm^3) was heated at 473-673 K for 0.5-12.5 h. The pressures of 7~13MPa in the reaction cell were controlled by the volume of the reaction aqueous dispersion and temperature. After rapid cooling to room temperature by putting the reaction cell into a large water bath, samples were collected by centrifuging and washing.

Removing the silica cores via NaOH etching: An aqueous dispersion of treated Au/FePt/silica nanoparticles were added and stirred with 1 mol dm^{-3} NaOH aqueous solution at 353 K for 6 h to dissolve the silica core particles. After removing the silica cores, the particle density became smaller, which result that these hollow particles were floating on water-air surface of tube when stirring was stopped. Hollow particles were subsequently purified several times by water washing and magnetic separation, and finally were redispersed in deionized water.

3.3 Results & Discussions

3.3.1 Fabrication of Hollow FePt/Au Nanoshells (Type A)

The hollow FePt/Au particles of Type A made from the silica-FePt/Au core-shell particles were successfully obtained after etching of the silica core in NaOH alkaline solution. The as-prepared silica-FePt/Au core-shell particles consist of a PDDA-modified silica core of 320 nm in diameter, a FePt-nanoparticle layer of 7.5 nm in thickness, a PEI interlayer and an outer gold layer of 15 nm in thickness. The NaOH etching effectively removed the silica core, which was evident from the difference in the contrast of TEM images before and after etching (Figure 3.4). At higher magnification, the pores of ~5nm size were observed, which is suitable for loading low-molecule weight drugs or genes.

The removal of the cores does not change the size of the particles, suggesting that hollow shell consisted of a network structure with enough mechanical stability. This good mechanical stability of Type A particles was confirmed from the TEM images of

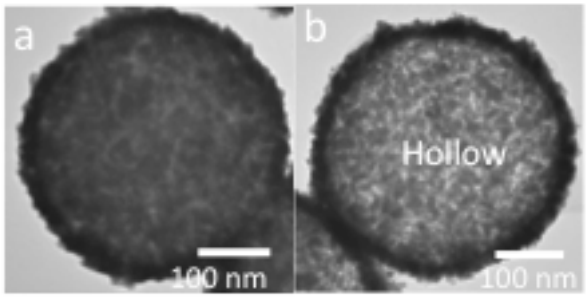

Figure 3.4 TEM images of silica/FePt/Au particles (a) and the hollow particles made from silica/FePt/Au particles via NaOH etching at 343K for 1h.

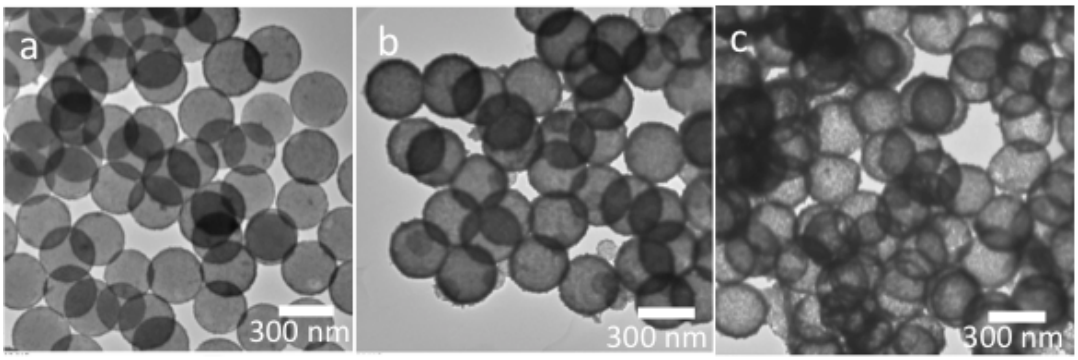

Figure 3.5 TEM images of (a) silica/FePt core-shell particles, (b) silica/FePt/Au core-shell particles and (c) hollow FePt/Au particles of Type A at low magnification.

Type A particles shown in Figure 3.5. Figure 3.5 shows three kinds of particles of (a) silica/FePt, (b) silica/FePt/Au, and (c) hollow FePt/Au particles at low magnification. All the particles obtained at each step show the good structural stability and the excellent uniformity in morphology. Almost all of double-shelled FePt/Au composites kept a complete shell even without the support of silica templates.

Figure 3.6 shows magnetization curves of the FePt/Au core-shell particles and the porous hollow spheres (Type A) were measured at 300 K in applied magnetic fields from 9 to 0 T. Magnetization per weight at 9 T increases after dissolution of the silica template particles from the core-shell particles due to the removal of the non-magnetic silica particles. The Fe content of the composite increased from 9% to 11% after removing silica cores.

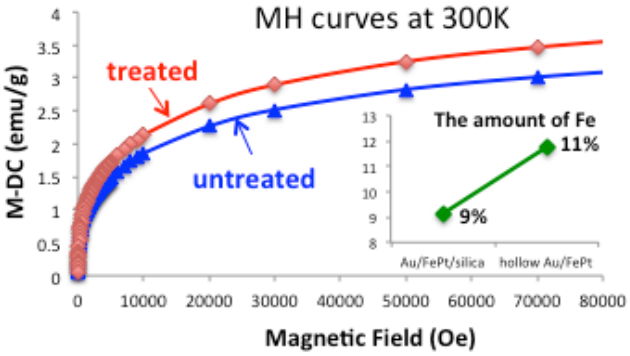

Figure 3.6 Magnetization curves of Au/FePt /silica core-shell particles and hollow particles measured at 300 K in applied magnetic fields from 9 to 0 T. Inset is the change in the Fe content of Au/FePt /silica composite before and after the etching.

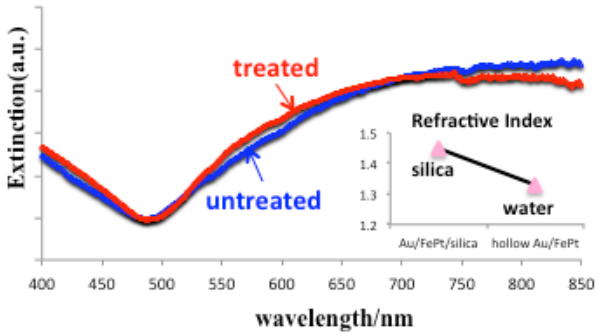

Figure 3.7. Extinction spectra of FePt/Au core-shell particles before (blue line) and after (red line) silica core removal. Inset is the change in refractive index of the core before and after silica removal.

The structural changes are reflected in the optical spectra shown in Figure 3.7. Silica core removal by NaOH etching affects the peak position—a blue shift is observed relative to the core-shell particles (720 vs 780 nm). This may be explained by a decrease in the refractive index of core material from 1.34 (silica) to 1.0 (air) or water (1.33).

3.3.1.1 Dependence on NaOH Etching Time

Figure 3.8 shows the dissolving process of the silica/FePt/Au composite particles via NaOH etching. After etching for 0.5h, a partly dissolved silica core encapsulated in FePt/Au shell was observed in Figure 3.8b, indicating that the dissolution of silica cores was proceeding. After etching for 1h, the silica core was completely dissolved and then

a hollow porous particle was obtained (Figure 3.8c).

3.3.1.2 Structure Dependence of Mechanical Stability

Figure 3.9 shows TEM images of three kinds of particles of silica/FePt, silica/Au, silica/FePt/Au and their hollow particles at low magnification. All kinds of particles had a complete shell structure and showed a good uniformity in morphology and particle

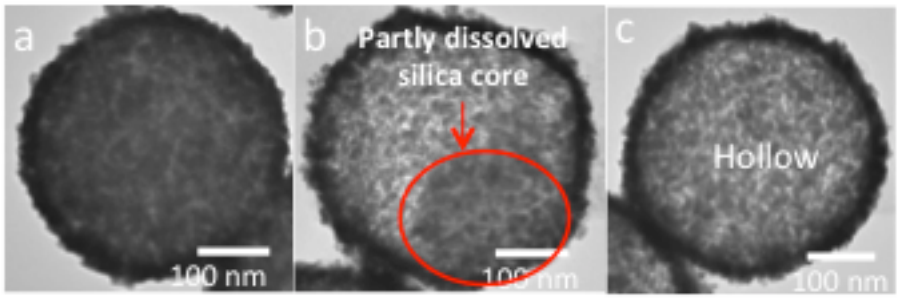

Figure 3.8 TEM images of silica/FePt/Au particles before (a), after NaOH etching for 0.5 h (b) and after etching for 1h(c).

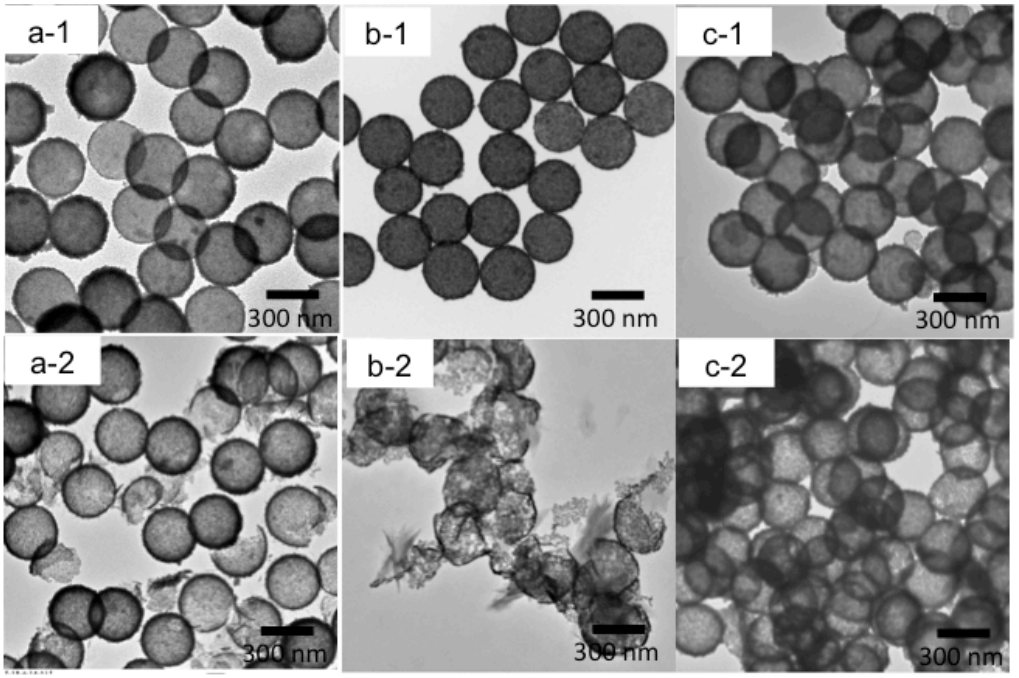

Figure 3.9 TEM images of three kinds of particles and their hollow particles: FePt nanoshells (a1-2), gold nanoshells (b1-2), and Au/FePt nanoshells (c1-2)

size (Figure 3.9 a1,b1,c1). However, only double-layered FePt/Au particles completely kept the shell structure after dissolution of the silica cores (Figure 3.9 c2). In the case of the monolayered FePt nanoshells, part of particles was broken (Figure 3.9 a2). In the case of the monolayered gold nanoshells, most of particles were broken apart (Figure 3.9 b2). These TEM images indicate that the mechanical stability of FePt/Au composites was greatly enhanced by using the double-layered structure.

3.3.2 Fabrication of Hollow FePt/Au Nanoshells (Type B)

Figure 3.10 shows TEM images of the FePt/Au core-shell particles before and after thermal treatment with supercritical ethanol at 573 K and 14 MPa for 1 hour, and the hollow particles made from the thermally treated FePt/Au core-shell particles by NaOH etching. The as-prepared FePt/Au core-shell particles (Fig. 3.10 a1-2) consist of a PDDA-modified silica core of 320 nm in diameter, a FePt interlayer of 7.5 nm in thickness and an Au outer layer of 15 nm in thickness. After the thermal treatment, the silica particles were still left, and the metal nanoparticles were fused together so that the shell surface became smooth (Fig. 3.10 b1-2). Particle-shaped FePt and gold particles were not observed by the fusion and there were a lot of large pores on the shell surface. Maximum pore size was 20 nm. Figure 3.1 represents the possible formation mechanism of enlarged pores after thermal treatment. Metallic NPs with a short distance probably fused together whereas the distance between these fused NPs and other fused

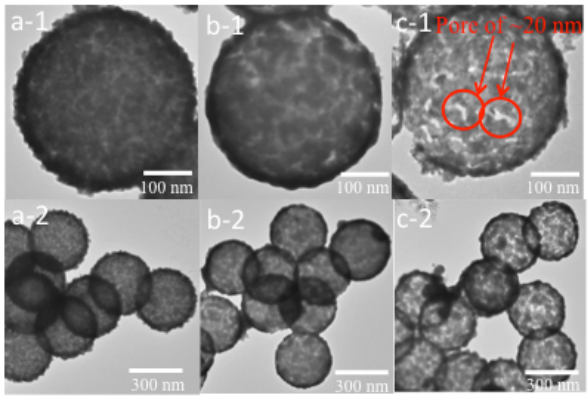

Figure 3.10 TEM images of 320 nm-silica/FePt/Au particles before (a1-2), after (b1-2) thermal treatment and the hollow particles (c1-2) treated by NaOH etching for 1h.

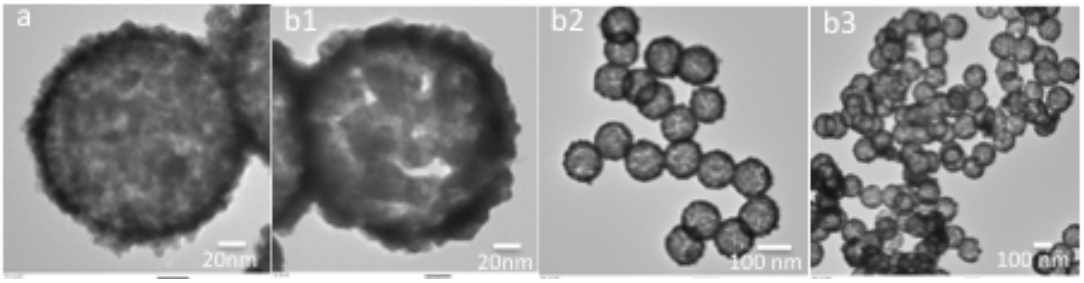

Figure 3.11 TEM images of 120 nm-silica/FePt/Au particles before (a), after thermal treatment and the hollow particles (b1-3) treated by NaOH etching for 1h.

NPs was increased. As a result, some pores disappeared whereas other pores were enlarged. It is reported that the decomposition of PDDA molecules starts from 553 K while the decomposition of PEI molecules starts from 533 K in air atmosphere [8]. Therefore, both the PDDA and PEI molecules were probably decomposed during the thermal treatment. After the silica removal, a complete shell with large pores (Type B, Figure 3.10 c1-3) was successfully remained. Moreover, the porous surface and hollow structure also successfully obtained using the 120 nm-silica/FePt/Au particles shown in Figure 3.11. These hollow particles having uniform particle size and morphology not only have a small size of within 150 nm but also show excellent mechanical and thermal stability.

Figure 3.12 shows XRD patterns of the silica/FePt/Au core-shell particles untreated and treated with supercritical ethanol at 573 K for 1h. Their crystallite sizes calculated from their XRD patterns as well as the shell thickness and pore size calculated from their TEM images were summarized in Table 3.2. There are no various differences in the peak location but differences in the crystallite size. The crystallite sizes of metal nanoparticles increased greatly after the supercritical ethanol treatment due to the fusion of metal particles.

Figure 3.13 shows magnetization curves of the FePt/Au core-shell particles and the porous spheres made from the FePt/Au core-shell particles treated with supercritical ethanol at 573 K for 1h. They were measured at 300 K in applied magnetic fields from 9 to 0 T. The magnetization of the core-shell particles after treatment at high magnetic field was higher than that of the untreated core-shell particles, which might result from the structure change of partly FePt NPs from fcc to fct and the increase of the crystallite

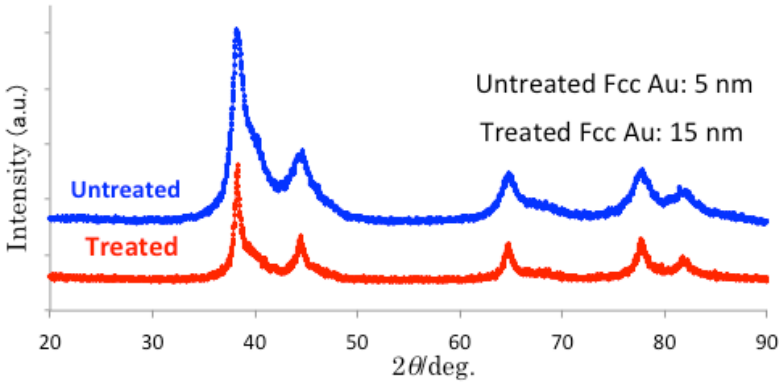

Figure 3.12 XRD patterns of silica/FePt/Au core-shell particles and the silica/FePt/Au core-shell particles treated with supercritical ethanol at 573 K for 1h.

Table 3.2 Changes of shell thickness, pore size and crystallite sizes in silica/FePt/Au core-shell particles before and after thermal treatment via ethanol

Particles	Shell thickness (nm)	Pore size (nm)	Au Crystallite size (nm)	FePt Crystallite size (nm)
Before treatment(untreated)	23	~5	5	2
After treatment (treated)	20	~20	15	5.5

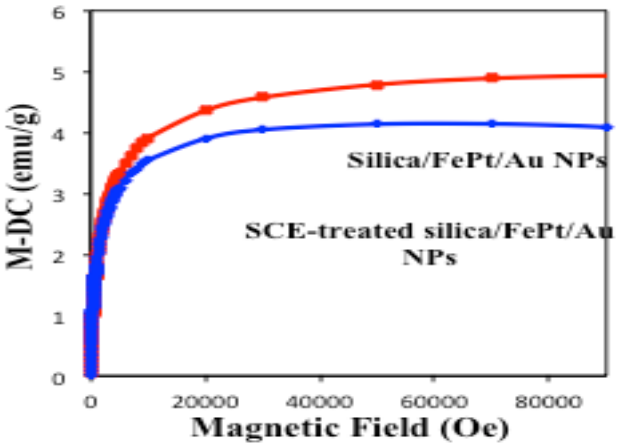

Figure 3.13 Magnetization curves of silica/FePt/Au core-shell particles untreated and treated with supercritical ethanol at 573 K for 1h. These curves were measured at 300 K in applied magnetic fields from 9 to -9 T.

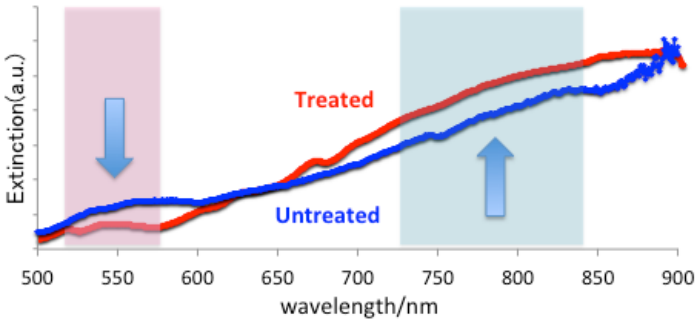

Figure 3.14 UV-Vis SPR spectra of silica/FePt/Au core-shell particles and the silica/FePt/Au core-shell particles treated with supercritical ethanol at 573 K for 1h.

size of FePt after the supercritical ethanol treatment due to the fusion of metal nanoparticles.

Figure 3.14 displays the changes of extinction spectra of the silica/FePt/Au core-shell particles by the thermal treatment. The extinction spectrum of the silica/FePt/Au core-shell particles before treatment is shown in the blue line whereas the extinction spectrum of the treated silica/FePt/Au core-shell particles in the red line. By the thermal treatment at 573K for 1h, the broad maximum of the nanoshell spectrum originally observed at 830 nm has been shifted to 860 nm and is slightly broader, suggesting that the shell nanostructure has been changed as follows; TEM images show that the surface of the treated nanoshells became more smooth and thinner. The spectral shift observed in Figure 3.14 is probably due to the changes in the morphology, and the slight change in the peak width can be attributed to the aggregation and destruction of the little part of the nanoshell.

3.3.2.1 Structure Dependence of Thermal Stability

To investigate the structure dependence of thermal stability of double-layered silica/FePt/Au core-shell particles, three kinds of particles including silica/Au core-shell particles with a Au shell of 15 nm in thickness, silica/FePt core-shell particles with a FePt shell of 7.5 nm in thickness and silica/FePt/Au core-shell particles with a FePt interlayer of 7.5 nm in thickness and a Au outer layer of 15 nm in thickness were treated

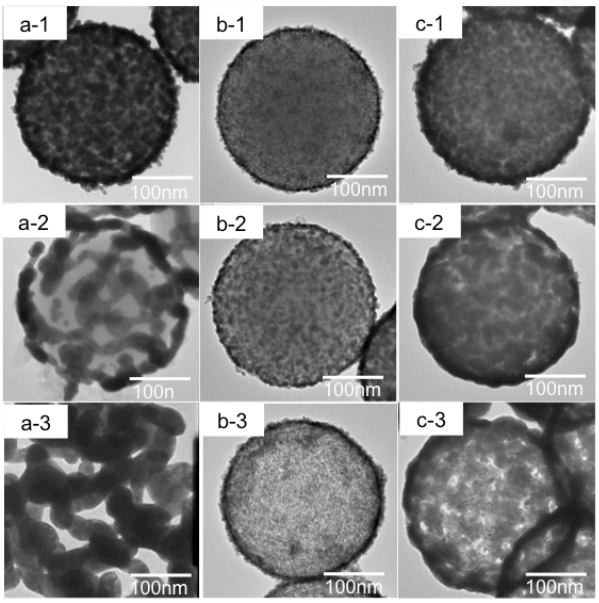

Figure 3.15 TEM images of various nanoshells before and after thermal treatment and the hollow nanoshells made from them: silica/Au (a1-3), silica/FePt (b1-3) and silica/FePt/Au (c1-3)

Table 3.3 Changes of three kinds of nanoshells on the silica core in shell thickness and crystallite size after thermal treatment.

Particles	Shell thickness (nm)	Au Crystallite size (nm)	FePt Crystallite size (nm)
Silica/Au	14	3	-
Treated Silica/Au	-	25	-
Silica/FePt	7	-	2
Treated Silica/FePt	5	-	6.7
Silica/FePt/Au	23	5	2
Treated Silica/FePt/Au	20	15	5.5

by ethanol at 573K for 1h, followed by NaOH etching at 543K for 1h. Table 3.3 shows the changes of these nanoshells on the silica core in shell thickness and crystallite size after the thermal treatment. TEM images of the obtained particles at each step are shown in Figure 3.15. The gold nanoparticles of silica/Au core-shell particles melt

together but failed to form a netlike structure after the thermal treatment (Figure 3.15 a1-2). After NaOH etching, a lot of large gold nanoclusters are observed in TEM image (Figure 3.15 a3), which indicates the structure of gold nanoshell is too weak to endure the thermal treatment under the conditions designed in this thesis. The poor thermal stability of gold nanoshell also had been experimentally determined by other researchers. They found that gold nanoshells on the silica core began to melt when subjected to a 2–3 h heating at 275°C and were completely destroyed following exposure to a heating at 325 °C [9]. This is significantly below the bulk gold melting temperature of 1064°C. On the other hand, FePt nanoshells on the silica core (Figure 3.15 b1-2) with the relatively high thermal ability maintained their core-shell structure after thermal treatment and successfully kept a complete shell even without the support of silica cores (Figure 3.15 b3). This suggests that FePt nanoshells possess a higher thermal stability than gold shells. This is one of the reasons why I chose FePt NPs to build a double-layered structure and enhance not only the mechanical stability but also the thermal stability of gold nanoshells.

3.3.2.2 Dependence on Treatment Temperature

Figure 3.16 shows TEM images of the silica/FePt/Au core-shell particles with Au shell of 15nm and FePt shell of 7.5 nm treated with subcritical or supercritical ethanol (SCE) at 473-673 K for 1h. Table 3.4 shows the changes of silica/FePt/Au core-shell particles treated at the different temperature in shell thickness and crystallite size. After SCE treatment at 473 K, there were no various changes of silica/FePt/Au core-shell particles in morphology and particle size. When the treatment temperature is increased to 573 K, the morphology of the silica/FePt/Au core-shell particles was obviously changed. Neighboring metal nanoparticles were fused together and the netlike structure was formed on the surface of the silica cores, resulting that the shell surface became smooth and the pore size became large. When the treatment temperature is increased to 673 K, the fusion of the metal nanoclusters went more deeply. Some particles had a complete shell structure and their surface became smoother and seamless. Oppositely, the shell structure of some particles appears broken up (not shown). Naked silica particles and large clusters were observed. It was reported that most of silica/FePt core-shell particles could maintain the shell structure even after treated at 673 K for

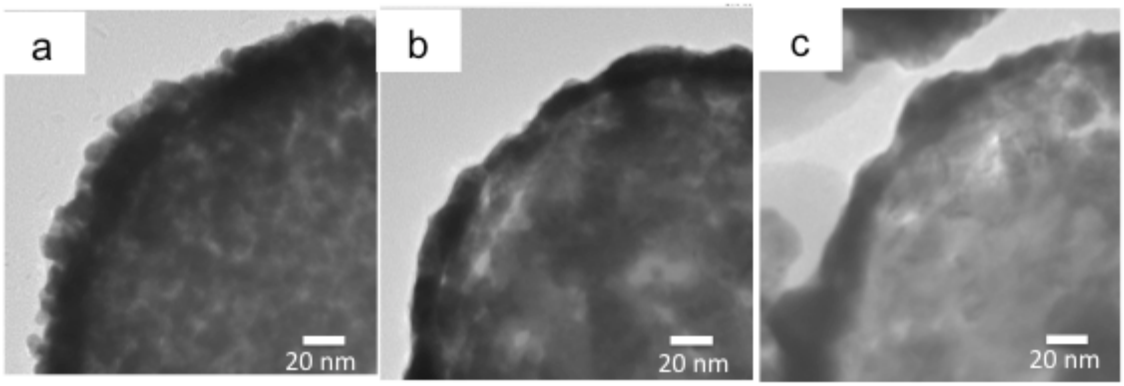

Figure 3.16 TEM images of the silica/FePt/Au core-shell particles with Au shell of about 15nm treated with ethanol at 473(a), 573K(b) and 673 K(c) for 1h.

Table 3.4 Changes of silica/FePt/Au core-shell particles treated at the different temperature in shell thickness and crystallite size

Treatment Temperature (K)	Shell thickness (nm)	Au Crystallite size (nm)	FePt Crystallite size (nm)
Untreated	23	5	2
473	23	5	2
573	20	15	5.5
673	19	21	8.2

1.5h. This suggests that the thermal stability of composite shells was decreased by the presence of the outer gold shells.

3.3.2.3 Influence of Shell Thickness on Structurally Stability

To investigate the influence of the thickness of Au shell on the structural stability of hollow FePt/Au particles, silica/FePt/Au core-shell particles with various thickness of Au shell (15nm, 30nm, 45nm) were prepared using the silica particles of 320 nm in diameter and the thickness of the FePt shell was set to be 7.5 nm. There were no obvious changes in the crystallite sizes of FePt NPs or gold NPs even when the shell thickness of Au increased. Then all of them were treated with supercritical ethanol at 573 K for 1h. Figure 3.17 shows TEM images of silica/FePt/Au core-shell particles with

various thickness of Au shell after the thermal treatment. When the thickness of the Au shell is 15nm, the surface coverage of metal nanoparticles was less than 100% so that a lot pores were observed on the shell surface of silica/FePt/Au core-shell particles and these pores were enlarged after the thermal treatment; a netlike structure was obtained on the surface of silica cores. When the thickness of the Au shell increased to 30 nm, the surface coverage of metal nanoparticles is close to 100 %, few small pores were observed on the surface of silica/FePt/Au core-shell particles. After the thermal treatment, the metal nanoparticles fused together to form a smooth and almost complete shell. This result suggests the thickness of the Au shell should be controlled under 30 nm in order to obtain a porous structure after thermal treatment. Additionally, the aggregation of silica/FePt/Au core-shell particles was observed and the surface of some nanoshells connected with each other via the fusion of gold nanoparticles on their surface. When the thickness of the Au shell increased to 45nm, the surface coverage of

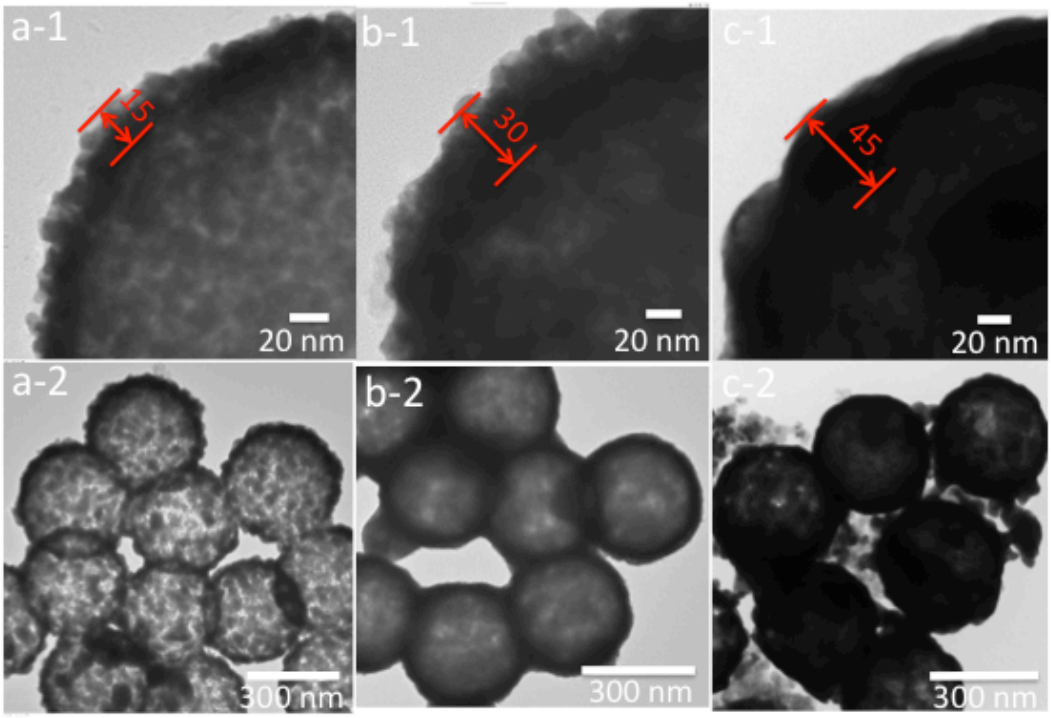

Figure 3.17 TEM images of various silica/FePt/Au core-shell particles with Au shell in thickness of 15nm(a1), 30nm(b1) and 45 nm (c1) and their particles with Au shell in thickness of 15nm(a2), 30nm(b2) and 45 nm (c2) treated with ethanol at 573K for 1h.

metal nanoparticles reached above 100%. The surface of the silica/FePt/Au core-shell particles was smooth and seamless. After the thermal treatment, some separated clusters were observed, which might be gold clusters stripped from the shell. The separation of these gold nanoparticles resulted in some empty space on the surface of silica/FePt/Au core-shell particles. These results suggest that the thermal stability of the nanoshell on the silica core particles was greatly decreased by the presence of the thick gold shell.

3.4 Conclusions

In this chapter, two types of hollow porous spheres with different morphology and properties (Type A and Type B) were synthesized and their properties were discussed.

The first type of the hollow FePt/Au particles named as Type A was a hollow double-layered shell consisting of a FePt interior shell and an Au outer shell made from silica/FePt/Au core-shell particles by removal of the silica cores via using NaOH etching. After NaOH etching, there were no changes in both the morphology and the total size. There are many small pores ($d < 5$ nm) evenly distributed on the surface of the FePt/Au particles. The total thickness of the FePt/Au nanoshells and the surface coverage of metal nanoparticles could be easily controlled by changing the amount of metal nanoparticles deposited on the core. The presence of the interior layer of FePt resulted in an increase of the mechanical strength of the hollow particles due to its relatively higher structure strength. The extinction peak of the hollow particles showed a blue-shift because of a decrease in the refractive index of the core material from silica to air or water.

The second type of the hollow FePt/Au particles named as Type B was also a hollow double-layered shell composed of a FePt interior shell and an Au outer shell made from silica/FePt/Au core-shell particles by a thermal treatment followed by NaOH etching. Neighboring metal nanoparticles were fused together during the thermal treatment, resulting in the formation of a netlike shell with a lot of enlarged pores (~20 nm) and a smooth surface. A red-shift of the peak in the extinction spectra was originated in the changes of the morphology in the nanoshell; the surface of the nanoshells became smoother and more complete with the increase of the treatment temperature or thickness of Au shell. The structural stability of the hollow particles was strongly enhanced by the presence of the FePt shell.

Reference

[1].Qi, J.; Lai, X.; Wang, J.; Tang, H.; Ren, H.; Yang, Y.; Jin, Q.; Zhang, L.; Yu, R.; Ma, G.; et al. Chem. Soc. Rev. 2015, 44,6749−6773.

[2]. Hu, J.; Chen, M.; Fang, X.; Wu, L. Chem. Soc. Rev. 2011, 40, 5472−5491.

[3]. Zhang Y, Erkey C. J Supercritical Fluids 2006, 38, 252-67.

[4]. Reverchon E, Adami R. J Supercritical Fluid 2006, 37, 1-22.

[5] Y. Kitamoto, J. He, Electrochim. Acta, 54, 2009, 5969–5972

[6] T. Fuchigami, et.al. Langmuir 2011, 27, 2923-2928

[7] T. Iwamoto, Y. Kitamoto, N. Toshima, Phys. B, 404, 2009, 2080–2085

[8] P.simon et al. J Therm Anal Cal, Vol. 84, p. 727, 2006.

[9]Radloff, C. et al; Applied Physics Letters; vol. 79, No. 5, Jul. 30, 2001; pp. 674-676.

Chapter 4 Heat Generated by Porous FePt/Au Nanoshells

4.1 Introduction

Photothermal therapy (PTT) has been taken as a promising cancer treatment. In PTT, light-absorbing nanoparticles are delivered to a tumor, which is subsequently irradiated with the light within the therapeutic wavelength band (700 nm – 1100 nm). Then the electromagnetic radiation interacts with these highly absorbing nanoparticles to produce local heating, which enables thermal damage of the tumor. The choice of nanoparticles for achieving efficient heating for photothermal therapy application is based on their extinction efficiencies including absorption and scattering efficiencies, Q_{abs} and Q_{sca}, which depend on the size, shape, and composition of the nanoparticles [1]. Among various light-absorbing nanoparticles, gold nanoshells are of particular importance due to their relatively lower toxicity and comparatively larger photothermal efficiency. The photothermal conversion efficacy of gold nanoshells depends on their dimensions, composition, refractive indices of the core material and surrounding material [1]. Many research efforts have thus been devoted to the analyses of these dependencies with the intention to maximize the energy absorbed by nanoshells irradiated by a NIR laser. In this thesis, one of the important purposes that FePt NPs was chosen to combine with gold nanoshell is to obtain an improved photothermal conversion efficiency due to the synergistic effect of gold shell and FePt shell.

In this chapter, I systematically evaluated the potential of two types of FePt/Au nanoshell particles as a photo-absorber for photothermal therapy. Four kinds of gold shell-based plasmonic particles including silica/Au core-shell particles, silica/FePt core-shell particles, silica/FePt/Au double-layered core-shell particles and silica/iron oxide NPs/Au double-layered core-shell particles were prepared and used in the photothermal experiments. The size and shell thickness of these four kinds of gold shell-based plasmonic particles are listed in Table 4.1. The photothermal effects of various particles were evaluated and compared with each other. The effects of four important factors including core material, shell composition, particle size and shell thickness were investigated.

In this study, I used a continuous wave (CW) laser to irradiate four kinds of various

gold shell-based plasmonic particles and investigated their photothermal responses because using a CW laser to optically excite gold nanoshells can obtain an enduring, moderate temperature increase that is best suited for hyperthermia treatment of cancer. On the other hand, the particle is irradiated by laser in water medium at a wavelength of 800 nm where absorption in biological tissues is very low. Considering that the irradiation of a long time or high power would be harmful for healthy cells, I restrict the maximum irradiation time within 300 s and the laser power within 0.5W.

Table 4.1 Size and shell thickness of various gold shell-based plasmonic particles

Particles	Silica Core Size (nm)	Magnetic Shell thickness (nm)	Au shell thickness (nm)
silica/Au	120 or 320	-	15
silica/FePt	120 or 320	10-20	-
silica/FePt/Au	120 or 320	10-20	15

4.2 Materials and Methods

4.2.1Preparation of Silica/Au Core-shell Nanoparticles

4.2.1.1 Preparation of Amine-functionalized Silica Nanoparticles

A supernatant of silica of 120 nm in diameter (13.3 mg) or silica of 320 nm in diameter (40 mg) was dispersed in ethanol, then 3 ml ammonium aqueous (28 wt%) and 50 μl of 3-aminopropyl- triethoxysilane (APTES) were added, following the stirring of 24 h. The resulted solution was centrifuged and washed by deionized water three times. Finally, APTES-modified silica nanoparticles were redispersed and stored in 50 ml of ethanol for further use.

4.2.1.2 Preparation of Silica/Au Core-shell Nanoparticles

5 ml of APTES-modified silica nanoparticle solution and 5 ml of THPC-Au colloid solution were mixed and stirred for 2 h at room temperature, following sitting at 4°C overnight. Then the solution was centrifuged and washed by deionized water three times.

The precipitate (Au-seeded silica nanoparticles) was redispersed in 50 ml of deionized water. To grow the Au shell, 200 μL of Au-seeded silica nanoparticle solution was added to 4 ml of the Au ion solution, after which 40~80 μL of formaldehyde were rapidly dropped into the solution. Then the precipitate was collected and washed with deionized water three times after stirring for 1 h at room temperature. The final precipitate was redispersed in deionized water and stored at 4°C, yielding silica/Au nanoshells.

4.2.2 Photothermal Behavior Measurements

Under the laser irradiation, the light-absorbing nanoparticles generate heat, which is quickly transferred to water by a thermal conduction process at the surface. Subsequently, the temperature of the water around the nanoparticles also rises up. Therefore, the heat generated by the nanoparticles can be determined by measuring the temperature increase of their suspension after receiving the optical energy provided by the laser.

An experimental setup for measuring the temperature change of the sample solution during the laser irradiation is shown in Figure 4.1. Various sample solutions with the concentrations of 8 x 10^9~1.6 x 10^7 particles/mL were placed into a 1 cm path length plastic cuvette (Malvern), and were diluted with a final volume of 2 mL deionized water. Pure water and silica dispersion (4 x 10^9 particles/mL) were used as controls. The cuvette was clamped to a foam cap to reduce the heat loss. A fiber optic temperature sensor (Neoptix, T1S-24716A) connected to a converter (Neoptix, ReFlex-1) is placed into the solution at a middle height of the sample solution and kept away from the illumination path of the laser light. Then the cuvette is sealed and irradiated with NIR light (center wavelength of 808 nm, 0.5 W, Spot size of 7mm^2) from the Ti: sapphire laser (Coherent, Mira 900) that is operated at a continuous-wave (CW) mode. The laser intensity was measured and confirmed by a portable laser power meter (Spectra-Physics, model 407A) before the irradiation. A computer connected with the converter was used to collect the data in every second. The temperature sensor could accurately measure temperature from -20 to 200 °C.

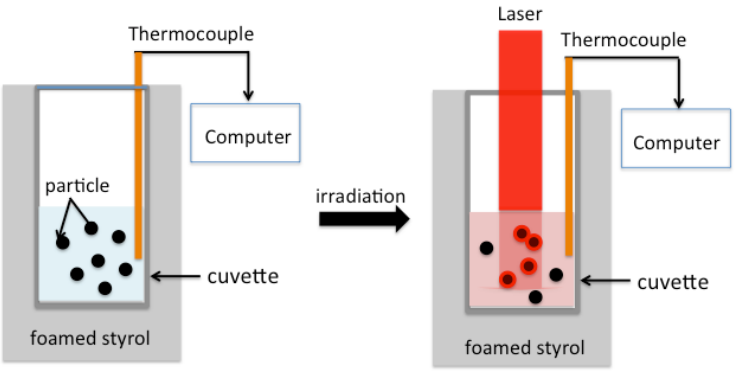

Figure 4.1 Illustration of experimental setup for measuring the photothermal effect, particles indicates the aqueous solution containing various gold shell based plasmonic particles in a 1 cm path length plastic cuvette, the red bar represents an optical fiber delivering NIR laser light (808 nm) through the cuvette window and the orange line indicates the temperature sensor which is connected with the computer.

Assuming the heat loss of the whole system during the irradiation is zero and all the absorbed optical energy by samples is converted to heat, the photothermal efficiency (η) defined to be the ratio of the thermal energy generated by the nanoparticles (Q_{out}) to the optical energy provided by the laser light (Q_{in}) is given as following:

$$\eta = Q_{out} / (Q_{in} - Q_0)$$

where Q_0 is the loss of optical energy due to light absorption by the solvent of the sample solution. In this study, Q_0 can be ignored because no obvious temperature change of the pure water without any nanoparticles is observed after the laser irradiation. And the function $Q_{in}(I, t)$ representing an energy source coming from light dissipation are described by $Q_{in}(I, t) = I \cdot t$, where I is the laser power in watt and t is the irradiation time. Therefore the photothermal conversion efficiency (η) is described as

$$\eta = Q_{out} / Q_{in} = m_D \cdot C_D (T_{max} - T_{surr}) / I \cdot t$$

where the mass of the sample solution m_D is 2g since the volume of the irradiated sample solution is 2 mL and the weight density of the sample solution is approximated to 1g/mL, the weight density of water. The heat capacity of the sample solution C_D is 2.0 g is approximated to be 4.2 J/g °C (the heat capacity of the solvent water) due to low

concentration. T_{max} is the steady state maximum temperature of the sample solution and T_{surr} is the ambient room temperature, therefore, $T_{max} - T_{surr}$ means the increased temperature (ΔT) of the sample solution. The heating rate that is defined as the average rate of temperature increase in degrees per min is equal to the heat transfer rate of the system at the maximum steady-state temperature as follows:

$$\text{heating rate} = \Delta T/t = (T_{max} - T_{surr})/t$$

If the mass of the sample nanoparticle is m_s , the photothermal effect of the sample nanoparticles is then calculated according to:

$$\text{Photothermal effect} = Q_{out}/m_s \cdot t = m_D \cdot C_D (T_{max} - T_{surr})/m_s \cdot t$$

4.3 Results & Discussions

A representative graph of the temperature difference, i.e., the temperature increase, for pure water and the water suspension of various concentrations (4 x 10^9particles/mL), which were irradiated with a laser that has an output power of 0.5 W for approximately 10 min, is shown in Figure 4.2. Experiments in aqueous solution showed that the temperature increased with increasing exposure time and plateaued after about 10 min of light exposure. In the case of the pure water and bare silica particles, the temperature increase (blue curve for water and pink curve for silica Figure 4.2) was negligible. In contrast, the temperature of the sample solutions including light-absorbing nanoparticles was found to depend on laser irradiation time. For example, the temperature increase after 600 s of the water suspension containing the Au colloids (~3 nm) NPs was 4.5 °C (light blue curve, Figure 4.2), indicating a photothermal effect. In the case of silica/FePt particles, the temperature increase after 600 s was 9.5 °C (green curve, Figure 4.2), far higher than that of Au colloids, demonstrating a photothermal effect of magnetic FePt NPs. After coated by a gold shell, the temperature increase of silica/FePt/Au particles after 600 s was 11.5 °C, (black curve, Figure 4.2) indicating the combination of gold shell and FePt shell caused an enhanced photothermal effect. When silica cores was dissolved, the temperature increase of hollow nanoshell particles (Type A) after 600 s was 13 °C (purple curve, Figure 4.2), which suggests the photothermal effect was improved. This improvement should be caused by the change of core dielectric constant from 2.04(silica) to 1.0(air) or 1.33 (water). It was reported that the strengths of the

extinction peaks (dipole and quadrupole) were increased with the decreasing core dielectric constant and ascribed the behavior to the plasmon hybridization [2]. The increased peak intensity of hollow nanoshell particles (Type A) leads to an improved absorption efficiency [3]. On the other hand, when silica/FePt/Au particles were treated by supercritical ethanol at 573K for 1 h, the temperature increase of treated particles after 600 s was 12 °C (orange curve), a little higher than that of untreated particles, which well consonants with the changes in extinction spectra. In the extinction spectra, the peak of treated particles showed a slightly red shift. After the removal of silica cores, the temperature increase after 600 s of hollow FePt/Au nanoshell particles (Type B) was about 12 °C (red curve, Figure 4.2), a little higher than that of SCE-treated particles with a silica core. Theoretically, the photothermal effect of a gold shell-based particle with a hollow structure would stronger than that of a gold shell-based particle due to the decreasing core dielectric constant.

To well understand the photothermal behavior of these nanoparticles, I compared their mean heating rate and photothermal efficiency calculated from the equation

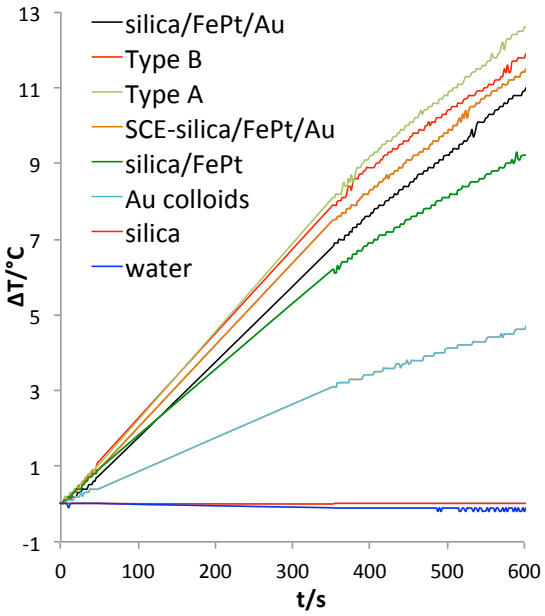

Figure 4.2 Graph of the temperature increase for pure water and a water suspension of nanoshell NPs (4 x 10^{-9}/mL), irradiated by CW laser light with an output power of 0.5 W for approximately 10 min. Pure water and silica dispersion (4 x 10^{9} particles/mL) were used as controls.

discussed above. The results show in Figure 4.3 and Table 4.2. Among all the samples, the hollow FePt/Au nanoshell particles of Type A showed the highest photothermal efficiency and heating rate. The heating rate for the suspension of hollow nanoshell NPs (Type A and Type B) in the experiment was approximately 1 °C/min, which is slow enough to heat tissue in a controllable manner, but efficient enough to increase the temperature above the hyperthermia level [4,5]. The above data indicate that both of Type A and Type B hollow nanoshells acted as an efficient photothermal mediator.

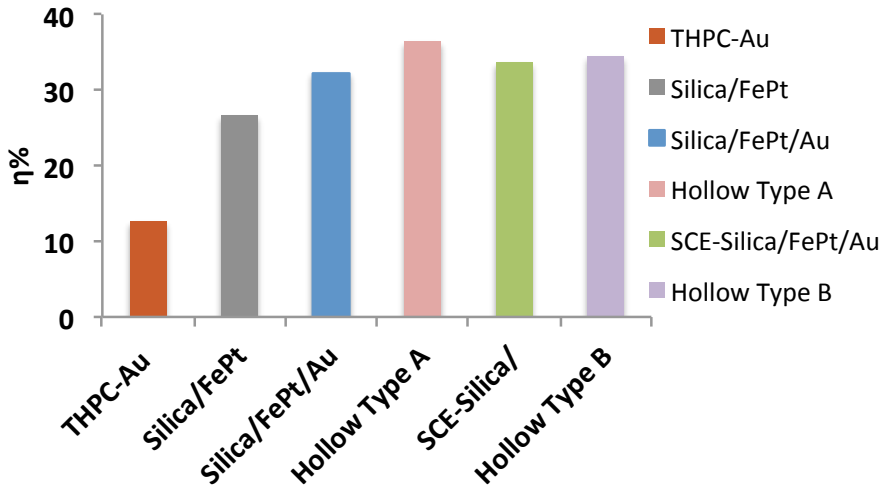

Figure 4.3 Mean photothermal efficiency from the conversion of light to heat in various sample solutions prepared in this study

Table 4.2 Comparisons of mean photothermal efficiency from the conversion of light to heat in various sample solutions prepared in this study

Samples	Heating rate °C/min	η%
THPC-Au NPs	0.5	12.6
Silica/FePt NPs	1.0	26.6
Silica/FePt/Au NPs	1.2	32.2
Hollow Type A NPs	1.3	36.4
SCE-Silica/FePt/Au NPs	1.2	33.6
Hollow Type B NPs	1.2	34.4

4.3.1 Heat Generated by Silica-core FePt Nanoshells

4.3.1.1 Dependence on Shell Thickness

As well known, in the case of gold nanoshells, the shell thickness strongly affects the optical property of gold nanoshells as well as their photothermal behavior. To gain insight into the thickness dependence of FePt shell, three types of various silica-core FePt nanoshells with the different thickness of 10nm, 15nm and 20 nm synthesized by changing the amount of silica cores of 120 nm in diameter were fabricated and their photothermal experiments were conducted. TEM images and UV-Vis-NIR spectra of the obtained silica/FePt core-shell nanoparticles are shown in Figure 4.4. When changing the thickness of FePt nanoshells, no obvious changes was observed on the UV-Vis-NIR spectra of these FePt nanoshells. The results of UV-Vis-NIR spectra provide evidence that the light absorption of FePt nanoshells is non-selective from the visible to NIR regain and don' t strongly depend on the shell thickness, which is completely different with those of gold nanoshells. The Characteristics of various silica/FePt nanoshells with different thickness and the results of photothermal experiments are list in Table 4.3 while the temperature change (ΔT) over a period of 2 min as a function of shell thickness of FePt shells and the changes of photothermal effect as a function of the weight percent of FePt NPs in silica/FePt particles are shown

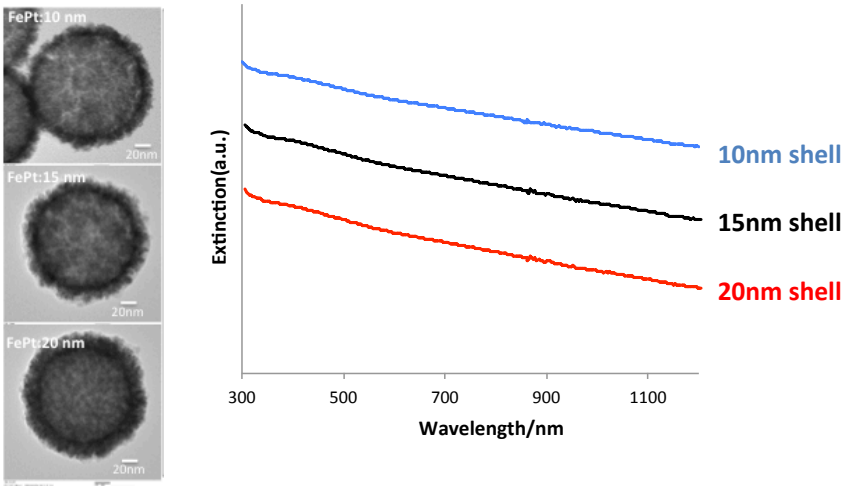

Figure 4.4 TEM images and UV-Vis-NIR spectra of three types of various FePt nanoshells with different shell thickness.

Table 4.3 Characteristics of various silica/FePt nanoshells with different thicknesses and various important data of photothermal experiments

Sample	FePt wt%	Crystalize Size/nm	ΔT/°C	Photothermal efficiency of FePt nanoshells (η%)
silica/FePt-10nm	63.2	1.9	1.4	7.8
silica/FePt-15nm	67.4	2.1	3.8	21.3
silica/FePt-20nm	76.7	2.2	4.8	26.8

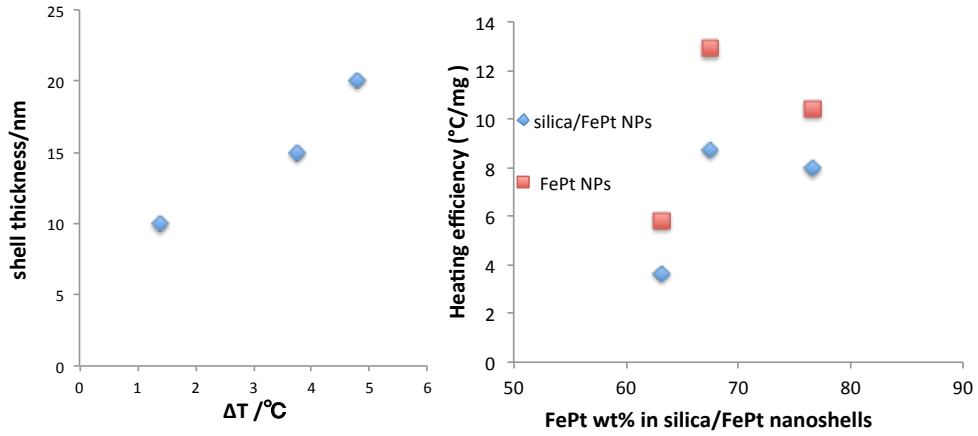

Figure 4.5 Temperature change (ΔT) over a period of 2 min as a function of thickness of FePt shell (left) and Changes of photothermal effect of silica/FePt NPs and FePt NPs as a function of the weight percent of FePt NPs in silica/FePt particles (right)

in Figure 4.5. With increasing shell thickness, the temperature change as well as the photothermal effect of silica/FePt particles increased. However, it should be noted that the photothermal effect of FePt NPs accumulating on the silica cores increased with increasing the weigh percent of FePt NPs in silica/FePt composites at weight percent of < 68%, thickness: 15nm). At higher weight percent (>68%, thickness: 15nm), no further increase in the photothermal effect of FePt NPs, which may be explained by the difference in the distance the laser spot can pass through in various sample solutions. Figure 4.5 revealed that the FePt nanoshells with the thickness of 15 nm had higher photothermal effect than other two types.

Furthermore, in order to evaluate the photothermal effect of FePt shells fabricated in this study, the photothermal behavior of FePt nanoshells and gold nanoshells, all which

consist of a 120 nm silica core and a metal shell of 20 nm, were measured and compared. The extinction spectra of FePt nanoshells and gold nanoshells are presented in Figure 4.6. Peaks at 812 nm represent plasma resonance of gold nanoshells. For FePt NPs, instead of the unique feature of plasmon resonance as that of Au nanostructures, a broadband absorption at NIR region was observed. The 808 nm laser heat conversion efficiency ($\eta\%_{FePt}$) of the FePt nanoshells of 120/20-nm can be calculated to be 26.8 % while the 808 nm laser heat conversion efficiency ($\eta\%_{Au}$) of the gold nanoshells can be calculated to be 35.1 %. For FePt nanoshells (26.8%) is very consistent with the literature value of 30% for FePt NPs [6].

It should be noticed that the photothermal effect of FePt NPs as well as FePt NPs-based nanostructure is not due to surface plasmon resonance, which occurs in the case of plasmonic nanoparticles. A physical mechanism should be responsible for the photothermal effect of FePt NPs. In contrast to plasmonic gold nanoshells, as the photons were captured by FePt nanoshells, some photon energy was transferred to heat, the heat from the high-temperature nanoparticles then dissipates to the surrounding medium. The stable and considerable photothermal efficiency for NIR light makes FePt NPs as well as FePt NPs-based nanoparticles very promising in the laser treatment of cancer. Most of NIR-absorbed gold nanostructures changed their shape due to the low melting temperature, which not only has less the absorption cross-section but also significantly shift the surface plasmon resonance absorption peak away from NIR

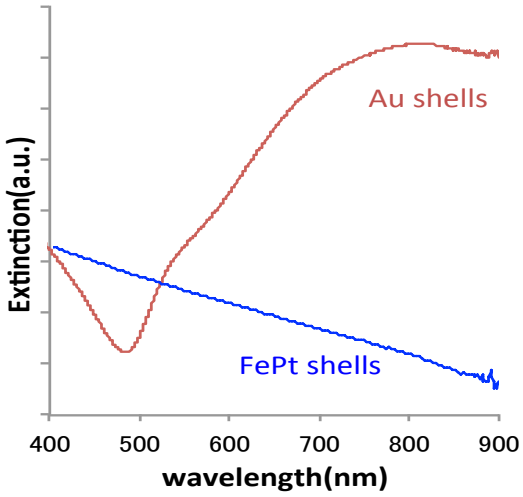

Figure 4.6 Experimental extinction spectra of FePt nanoshells and gold nanoshells.

region. In contrast to, FePt NPs could consistently convert light to heat regardless of the changes of shapes and refractive index of the surrounding media. For gold nanoshells, the higher photothermal efficiency may be attributed to strong plasmonic absorption. While the electrons in gold nanoshells oscillate with the incident electric field of laser light, they transfer electro-magnetic waves to heat more efficiently, i.e. enhanced plasmonic absorption since the optical wavelength of laser light (808 nm) is at the plasmon resonance of Au nanoshells (see Figure 4.6). It should be noticed that plasmonic scattering is also enhanced, which does not contribute to heating, but essentially contributes to the photothermal transduction loss.

Terentyuk et al. reported the photothermal efficiency of the gold nanoshells having the similar conditions with our gold nanoshell. The reported experiment conditions and results were compared with ours in Table 4.4.The calculated generated heat of the reported gold nanoshells is 2.5 $x10^{-8}$ J/particle while 2.8 $x10^{-8}$ J/particle for the gold nanoshell prepared in this study in the case of 1 W laser. The agreement between the reported gold nanoshell and the prepared gold nanoshell in this study is quite good, which permits us comparing the experiment results obtained in the study with other literatures.

Table 4.4 Photothermal experiment results of our gold nanoshells and reported gold nanoshells after the irradiation of CW laser

Samples	Size (nm)	Laser Power (W)	Concentration (particle/mL)	Solution volume (mL)	ΔT (°C)	Averaged heat estimated for 1 W laser power (J/particle)
Prepared Au shells	120/ 20	0.5 (808 nm)	$4.0x10^9$	2.0	12.0	2.5 $x10^{-8}$
Reported Au shells	140/ 20	2 (810nm)	5.0 $x10^9$	2.0	66.0	2.77 $x10^{-8}$

4.3.1.2 Dependence on Concentration

We evaluated the temperature increases of various FePt nanoshells aqueous solution

with different concentrations under laser irradiation shown in Figure 4.7 (left) and hence understand the effects on photothermal effect. Table 4.5 showed the characteristics of silica/FePt particles with different concentrations. The obtained photothermal experiment results evidently showed that the temperature of FePt nanoshell solution

Table 4.5 Characteristics of silica/FePt nanoshells with different concentration

Sample	Nanoshell Concentration (particles/ml)	Total Amount of FePt NPs (μg)	Temperature Increase (°C)
S-01	4.0×10^8	10.6	8.4
S-02	8.0×10^8	21.1	9.6
S-03	1.2×10^9	31.7	9.9
S-04	1.6×10^9	42.3	10.7
S-05	2.0×10^9	52.9	11.2
S-06	4.0×10^9	105.8	12.2
S-07	8.0×10^9	211.6	12.8

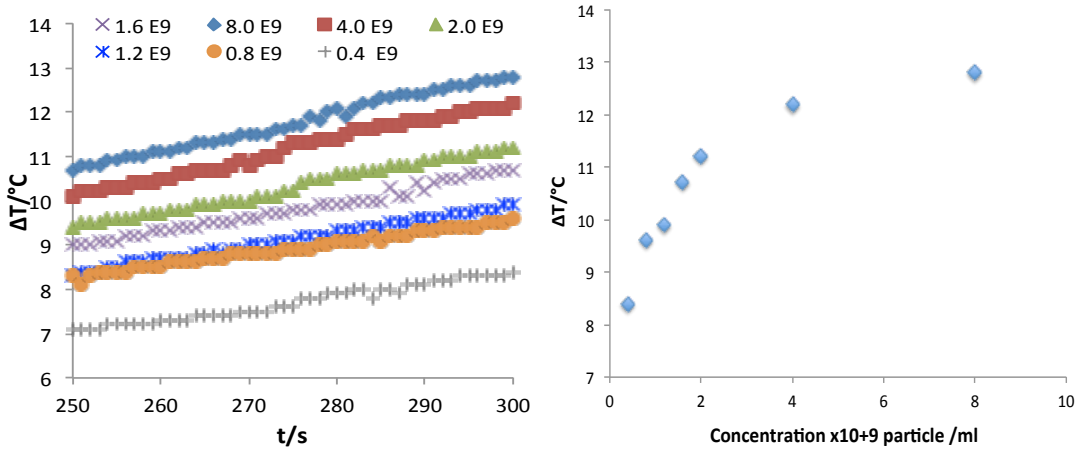

Figure 4.7 (left) Temperature measured over a given time of exposure to NIR light at various nanoshell concentrations at an output power of 0.5 W, and (right) temperature change (ΔT) over a given time as a function of nanoshell concentration.

was positively correlated with the irradiation time and the concentration of solution (particle number). More importantly, the temperature change of the sample solution increased when increasing nanoshell concentration. After the concentration is above 2.0 $x10^9$ particles/mL, no further increase in temperature was observed when the concentration was increased (Figure 4.7 right). It should be noted that the increase of the temperature change is not proportional to the increase of the concentration for FePt nanoshells.

4.3.1.3 Effect of Silica Size

Particle size is another critical factor that strongly affects the therapy efficiency because a lot of the important maters, such as the particle biodistribution and the SPR absorption are related to the particle size. To study the particle size dependence of the photothermal efficiency of nanoshells made from different materials (FePt or gold), two types of various silica/FePt core-shell nanoparticles were prepared using the silica cores of 120nm (120nm-silica/FePt, a1-3) and 320 nm (320nm- silica/FePt, b1-3). To investigate the effect of only core size, I restrict the shell thickness and total surface area of two samples to the same, which means that the number of 320nm-silica/FePt is three times of that of 120nm-silica/FePt. TEM images of the obtained particles are shown in Figure 4.8 (left), and the characteristics and the graph of temperature increase under the laser irradiation of silica/FePt particles prepared with different silica cores are

Table 4.6 Characteristics and temperature increase under the laser irradiation of silica/FePt particles prepared with silica cores different in size

Sample	**Shell thickness (nm)**	**Concentration (particle/ml)**	**FePt/Au wt%**	**ΔT (°C)**	**η %**
120nm-silica/ FePt/Au	18	$6x10^8$	77.0	13.1	38.3
300nm-silica/ FePt/Au	18	$2x10^8$	62.5	11.7	34.2

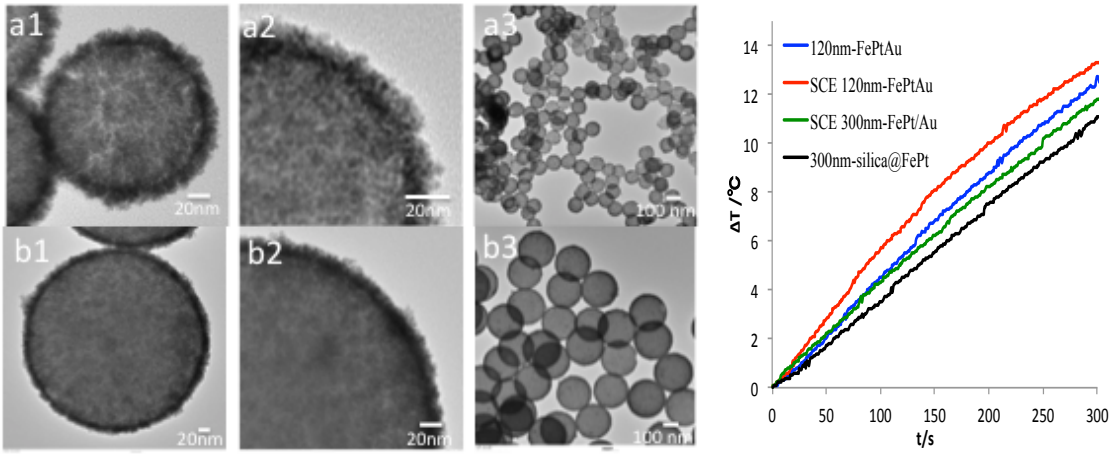

Figure 4.8 (left) TEM images of silica/FePt particles prepared using silica particles of 120nm in diameter (a1-3) and silica/FePt particles prepared using silica particles of 320 nm (b1-3), (right) Graph of the temperature increase when irradiated by CW laser light with an output power of 0.5 W for approximately 5 min.

listed in Table 4.6 .The solution including 320nm-silica/FePt particles with the bigger silica particles showed a relatively higher temperature increase. The bigger-sized FePt nanoshells displayed a favorable behavior as indicated by their higher photothermal efficiency. This result might be caused by the lower concentration of 320nm-silica/FePt particles, which might result in a relatively more active irradiation surface area due to the more far penetrate distance of laser light and the less hindrance effect between each particles to receive laser irradiation.

4.3.1.4 Effect of Thermal Treatment

Figure 4.9 shows TEM images of silica/FePt core-shell nanoparticles prepared using the silica cores of 120nm,followed the thermal treatment via ethanol at 300°C(a1-2), 350℃(b1-2) and 400°C(c1-2) for 1h. As shown in Figure 4.10,photothermal experiment results showed that the temperature increase of treated silica/FePt core-shell nanoparticles was in proportion to the crystalize sizes of FePt NPs. Since heat generation in metal occurs through a free carrier absorption process, the photothermal effect of FePt Nanoshells should depend on the band gap energy. It has been known that the band gap energy of a nanomaterial decrease due to quantum size effect as the crystallite size increases [16]. Thus, it is speculated that increasing the crystalize size of FePt nanoshell can enhance its photothermal effect through more efficient utilization of

lower energy photons due to the narrowed band gap of FePt NPs.

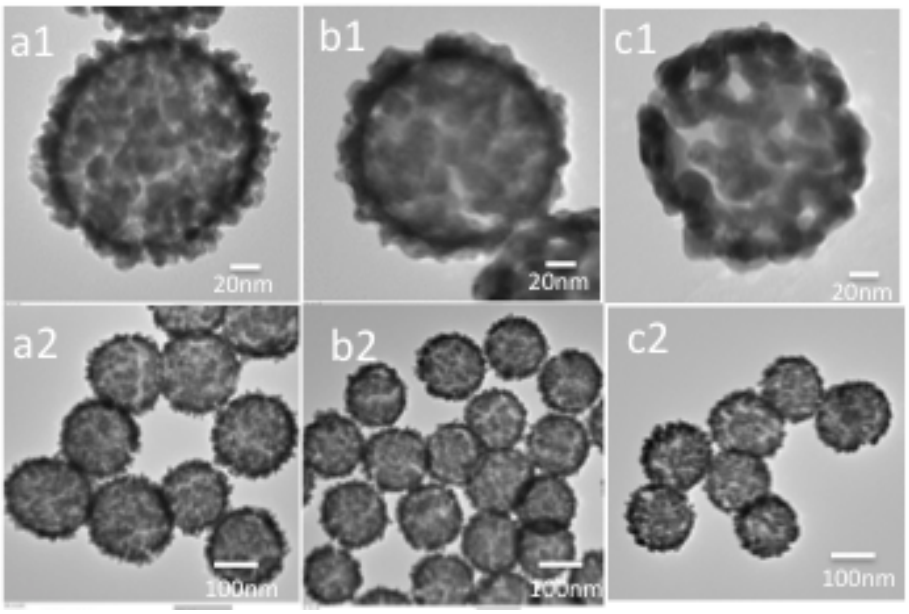

Figure 4.9 silica/FePt core-shell nanoparticles prepared using the silica cores of 120nm,followed the thermal treatment via ethanol at 300°C(a1-2), 350℃(b1-2) and 400°C(c1-2) for 1h.

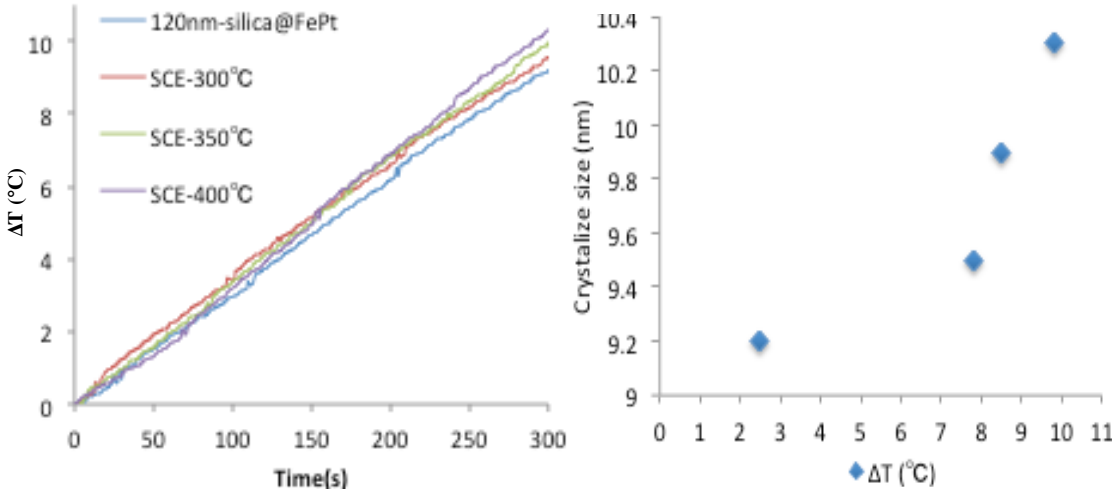

Figure 4.10 (left) Temperature measured over a period of 5 min of exposure to NIR light at various nanoshell concentrations at an output power of 0.5 W. (right) Temperature change (ΔT) over a period of 5 min as a function of crystalize size of FePt NPs.

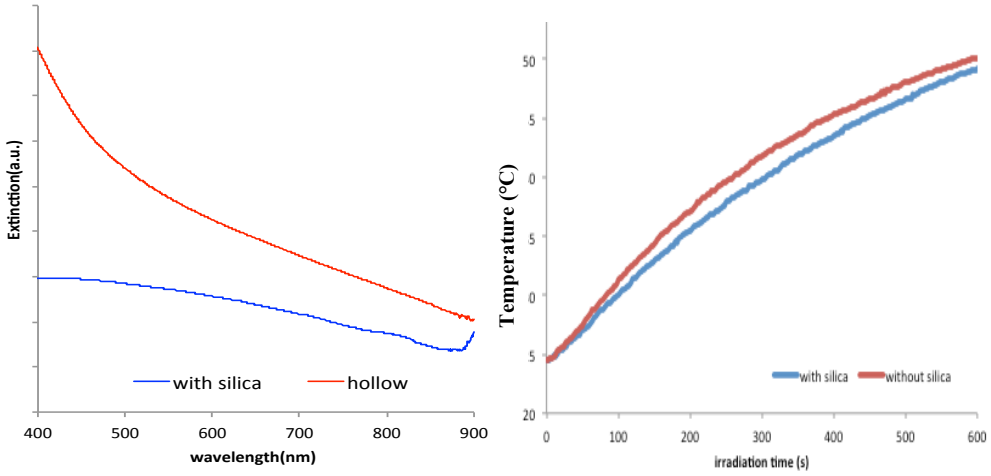

Figure 4.11 UV-vis NIR spectra (left) and temperature increase (ΔT) when irradiated by CW laser light with an output power of 0.5 W for approximately 2 min (right) of silica/FePt core-shell nanoparticles and the hollow particles

4.3.1.5 Effect of Core Material

Figure 4.11 shows UV-vis NIR spectra of 120nm-silica/FePt core-shell nanoparticles and the hollow particles made from 120nm-ilica/FePt core-shell nanoparticles by removing the silica cores and a graph of the temperature increase when irradiated by CW laser light with an output power of 0.5 W for approximately 2 min. There are no obvious changes in the extinction spectra and temperature increase of particles when the core material changed from silica cores to air or water, which is greatly different with plasmonic gold nanoshells.

4.3.2 Heat Generated by Silica-core FePt/Au Nanoshells

4.3.2.1 Dependence on Au Ion Amount

Figure 4.12 shows UV-vis NIR spectra of 120nm-silica/FePt/Au core-shell nanoparticles grown with the different amount of K-gold solution (left) and a graph of the temperature increase when irradiated by CW laser light with an output power of 0.5 W for 5 min (right). The changes of the extinction peak location and the temperature increase with the increase of the amount of Au ion are shown in Figure 4.13. With increasing the amount of Au ion (K-gold solution) from 1ml to 4ml, a red-shift of the extinction peak of the obtained silica/FePt/Au nanoshells was observed in spectra, which result in the increase of temperature. However when the amount of Au ion

increased to 5ml,a decrease in both of extinction spectra and the graph of the temperature increase appeared. TEM images of these silica/FePt/Au particles demonstrated that the increased thickness of complete gold shell was the main reason for this blue shift in spectra as well as the decrease in the photothermal therapy. This result suggests that the silica/FePt/Au core-shell nanoparticles grown with the 4ml of k-gold solution should be optimal to PTT.

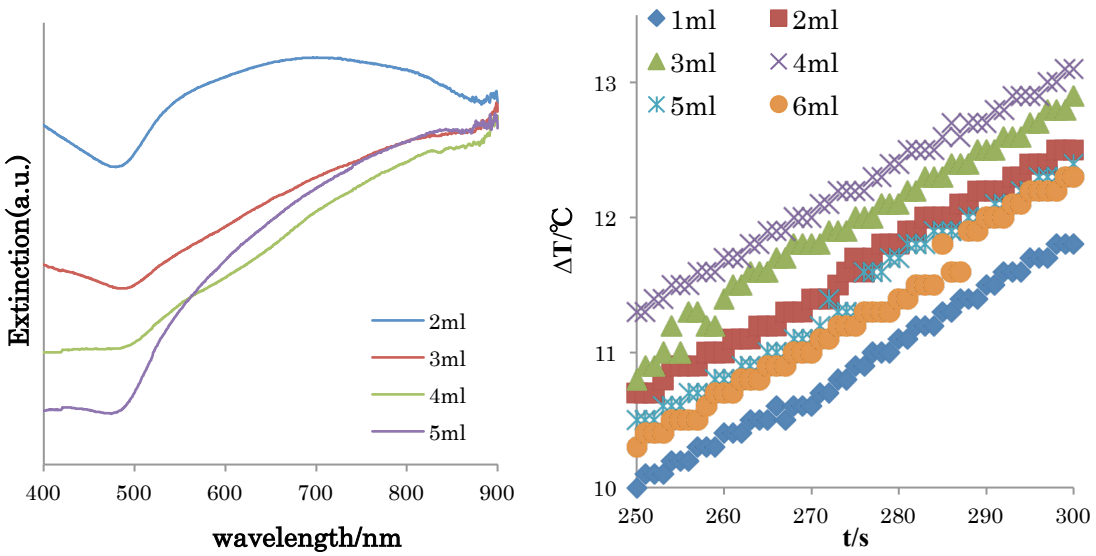

Figure 4.12 UV-vis NIR spectra (left) and temperature increase (ΔT) when irradiated by CW laser light for 5 min (right) of silica/FePt/Au core-shell nanoparticles grown with the different amount of K-gold solution

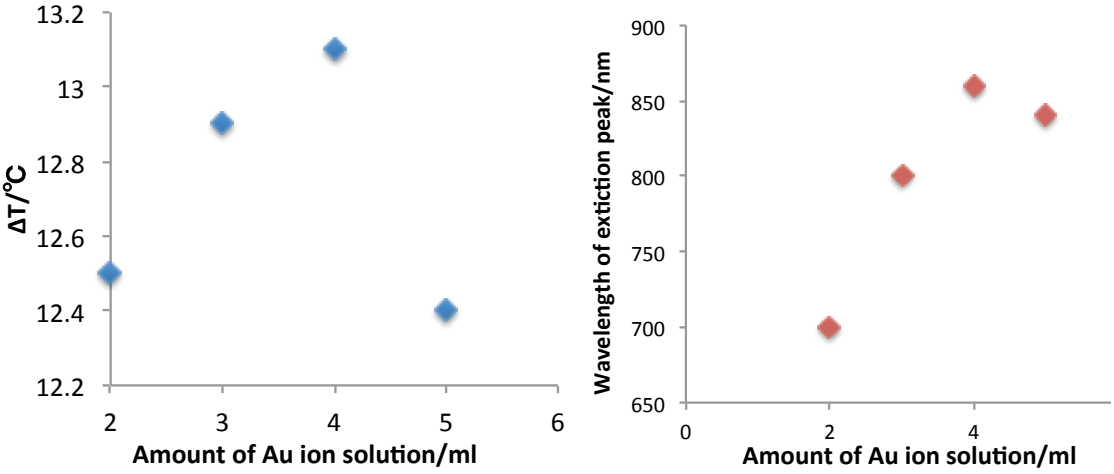

Figure 4.13 Changes of the extinction peak location and the temperature increase with the increase of the amount of Au ion

4.3.2.2 Dependence on Concentration

We evaluated the temperature increase of different concentration of FePt/Au nanoshells aqueous solution under laser irradiation Temperature change (ΔT) over a period of 5 min as a function of nanoshell concentration is shown in Figure 4.14. Table 4.7 showed the characteristics of silica/FePt/Au particles with different concentration.

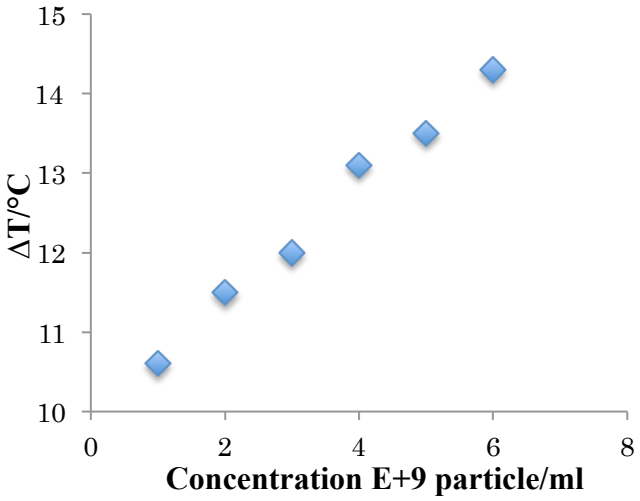

Figure 4.14 Temperature change (ΔT) over a period of 5 min as a function of nanoshell concentration.

Table 4.7 Characteristics of silica/FePt/Au particles with different concentrations

Nanoshell Concentration	Nanoshell Weight (μg)	ΔT (°C)
1.0 x 10^9	18.2	10.6
2.0x 10^9	36.4	11.5
3.0 x 10^9	54.6	12
4.0 x 10^9	72.8	13.1
5.0 x 10^9	91.0	13.5
6.0x 10^9	109.2	14.3

With increasing the nanoshell concentration within 6.0×10^9 particles/ml, the temperature increased but the photothermal effect per 1μg sample particles decreased. The increased ΔT suggests that absorption of light by the nanoshells is a dominant factor within the concentration of 6.0×10^9 particles/ml. The decrease in photothermal effect may be due to the decreased in the irradiated surface area per particle.

4.3.2.3 Effect of Silica Size

In addition to tunable wavelength, the absorption to scattering ratio of gold nanoshells can also be adjusted by changing the outer radium (r_2). For smaller nanoshells, absorption dominates scattering, whereas for larger nanoshells scattering dominates absorption. Herein, we investigate the changes of photothermal property when the particle size is increased by increasing the diameter of silica core from 120 nm to 320 nm. Figure 4.15 (left) shows TEM images of silica/FePt/Au core-shell nanoparticles prepared using the 120nm-silica/FePt particles and 320nm-silica/FePt particles. To investigate the effect of only core size, I restrict the shell thickness and total surface area of two samples to the same, which means that the number of 320nm-silica/FePt/Au used for measurement is three times of that of 120nm-silica/FePt/Au. Table 4.8 lists the characteristics and temperature increase under the laser irradiation of silica/FePt/Au particles prepared with silica cores different in size. When the core size as well as the overall particle size is increased, the excitation of higher order plasmon modes takes place and results in the dipole plasmon resonance shifting to lower energies reflected by a red-shift in resonance wavelength. However the

Table 4.8 Characteristics and temperature increase under the laser irradiation of silica/FePt/Au particles prepared with silica cores different in size

Sample	Shell thickness (nm)	Concentration	FePt/Au wt%	ΔT (°C)	η %
120nm-silica/FePt/Au	18	$4x10^9$	77.0	13.1	38.3
300nm-silica/FePt/Au	18	$1.3x10^9$	62.5	11.7	34.2

extinction peak of 320nm-silica/FePt/Au particles is sharper and the wavelength is longer, the solution including 120nm-silica/FePt/Au particles with the smaller gold shell showed a relatively higher temperature increase. This result suggests that scattering of light by 300nm-silica/FePt/Au particles became a dominant factor due to its large size.

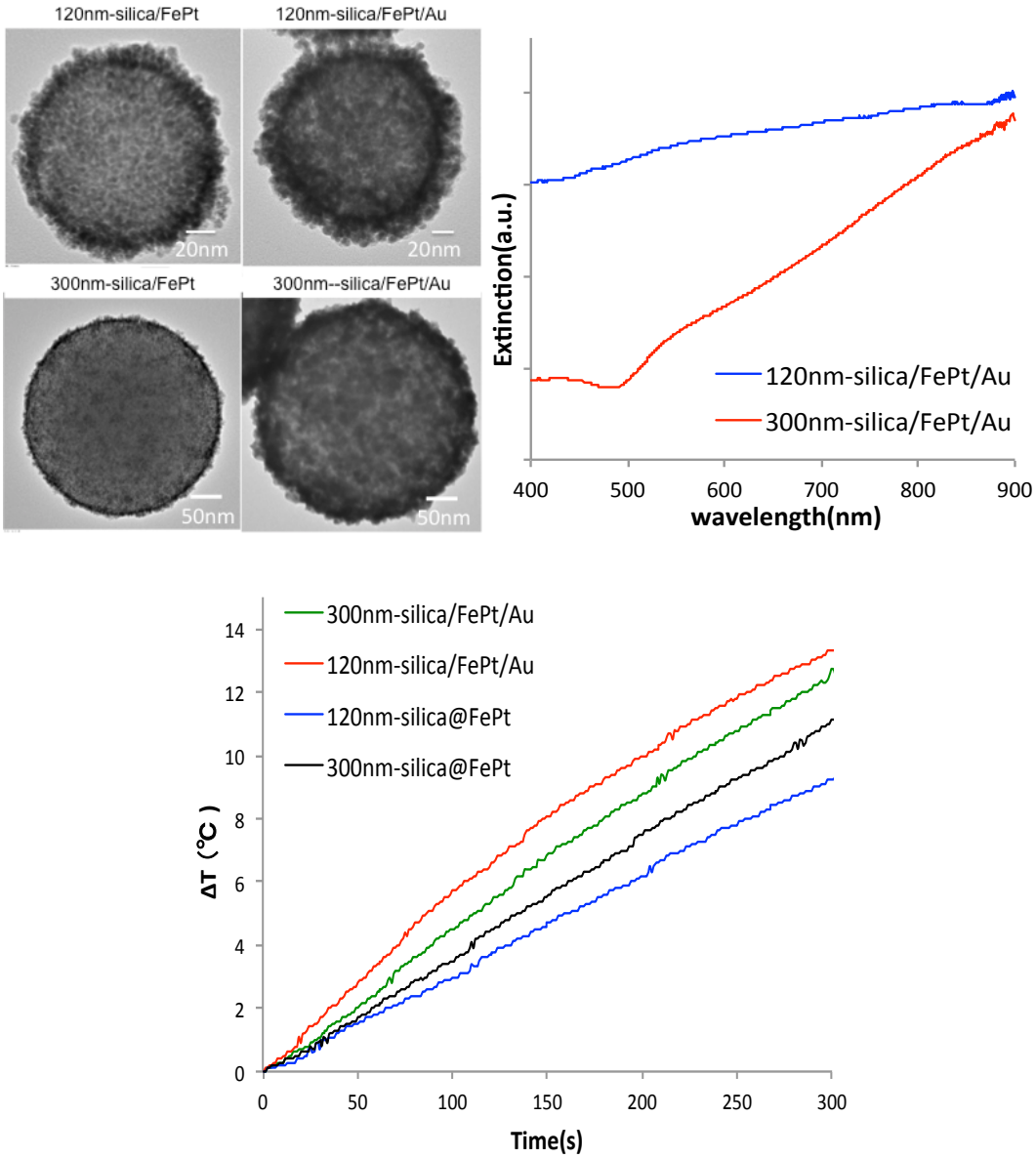

Figure 4.15 TEM images, UV-Vis NIR spectra and temperature increase of silica/FePt/Au particles prepared using 120nm-silica/FePt particles and silica/FePt/Au particles prepared using 300nm-silica/FePt particles.

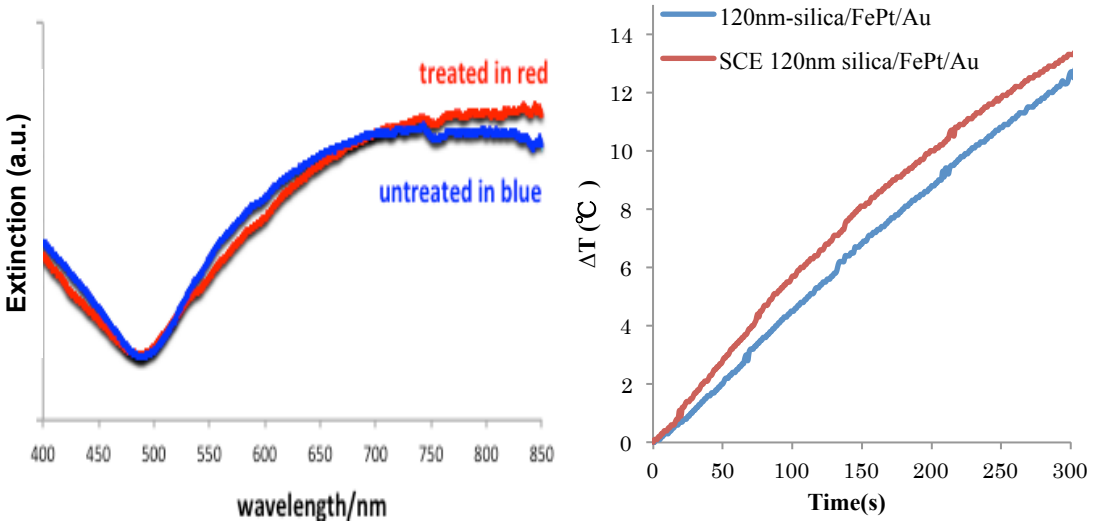

Figure 4.16 UV-Vis NIR spectra (left) and temperature increase (right) of silica/FePt/Au nanoparticles prepared using the silica cores of 120nm,followed the thermal treatment The irradiation is done by CW laser light for 10 min.

Table 4.9 Characteristics and temperature increase under the laser irradiation of silica/FePt/Au particles before and after thermal treatment

Sample	Shell thickness (nm)	Extinction peak (nm)	Concentration (particle/ml)	ΔT (°C) before treatment	ΔT (°C) after treatment
120nm-silica/FePt/Au	18	840	$6x10^8$	13.1	13.3
300nm-silica/FePt/Au	18	750	$2x10^8$	11.7	11.8

4.3.2.4 Effect of Thermal Treatment

Figure 4.16 shows UV-Vis NIR spectra (left) and temperature increase (right) of silica/FePt/Au core-shell nanoparticles prepared using the silica cores of 120nm,followed the thermal treatment via ethanol at 573K for 1h. Experiment results listed in Table 4.9 showed that the temperature increase of treated silica/FePt/Au core-shell nanoparticles was slightly higher than that of untreated silica/FePt/Au core-shell nanoparticles, which well consonants with the changes in extinction spectra. In the extinction spectra, the peak of treated particles showed a slightly red-shift.

4.3.2.5 Effect of Core Material

Figure 4.17 shows UV-vis NIR spectra of 120nm-silica/FePt/Au core-shell NPs and the hollow nanoshell particles made from 120nm-silica/FePt/Au core-shell NPs by removing the silica cores and a graph of the temperature increase when irradiated by

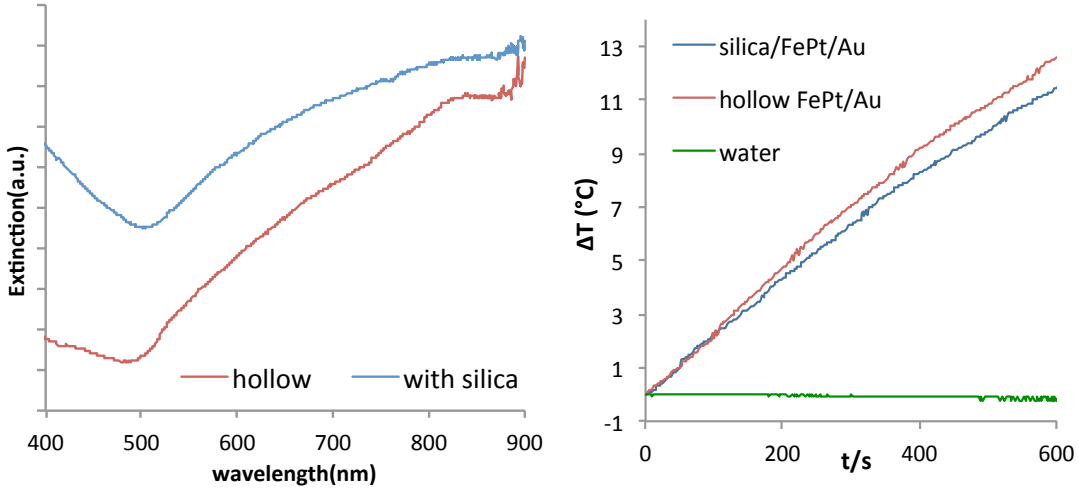

Figure 4.17 UV-vis NIR spectra (left) and temperature increase (ΔT) when irradiated by CW laser light with an output power of 0.5 W for approximately 10 min (right) of 120 nm-silica/FePt/Au core-shell nanoparticles and the hollow nanoshell particles

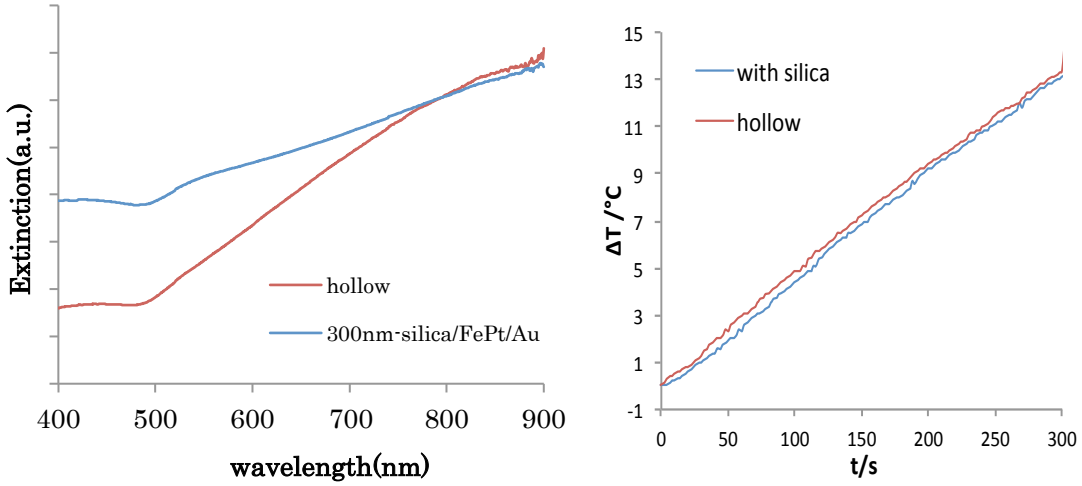

Figure 4.18 UV-vis NIR spectra (left) and temperature increase (ΔT) when irradiated by CW laser light with an output power of 0.5 W for approximately 10 min (right) of 320 nm-silica/FePt/Au core-shell nanoparticles and the hollow nanoshell particles.

CW laser light with an output power of 0.5 W for approximately 10 min. The peak of hollow nanoshell particles showed a slight blue-shift from 860 nm to 830 nm due to the change of core material from silica to air or water, which results in the decreasing core dielectric constant. However the maximum band of extinction peak became sharper,

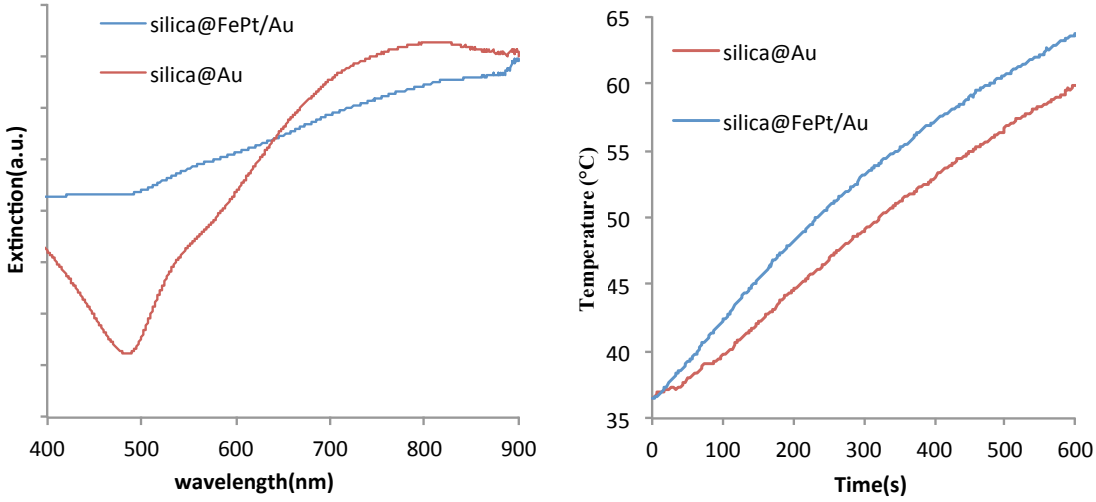

Figure 4.19 Differences of silica-gold nanoshell and silica/FePt/Au nanoshell in UV-vis NIR spectra (left) and temperature increase (ΔT) when irradiated by CW laser light with an output power of 0.5 W for approximately 10 min (right)

Table 4.10 Temperature increases of different kinds of particles when irradiated by CW laser light with an output power of 0.5 W for approximately 10 min

Size	Silica/FePt	Silica/Au	Silica/FePt/Au
120nm	9.2	12.1	13.1
300nm	10.9	11.3	11.7

Table 4.11 Photothermal efficiency for three kinds of nanoshells of 120 nm silica cores.

Sample	Silica/FePt	Silica/Au	Silica/FePt/Au
η %	26.7	35.1	38.0

which suggests an increase of the peak intensity at around 800nm.As a result, the temperature of hollow nanoshell particles after laser irradiation was slightly higher than that of silica-core particles. UV-vis NIR spectra and the graph of the temperature increase of 300nm-silica/FePt/Au core-shell nanoparticles and the hollow particles were shown in Figure 4.18, which show the similar change in extinction spectra and temperature increase.

4.3.2.6 Effect of FePt Shell

Figure 4.19 shows the differences of silica-gold nanoshell and silica/FePt/Au nanoshell in UV-vis NIR spectra o and the graph of the temperature increase when irradiated by CW laser light with an output power of 0.5 W for approximately 10 min. The presence of FePt shell causes the extinction peak of composites broader. The extinction peak of silica/Au particles was sharper and stronger than that of silica/FePt/Au particles in NIR region, which also occurred in the case of iron oxide-based gold nanoshell reported by some groups. The maximum of broadband peak of silica/FePt/Au particles was 860nm, longer than 820 nm of silica /Au particles, which might be caused by the relatively larger particle size of silica/FePt/Au particles. The graph of temperature increase shown in Figure 4.19(right) and Table 4.10 indicates that the photothermal effect of composites was stronger than that of silica/Au nanoparticles. In order to understand the photothermal effect of silica/FePt/Au nanoshells well, the photothermal transduction efficiency for FePt nanoshells, gold nanoshells and FePt/Au nanoshells were calculated and listed in Table 4.11.The higher photothermal efficiency of FePt/Au nanoshells might be caused by the combination of FePt shell with gold shell, which indicates that the two-layered structure brings FePt/Au nanoshells an improvement in photothermal capability, although the presence of FePt shell affect the optical property of composites. It should be noticed that the photothermal effect of composites was not the total of the photothermal effects of mono-layered gold shell and mono-layered FePt shell.

The highly efficient interacting of gold nanoshells with incident electromagnetic energy at surface plasmon frequencies leads to a strong absorption and, in turn, efficient heating, as already discussed before. The basic mechanisms responsible for the photothermal effect of gold nanoshells have been studied a lot [8-13]. When irradiated

by light, the oscillating electromagnetic field of the light induces a collective coherent oscillation of the free electrons of the metal. These excited electrons relax in two different ways: absorption and scattering. The strongly absorbed energy is quickly converted to the metallic lattice in the form of heat, which is subsequently transferred to the surrounding medium resulting in the temperature increase of the surrounding medium. In the case of slower rates, the lattice cools via phonon-phonon coupling, which only results in the temperature increase of the surrounding medium, which can be used in photothermal therapy to induce the death of tumor cells. However, in the case that the rate of energy dissipation is relative faster than that of lattice cooling, the photo-thermal damage for gold nanoshells takes place. The photothermal heating can result in the surface melting of gold nanostructures that induce the reshaping of gold nanostructure, or the melting of whole nanostructure that results in the deformation and destruction of gold nanoshells. Both two melting ways would cause the obvious change in optical absorption characteristics irreversibly [14,15]. Park *et al*. investigated the damage threshold of gold nanoshells (800nm resonance) and found low energies did not produce whole melting; however produce a slow reshaping and eventual degradation of the nanoshell structure, which is explained by large temperature rises near defects in the polycrystalline structure of the gold shell [16]. Figure 4.20 shows TEM images of silica-core Au nanoshell and two types of hollow FePt/Au nanoshells irradiated by laser with an output power of 0.5 W for 1 h. Similar to the study Park *et al*. reported, all of the silica-core gold nanoshells were damaged as observed even with the support of the silica templates in Figure 4.20 (right). This could be explained in terms of the slow heat release of the deposited laser energy into the surrounding solution, which might lead to melting of the gold nanoshells since the gold nanoshells cannot cool as fast as they are heated, they broke and fragment into smaller nanoclusters. To well understand the reason being responsible to the destruction of the irradiated silica-core gold nanoshells, the temperature of the gold nanoshells under the radiation from laser is very important because the temperature of the gold nanoshells decides how the particle melts, however it is very difficult to measure the actual temperature of the particle during the radiation. Assuming the generated heat by the particle only is used to increases the temperature of the particle itself but not surroundings, the maximum temperature the gold nanoshells can reach to during the radiation can be expressed as:

$$Q_{out} = C_p \rho_s V (T_{final} - T_{initial})$$

where heat capacity C_p of Au is 0.129 J/g °C, $\rho_s V$ is mass of all particles(72.8 μg), initial temperature $T_{initial}$ is 19 °C. As discussed before, $Q_{out} = Q_{in} x \eta = I t \eta$ .The photothermal efficiency of gold shells 120/20 nm is 35.1%, and the power of laser I is 0.5 J/s.Then the maximum temperature the gold nanoshells can reach to is given by:

$$T_{final} (°C) = I t \eta / C_p \rho_s V + T_{initial} = 2555.7 * t + 19$$

Since the melting point of gold is 1064 °C, in the case of the gold nanoshell and set up used in this study, the gold nanoshell would be heated to the melting point after only 0.4 second. Based on this calculated result, it can be concluded that the melting of silica-core gold nanoshells induced by heating generated by gold shell itself under laser irradiation may induce the destruction of shell structure.

On the other hand, there were no obvious changes of shape and structure observed in TEM images for hollow FePt/Au nanoshells. Most of hollow FePt/Au nanoshells still

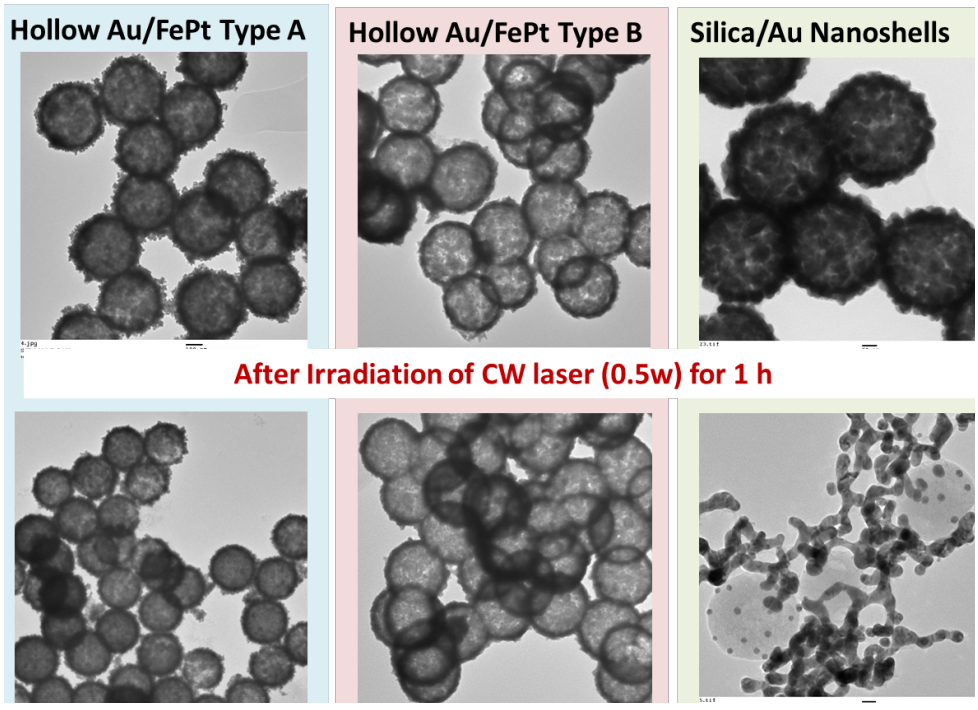

Figure 4.20 TEM images of Au nanoshell and two types of hollow FePt/Au nanoshells irradiated by laser with an output power of 0.5 W for 1 h.

Table 4.12 Thermal conductivity of Au, Fe,Pt and silica

Materials	**Au**	**Fe**	**Pt**	**Silica**
Thermal conductivity	320	84	70	1.3

maintained the hollow structure. This might be explained in terms of the presence of FePt shells since the characteristics of the surrounding medium strongly influence the cooling dynamics of the hot electrons in the nanostructures. In the case of hollow FePt/Au nanoshells, metallic FePt nanoshells having large thermal conductivity is the direct surrounding medium so that the thermal conductivity of the surrounding medium and the thermal contact between the nanostructures and the surrounding medium is increased, which results in the decrease of relaxation time (electron-phonon and phonon-phonon), implying that the cooling dynamics of gold nanoshell coated on the FePt shells would be faster and the melting of gold nanoshell would be delayed. On the other hand, the excellent thermal stability of FePt NPs shown in Table 4.12 would be another reason for the enhanced photothermal stability of FePt/Au nanoshells. The relatively more stable structure of FePt shells as interior layer under high temperature provides the powerful structure support to the outside layer of gold nanoshell and permit the maintenance of shell structure.

4.3.3 Potential of FePt/Au Nanoshells for Photothermal Therapy

To well understand the efficiency and the safety of PTT using hollow FePt/Au NPs nanoshell particles, the needed particle number of hollow FePt/Au nanoshell particles with the diameter of ~170 nm and gold shell of 15 nm if heating 1 cm^3 tumor tissue from 36.5 °C to 42 °C under the irradiation of laser (808 nm, 0.5 W). Assuming there is not any heat loss for the hollow FePt/Au nanoshells-loaded tumor tissue to the surroundings and the heat generated per particle is $Q_{particle}$, the needed particle number is given as:

$$\text{Needed particle number} = m_{tissue} C_{tissue} \Delta T / Q_{particle}$$

When the average density value of human tissue is referred to 1 g/ml, the calculated results are listed in Table 4.13. It has been reported that the safe concentration of silica-core gold nanoshell with the diameter of 1~150 nm and the shell thickness of 20

nm that is very similar with the particles prepared in this study is 3.0 x10^9 for cells of mouse [17], more than two times of the needed concentration of our hollow nanoshell particles. Therefore, it is considered that our hollow nanoshell particles should be still effective even in the case that heat loss through blood vessels cannot be ignored.

Table 4.13 Needed particle number for heating 1cm^3 tumor tissue from 36.5 to 42°C with the laser (808 nm, 0.5 W)

Samples	η %	**Heat (J/s per particle)**	**Needed particle**
Hollow Type A	36.4	1.6x10^{-8}	1.3 x10^9
Hollow Type B	34.4	1.5x10^{-8}	1.2 x10^9

4.4 Conclusions

The photothermal capability of various core-shell nanoparticles as well as their hollow nanoshell particles was demonstrated using CW laser in this chapter. The silica-core FePt/gold nanoshells possessed higher photothermal conversion efficiency higher than silica-core gold shells that have the similar particle size and shell thickness of gold due to the presence of FePt nanoshells that also show an excellent photothermal effect. And hollow FePt/Au nanoshells showed higher photothermal conversion efficiency than silica-core core-shell FePt/Au nanoparticles due to the change of core materials. The heating rate for hollow FePt/Au nanoshells (Type A and Type B) in the experiment was approximately 1 °C/min. And the calculated therapeutic particle number of hollow FePt/Au nanoshells is far lower than the reported safe particle number. It can be concluded that hollow FePt/Au nanoshells can efficiently but safely enough raise the temperature above the hyperthermia level. Moreover, these hollow nanoshells are not only uniform in both size and shape, but also display tunable SPR properties and significantly enhanced photothermal stability as compared with gold nanoshells. Based on these results, we can conclude that hollow FePt/Au nanoshells are potential candidates applicable to photothermal therapy.

Reference

[1] C.F.BohrenandD.R.Huffman,(Wiley,NewYork,1998).

[2] Buining P A, Liz-Marzan L M and Philipse A P 1996 J. Colloid InterfaceSci.179318

[3] D. Wu et al. / Solid State Communications 146 (2008) 7–11

[4] E. Prodan, C. Radloof, N.J. Halas, P. Nordlander, Science 302 (2003) 419.

[5] Giering, K.; Lamprecht, I.; Minet, O.; Handke, A. Thermochim. Acta 1995, 251, 199–205.

[6] C.L. Chen et al. / Biomaterials 34 (2013) 1128e1134;

[7] I.sagnes,A Halimaoui,G. Vinecent and P.A.Badoz, Appl.Phys.Lett., 62,1155-1157 (1993)

[8]Link, S.; Burda, C.; Mohamed, M. B.; Nikoobakht, B.; El-Sayed,

[9] M. A. J. Phys. Chem. A 1999, 103, 1165.

[10] Kurita, H.; Takami, A.; Koda, S. Appl. Phys. Lett. 1998, 72, 789.

[11] Inasawa, S.; Sugiyama, M.; Yamaguchi, Y. J. Phys. Chem. B 2005, 109, 3104.

[12] Plech, A.; Kotaidis, V.; Lorenc, M.; Boneberg, J. Nat. Phys. 2006, 2, 44.

[13] Kamat, P. V.; Flumiani, M.; Hartland, G. V. J. Phys. Chem. B 1998, 102, 3123.

[14] Kamat, P.V., Flumiani, M. and Hartland, G.V. (1998). J.P.Chemistry B, 102, 3123–8.

[15] Aguirre, C.M., Moran, C.E., Young, J.F. and Halas, N.J. (2004). J.P.Chemistry B, 108, 7040–5.

[16] Park, J., Estrada, A., Sharp, K., Sang, K., Schwartz, J.A., Smith, D.K., Coleman, C., Payne, J.D., Korgel, B.A., Dunn, A.K. and Tunnell, J.W. (2008) Optics Express, 16, 1590–9.

[17] Pannerec-Varna, M., Ratajczak, P., Bousquet, G. et al. Gold Bull (2013) 46: 257. doi:10.1007/s13404-013-0115-8

Chapter 5 General Conclusions

In this thesis, synthesis and characteristics of two kinds of hollow magnetic gold nanoshells were investigated and discussed from the viewpoint of photothermal therapy (PTT). One was named as Type A composed of double-layered FePt/Au shell in which there are a lot of small pores of ~5nm and a hollow space inside. The other was named as Type B with a netlike nanoshell of FePt/Au made from silica/FePt/Au core-shell nanoparticles via thermal treatment in a supercritical fluid, followed by the removal of silica template particles. The morphology including the thickness, roughness, surface coverage of the shell, the pore size and so on, the optical properties and the magnetic properties can be tuned by controlling the conditions of synthesis and thermal treatment. The formation mechanism of two types of porous nanoshells was discussed. The main achievements and findings in the present study are summarized in the followings.

1. NIR light-absorbing gold nanoshells were successfully fabricated on polymer-modified silica/FePt core-shell nanoparticles via the two-step seed-mediated growth method using PEI polymer layer as an interlayer. The cationic polyelectrolyte PEI with high amine content binds to the negatively charged FePt nanoshell through electrostatic self-assembly to form a stabilizing polyelectrolyte layer, which is necessary to not only the deposition of Au nanoparticles but also the growth of the uniform gold shell. I have studied the effects of various fabrication conditions of PEI polymer on the quality of gold shells and found that using the mixture of PEI polymers with different molecular weight to modify the FePt nanoshell made successful the formation of a high-quality gold shell with a smooth and thin morphology being responsible to the appearance of a strong absorption. Additionally, the total particle size can be controlled by change the size of silica cores or tuning the shell thickness.

2. Two types of porous nanospheres with different morphology and properties (Type A and Type B) were synthesized. Type A was a hollow double-layered particle consisting of a FePt interior shell and an Au outer shell made from silica/FePt/Au core-shell particles by removal of silica cores via using NaOH etching. There are many small pores ($d < 5$ nm) evenly distributed on the surface of the FePt/Au nanoshells. I found that the presence of the interior layer of FePt increased the mechanical strength of the hollow particles. Even without the support of silica template, the shell structure of hollow particle was still maintained and there were no changes in both the morphology and the total size. The extinction peak of hollow nanoshell particles showed a blue-shift

because of a decrease in the refractive index of the core, which results from the change of the core from silica to water or air.

3. Type B was a hollow double-layered shell spheres composed of a FePt interior shell and a Au outer shell made by thermal treatment of the silica/FePt/Au core-shell particles, followed by NaOH etching. Neighboring metal nanoparticles were fused together during the thermal treatment, resulting in the formation of a netlike shell, a lot of enlarged pores (~20 nm) and a smooth and thin surface. The effects of various treatment conditions and the thickness of metal shell have been studied. The results showed that increasing the treatment temperature or time made the surface of hollow particles smoother and more complete, and increasing the thickness of FePt shell or Au shell enhanced the structural stability of the hollow nanoshell particles but also reduced the pore number and pore size. The changes of morphology brought a red-shift of the peak in the extinction spectra and the increase in crystallite size of FePt NPs resulting in the improvement of magnetic properties. It should be noticed that it is the enhanced thermal stability of the core-shell particles resulting from the presence of FePt shell, making the thermal treatment an effective method for the core-shell particles to enlarge the pore size.

4. The excellent photothermal capability of magnetic gold nanoshells as well as their hollow nanoshell particles was demonstrated using a CW laser. The dependences of the photothermal effect on the core size and the particle concentration were similar but that on the core material and the shell thickness were different between for the FePt nanoshells and for the gold nanoshells. The obtained heating rate for the suspension of the nanoshells (Type A and Type B) in the experiment was approximately 1 °C/min, which is slow enough to heat tissue in a controllable manner, but efficient enough to raise the temperature above the hyperthermia level. The calculated therapeutic particle number of hollow FePt/Au nanoshell particles is far less than the reported dose of Au NPs under the safety level for human body. These experimental analytical results suggest that magnetic gold nanoshells have a potential of a highly efficient PTT agent.

Acknowledgement

I am grateful to my supervisors, Professor Yoshitaka Kitamoto for his guidance and support for whole of my doctoral course.

I am deeply grateful to my co-supervisor Associate Professor Hiroyuki Wada for his warm encouragement and providing support to carry on this study.

I am also indebted to Associate Professor Kazutaka Nakamura for his valuable advice and providing support to carry on this study.

I am grateful to Professor Kotaro Kajikawa for his guidance and support for this study.

I am grateful to Associate Professor Takeharu Tsuge as my life advisor for his kindness.

I would like to express my gratitude to all members of Kitamoto lab for their kind help during my doctoral course in Tokyo Institute of Technology. I will remember their active cooperation, courteous concerns and warmest support forever.

I wish to acknowledge especially my family in the all aspects of my student life.

RUZHI ZHANG

2016/12/31

Accomplishment

Journal Publications

1. R. Zhang, T. Hamada, S. Inagi, and Y. Kitamoto, Magnetic Beads Composed of Au/FePt Hybrid Nanoshell and Silica Core. Journal of the Magnetics Society of Japan, Vol.37, No.3-2, 2013.

2. Ryushi Fujimura, Ruzhi Zhang, Yoshitaka Kitamoto, Masayuki Shimojo, Kotaro Kajikawa. Modeling of semi-shell nanostructures formed by metal deposition on dielectric nanospheres and numerical evaluation of plasmonic properties, Japanese Journal of Applied Physics, Vol. 53, Feb. 2014.

Presentation at International meetings

1. R. Zhang, T. Hamada, S. Inagi, and Y. Kitamoto, Magnetic hollow capsules composed of Au/FePt hybrid nanoshell, The 11th International Conference On Ferrites, Japan, Apr.2013

2. R. Zhang, Y. Kitamoto, Magnetic hollow capsules composed of Au/FePt hybrid nanoshell, International Conference on BioSensors, BioElectronics, BioMedical Devices,BioMEMS/NEMS and Applications,Oct.2013

Awards

1. Yamazaki Yohtaro Memorial Student Award, The 11th International Conference On Ferrites, 2013